

Electrospinning of Poly(ϵ -Caprolactone)

by

Chen-Ming Hsu

A Thesis

Submitted to the Faculty

of the

WORCESTER POLYTECHNIC INSTITUTE

In partial fulfillment of the requirements for the Degree of Master of Science

in

Materials Science and Engineering

By

May 2003

APPROVED:

Satya Y. Shivkumar, Associate Professor of Mechanical Engineering and
Advisor

Richard D. Sisson, Jr., Professor of Mechanical Engineering
Materials Science and Engineering Program Head

ABSTRACT

The objectives of the present work are to produce porous polymeric scaffolds with Poly (ϵ -Caprolactone), PCL, by electrospinning. The structure in the electrospun polymer has been characterized by scanning electron microscopy. The effects of process variables such as voltage, solution concentration and deposition distance on the structure have been studied. The physical phenomena associated with the electrospinning process have been highlighted through high speed digital photography. The feasibility of using additives to the solution to control the structure of the porous construct has been examined. The data indicate that a range of structural morphologies can be produced in the electrospun polymer. Solid and hollow sub-micron beads can be produced by electrospraying of dilute solutions. Beyond a critical solution concentration of about 4 wt% PCL, elongational flow stabilizes the fibrous structure and a web of interconnected sub-micron fibers may be obtained. The average fiber diameter increases with concentration. A combination of elongated beads and fibers, known as the bead-on-string morphology is also observed under many conditions. The fibrous structure is stabilized at high voltages. The fiber diameter in the electrospun polymer typically exhibits a bimodal distribution. The addition of DMF (N,N-dimethylformamide) to the solution increases the deposition rate significantly and leads to extensive splaying, thereby reducing the fiber diameter to about 150 nm. DSC data indicate that electrospinning may lower the degree of crystallinity in the polymer. The wide of range of structural characteristics that may be obtained in the electrospun polymer make it suitable for many biomedical applications including medical textiles, drug delivery, membrane separation, tissue engineering and organ regeneration.

ACKNOWLEDGEMENTS

I would like to express my sincerest thanks to the Materials Science and Engineering Faculty for the support. I would also like to thank K. Zeisler-Mashl, Qingyue Pan, Sumanth Shanker, Mohammed Maniruzzaman for all their help throughout this project. I also appreciate all of the help I have received from Prof. R.R. Biederman throughout two years here at WPI. Through his help and professional criticism I believe I have found out what a true artistic photograph looks like and how a professional skill is learned. I also thank Professor Satya Shivkumar for all of his constant assistance. Finally, I would like to thank my parents for their constant support and understanding, their support was immeasurable.

TABLE OF CONTENTS

ABSTRACT	ii
ACKNOWLEDGEMENTS	iii
TABLE OF CONTENTS	iv
LIST OF FIGURES	v
LIST OF TABLES	xi
1. INTRODUCTION	1
2. LITERATURE REVIEW	4
2.1 Scaffold Materials	4
2.2 Scaffold Fabrication	9
2.2.1 <i>Fiber bonding</i>	9
2.2.2 <i>Solvent casting and particulate leaching</i>	10
2.2.3 <i>Membrane lamination</i>	11
2.2.4 <i>Extrusion</i>	11
2.2.5 <i>Gas foaming</i>	12
2.2.6 <i>Phase separation</i>	13
2.3 Electrospinning	14
2.4 Shapes of Fibers Produced by Electrospinning	25
2.5 Structure in Electrospun Polymer	26
2.6 Effects of Process Variables	28
2.7 Applications of Electrospinning	33
3. OBJECTIVES	37
4. MATERIALS AND METHODOLOGY	38
5. RESULTS AND DISCUSSION	42
5.1 Structure in Electrospun PCL	42
5.2 Deposition Area	52
5.3 In situ Observations	53
5.4 Effect of Solution Concentration	57
5.5 Effect of Voltage	70
5.6 Effect of Deposition Distance	78
5.7 Effect of DMF	81
5.8 Effects of Electrospinning on Microstructure of PCL	87
6. CONCLUSIONS	92
7. REFERENCES	95
APPENDICES	97

LIST OF FIGURES

- Fig. 1 Schematic showing the evolution of various therapeutic methods based on tissue engineering [1].
- Fig. 2 *mer* structures of PLA, PGA and their copolymers.
- Fig. 3 *mer* structure of Poly (ϵ -caprolactone), PCL.
- Fig. 4 Typical structure in a PGA-bonded fiber mesh, prepared by a fiber bonding technique, embedded in PLLA, heated at a temperature of 195°C for 90 min and 235°C for 5 min [5].
- Fig.5 Photograph of a 75:25 PLGA scaffold with porosity, using sodium chloride of size range 300-500 μm as a porogen [5].
- Fig.6 Photograph of a membrane-laminated PLLA scaffold with a noselike shape [5].
- Fig.7 Photograph of a porous tubular PLLA scaffold processed by an extrusion technique for peripheral nerve regeneration [5].
- Fig. 8 Schematic of the electrospinning and electrospaying process [9].
- Fig. 9 Schematic of the electrospinning process for producing porous 3-D structures [10].
- Fig. 10 Surface area in the porous structure as a function of fiber diameter for various processing techniques [11].
- Fig. 11 Schematic illustration of the effects by electric field applied to a solution in a capillary.
- Fig. 12 Schematic illustrating the various modes of charged jet that emanates from the Taylor cone. The essential characteristics of each mode are summarized in Table V [33].
- Fig. 13 Various instabilities that may be induced in the viscoelastic jet that is ejected from the Taylor's cone.
- Fig.14. Scanning electron micrograph of coiled or looped nanofibers on the surface of the collector [21].
- Fig. 15 Schematic illustration of the various physical phenomena occurring during electrospinning a viscoelastic polymer.
- Fig. 16 Example of Splaying in the jet that emerges from the Taylor Cone [21].
- Fig. 17 Example of bead formation during electrospinning. The resulting structure is often referred to as "Bead-on-string" morphology [20].
- Fig.18 Photograph showing electrospun PEO fibers with generally circular cross section [32].

- Fig. 19 Photograph of flat fibers (a) and torroids (b) produced by electrospinning, the torroids may form by the collapse of beaded fibers [22].
- Fig. 20 Photographs showing branched (a) and split (b) fibers formed during electrospinning [22].
- Fig. 21 Bright field TEM photograph showing a fibrillar structure in electrospun products. bright field TEM of electrospun SLPF filaments reveals a fibrillar texture. Crystallites can be seen at the thinnest parts of the filaments [13]
- Fig. 22 Schematic of the shishkebab structure of the crystalline region in electrospun silk filaments [13].
- Fig. 23 Effect of applied field strength on the average fiber diameter [13].
- Fig. 24 Viscosity and surface tension of the polymer solution as a function of concentration [9].
- Fig. 25 Effect of solution concentration on the structure of electrospun D,L-PLA fibers A. 20 wt% B. 25 wt% C. 30 wt% D. 35 wt%. [14].
- Fig. 26 Effect of solution viscosity on the structure in the electrospun product (a) 13 mPa.s (b) 74 mPa.s (c) 289 mPa.s (d) 527 mPa.s [20] .
- Fig. 27 Effect of deposition distance on structure of electrospun polymer a) 2.0 cm (round fibers) b) 0.5 cm (flat fibers) [13].
- Fig. 28 Schematic illustration of the effects of process parameters on the the structure of the electrospun product [13].
- Fig. 29 Photographs showing the range of structures that can be produced with various biopolymers by electrospinning.
- Fig. 30 Release profile for Mefoxin from electrospun PDLA membranes [14].
- Fig. 31 Schematic of the electrospinning apparatus.
- Fig. 32 Photograph of the electrospinning apparatus.
- Fig. 33 Photographs showing the structure in electrospun PCL for two extreme conditions corresponding to electropraying (a) and electrospinning (b). (a) concentration = 3wt%, V = 30 kV (b) concentration = 5 wt%, V = 40 kV.
- Fig. 34 Calculated variation of solution viscosity with concentration for the chloform-PCL system.
- Fig. 35 Photographs showing general fiber crosssections in the electrospun PCL (a) round fibers (b) flat fibers.
- Fig. 36 Photographs showing the structure in the electrospun polymer (a) fibers mixed with round beads (b) fibers mixed with spindle-like beads.
- Fig. 37 Photographs showing the structure in electrospun PCL showing “bead-on-string” morphology with a combination of round and spindle-like beads (a) and (b) flat and round fibers and spindle-like beads.

- Fig. 38 Photographs showing stabilized filaments between droplets (a) spherical and (b) spindle-like.
- Fig. 39 Photographs showing fibers with large and small diameters. Many points of fiber contact may be observed in the structure. (a) Fiber merging, side by side growth, branching and flattening are observed at several locations. (b) Significant fiber flattening and fiber merging (inset).
- Fig. 40 Photographs showing various levels of splaying from beads.
- Fig. 41 Photographs showing fiber splitting (a) and splaying (b).
- Fig. 42 A low magnification photograph of fibers showing bending, coiling and looping of fibers due to bending instability.
- Fig. 43 Photograph showing surface undulations of characteristic wavelength resulting from bending instability.
- Fig. 44 Schematic illustration of the deposition area. The distance of elongational flow (λ) and the deposition area (A) depend strongly on experimental conditions. In most experiments, the structure was examined at the centre of the deposition area (X).
- Fig. 45 Photographs showing the structure at (a) the center (X) and (b) the periphery (Y) of the deposition area. (Concentration = 5 wt%, Voltage = 40 kV)
- Fig. 46 Photograph showing the dripping of the solution in the absence of an electrical field (solution concentration = 3wt%).
- Fig. 47 Photograph showing the ejection of a stable jet from the tip of the needle at a critical voltage.
- Fig. 48 Photograph showing the breakdown of the jet.
- Fig. 49 Photograph showing the breakdown of the primary jet.
- Fig. 50 Photograph showing elongational flow at the tip of the needle and splaying of the jet.
- Fig. 51 Mass of PCL deposited on the collector in 2 min as a function of solution concentration (Voltage = 30 kV, Needle size =20 gauge)
- Fig. 52 Photographs showing the structure of electrospun PCL for various solution concentrations.
- Fig. 53 Bead size distribution in the polymer obtained on the collector for solution concentration of (a) 1% (30 kV, 26 gage needle) (b) 3% (30kV, 20 gage needle).
- Fig. 54 Photograph showing cavities on the surface of the beads. Hollow beads can be produced by electrospinning.
- Fig. 55 Fiber diameter distribution in the polymer obtained on the collector for a solution concentration of (a) 5 wt% PCL (b) 7 wt% PCL (c) 9 wt% PCL

- (30 kV, 20 gauge needle).
- Fig. 56 Sequential images showing the breakdown and splaying of the jet during electrospaying. (3wt% PCL, 30 kV)
- Fig. 57 Sequential images showing the breakdown and splaying of the jet during electrospinning. (9 wt% PCL, 30 kV)
- Fig. 58 Schematic illustration of the breakdown of the jet at 3 wt% PCL (a) and 9 wt% PCL (b). These conditions correspond to the breakdown of the jet in electrospaying (a) and electrospinning (b).
- Fig. 59 Mass of PCL deposited on the collector in a time of 2 min for various voltages (Solution concentration = 5 wt%).
- Fig. 60 Photographs showing the effect of applied voltage on the structure in the electrospun polymer (solution concentration 5 wt%, deposition distance =75 mm). (a) 20 kV (b) 25 kV (c) 30 kV (d) 40 kV
- Fig. 61 Fiber diameter distribution in the polymer obtained on the collector for a voltage of (a) 25 kV (b) 30 kV (c) 40 kV (concentration = 5 wt% PCL).
- Fig. 62 Sequential images showing the breakdown and splaying of the jet during electrospinning. (5wt% PCL, 20 kV).
- Fig. 63 Sequential images showing the breakdown and splaying of the jet during electrospinning. (5wt% PCL,40 kV)
- Fig. 64 Schematic illustration of the breakdown of the jet at an applied voltage of 25 kV and (b) 40 kV. Regions of primary splaying (I) and secondary splaying (II) are indicated.
- Fig. 65 Photographs showing the structure in the electrospun polymer obtained from a 9 wt% PCL solution. (a) 10 kV, Position X, Center (b) 30 kV, Position X, Center (c) 10 kV, Position Y, Periphery (d) 30 kV, Position Y, Periphery. The positions correspond to the sample locations shown in Fig. 44.
- Fig. 66 Photographs showing the structure in the electrospun polymer for various deposition distances (a) 7.5 cm (b) 12.5 cm (c) 15 cm (d) 17.5 cm (Solution concentration 9 wt%, V = 30 kV).
- Fig. 67 Fiber diameter distribution in electrospun PCL for various deposition distances (a) 7.5cm (b) 12.5 cm,(c) 15 cm (9 wt% PCL , V= 30 kV)
- Fig. 68 Effects of chloform/DMF ratio(v/v) on structure of electrospun PCL. a) Pure chloroform at 7.5cm (b) 12: 1 at 10cm (c) 9: 1 at 10cm (d) 6:1 at 7.5cm deposition distance (5 wt%, 40 kV, 20 gage needle).
- Fig. 69 Fiber diameter distribution for various chloroform/DMF ratios (v/v) (a) Pure chloroform (b) 12:1 (c) 9:1
- Fig. 70 Photographs showing (a) extensive splaying from a single bead and (b)

fibers connecting different beads in samples with chloroform/DMF ratio of 9:1. (40 kV, 5 wt%, 20 gage needle, deposition distance = 10 cm)

- Fig. 71 Photographs showing fiber morphology for various chloroform/DMF ratios (v/v) (a) Pure chloroform (b) 12:1 (c) 9:1
- Fig. 72 Sequential images showing the breakdown and splaying of the jet with DMF (5wt% PCL, 40 kV, Chloroform/DMF ratio =12:1 v/v).
- Fig. 73 Schematic illustration of the differences between the breakdown and splaying of the jet without (a) and with DMF (b).
- Fig. 74 Typical DSC curve for as received PCL (heating rate = 10°C/min).
- Fig. 75 DSC curves for electrospun PCL produced at (a) 20kV (b) 40kV (Solution concentration = 5 wt% PCL, deposition distance = 7.5 cm).
- Fig. 76 DSC curves for electrospun PCL produced at (a) 3 wt% (b) 5 wt% (c) 9 wt% (30 kV, deposition distance = 7.5 cm).

Appendices

Appendix B Additional Photographs of electrospun PCL under various conditions.

- Fig. B1 Photographs of particles produced at 1 wt % PCL (30kV).
- Fig. B2 Photographs of particles produced at 3 wt % PCL (30kV).
- Fig. B3 Photographs of fibers produced at 5 wt % PCL (30kV).
- Fig. B4 Photographs of fibers produced at 7 wt % PCL (30kV).
- Fig. B5 Photographs of fibers produced at 9 wt % PCL (30kV).

Appendix C Additional Photographs of electrospun PCL under various voltages.

- Fig. C1 Photographs of fibers produced at 5 wt % PCL (40kV).
- Fig. C2 Photographs of fibers produced at 5 wt % PCL (25kV).
- Fig. C3 Photographs of fibers produced at 5 wt % PCL (20kV).
- Fig. C4 Photographs of fibers produced at 9 wt % PCL (10kV).

Appendix D Additional Photographs of electrospun PCL under various distances.

- Fig. D1 Photographs of fibers produced at 9 wt % PCL (distance = 12.5 cm).
- Fig. D2 Photographs of fibers produced at 9 wt % PCL (distance = 15 cm).

Appendix E Additional Photographs of electrospun PCL with DMF.

Fig. E1 Photographs showing the morphology of electrospun PCL with DMF addition (5 wt% PCL, $\text{CHCl}_3/\text{DMF}=12/1$ volume ratio, 40 kV, distance = 10cm)

Fig. E2 Photographs showing the morphology of electrospun PCL with DMF addition (5 wt% PCL, $\text{CHCl}_3/\text{DMF}=9/1$ volume ratio, 40 kV, distance = 10cm)

LIST OF TABLES

Table I	List of biopolymers used in tissue engineering and drug delivery applications [3].
Table II	Various morphological forms PGA and PLA.
Table III	Typical Properties of common biodegradable polymers [8].
Table IV	The advantages and disadvantages of processes for scaffold fabrication [2].
Table V	Summary of the jet characteristics for the different modes shown in Fig. 12 [33].
Table VI	Various process parameters associated with electrospinning.
Table VII	Summary of experimental conditions used during electrospinning of PCL.
Table VIII	Experimentally measured values of the critical voltage at which a jet shoots out from the tip of the needle. Data have been shown for various solution concentrations. At each concentration, at least 10 and up to 15 measurements were conducted. The measured critical voltages have been used to calculate the surface tension of the solution based on the Taylor's equation (eqn (5)).
Table IX	Heats of fusion obtained from the measured peaks in the DSC curves for various conditions. The %crystallinity calculated from the heats of fusion is also shown.

Appendices

Appendix A

Table A	Properties of Poly (ϵ -Caprolactone) used in this study.
---------	--

Appendix B Additional Photographs of electrospun PCL under various conditions.

Table B1	Summary of observations for the photographs shown in Fig. B1
Table B2	Summary of observations for the photographs shown in Fig. B2
Table B3	Summary of observations for the photographs shown in Fig. B3

Table B4 Summary of observations for the photographs shown in Fig. B4

Table B5 Summary of observations for the photographs shown in Fig. B5

Appendix C Additional Photographs of electrospun PCL under various voltages.

Table C1 Summary of observations for the photographs shown in Fig. C1

Table C2 Summary of observations for the photographs shown in Fig. C2

Table C3 Summary of observations for the photographs shown in Fig. C3

Table C4 Summary of observations for the photographs shown in Fig. C4

Appendix D Additional Photographs of electrospun PCL under various distances.

Table D1 Summary of observations for the photographs shown in Fig. D1

Table D2 Summary of observations for the photographs shown in Fig. D2

Appendix E Additional Photographs of *electrospun* PCL with DMF.

Table E1 Summary of observations for the photographs shown in Fig. E1

Table E2 Summary of observations for the photographs shown in Fig. E2

1. INTRODUCTION

Porous polymer structures are used extensively in many applications including medical textiles, wound dressings, drug delivery devices and tissue engineering scaffolds. The microstructure in these materials ranges from isolated open-pore structures to fibrous matrices. Biodegradable polymers such as poly lactic acid (PLA), poly glycolic acid (PGA), poly (ϵ -caprolactone), PCL, and their copolymers and non-biodegradable polymers such as nylon, Teflon and Dacron have been used as the base material. Biodegradable three-dimensional porous polymer scaffolds are used extensively in tissue engineering and guided tissue regeneration. In these applications, scaffolds with high porosity and interconnectivity are required to minimize the amount of implanted polymer and to increase the specific surface area for cell attachment. The scaffold may also be required to contain and release bioactive agents at a controlled rate over extended periods to influence local cellular activity. Optimal attachment and growth of cells are strongly influenced by the pore architecture in the scaffold. Various techniques including phase separation, freeze drying and particle leaching have been used to produce the scaffolds. The typical thickness of the cell walls in the scaffold and the average diameter of the ensuing porosity are on the order of 5 to 50 μm . Rapid prototyping techniques involving the processing of polymer melts and powders, such as three-dimensional printing techniques have also received considerable attention. In these techniques, complex free-form parts can be readily produced from computer-aided design (CAD) models. The drawback is that they are time consuming and require sophisticated equipment. Further, the maximum porosities obtained are limited to approximately 80%. Electrospinning of porous structures from polymer solutions may be used to

overcome some of the drawbacks with the techniques outlined above.

Electrospinning is a technique where the high voltages are applied to a polymer solution to produce porous structures of varying morphologies. If a dilute polymer solution is used, sub-micron sized particles of the polymer can be obtained. At high polymer concentrations in the solution, an interconnected membrane structure with a web of sub-micron fibers, may be obtained. This novel technique provides the capability of integrating various types of polymers, fibers and particles to produce unique porous materials with a structural scale on the order of *nm*. In biomedical applications, drugs, growth factors and/or biomolecules can be incorporated into the solution so that they can be distributed uniformly in the porous structure, thereby enabling zero order release at the targeted site. A wide range of pore architectures can be obtained in electrospun products. In addition, electrospun layers can also be sprayed directly onto 3-D forms, similar to painting of automotive bodies.

Electrospun porous structures and fibers are being considered for many applications including protective clothing, drug delivery systems, wound dressings, vascular grafts and tissue engineering scaffolds. Currently, there are over 40 synthetic or natural polymers which have been electrospun, with research focusing on the structure and morphology of electrospun polymer.

All these advantages have generated considerable interest in electrospinning. A variety of biopolymers including PEO, PVA and collagen have been used to study the characteristics of porous structures produced by electrospinning. The objectives of the present work are to use electrospinning to produce and characterize porous polymer scaffolds with PCL. The effects of process variables such as voltage, solution concentration and deposition distance on the structure have been studied. The physical phenomena associated with the electrospinning process have been

highlighted through high speed digital photography. The feasibility of using additives to the solution to control the structure of the porous construct has been examined.

2. LITERATURE REVIEW

Porous materials are used in many medical applications including wound care products, tissue engineering scaffolds and drug delivery devices. The use of porous scaffolds in the repair and regeneration of tissues has received considerable attention recently. The goal of tissue engineering is to produce biological substitutes which may overcome the limitations of conventional clinical treatments for damaged tissues or organs [1]. One of the principal methods associated with tissue engineering entails growing the relevant cell(s) *in vitro* to form the required tissue, or organ, before implanting into the body. In order to accomplish this goal, the cells must attach to a three-dimensional (3D) substrate, known as a *scaffold*. A temporary three-dimensional biodegradable scaffold that mimics the physiological functions of the native extra cellular matrix (ECM) is used to promote cell proliferation and cell-specific matrix production [2]. The scaffold, therefore, is a key component of tissue engineering. The basic principles of tissue engineering are schematically illustrated in Fig. 1

2.1 Scaffold Materials

The scaffold should satisfy several important requirements crucial for its cellular attachment, proliferation and regeneration processes. The scaffolds are generally made from a biodegradable or bioresorbable material (typically a polymer), that degrades at an appropriate rate with no undesirable by-products, so and is eventually replaced by the host tissue. It is well recognized that viable scaffold materials

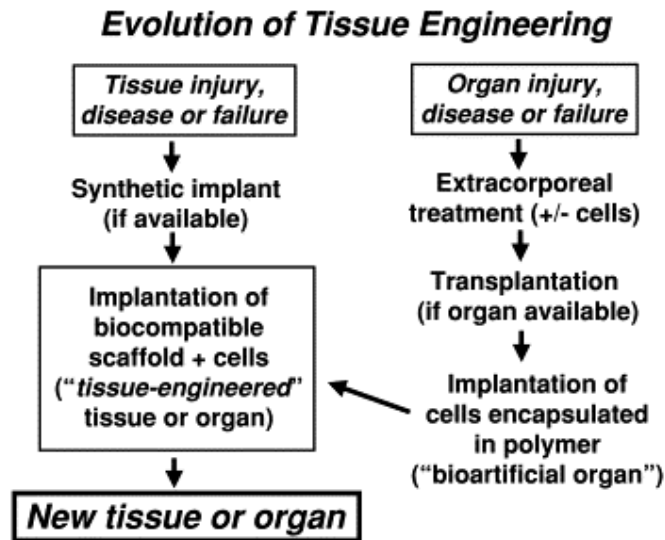


Fig. 1 Schematic showing the evolution of various therapeutic methods based on tissue engineering [1].

should be non-mutagenic, non-antigenic, non-carcinogenic, non-toxic, non-teratogenic and possess high cell/tissue biocompatibility [2]. In addition, the macro- and microscopic properties of the scaffold are also important during cell signaling, growth, regeneration and reorganization. In general, a three-dimensional polymer scaffold should mimic the structural and functional property of the extracellular matrix (ECM). In this respect, the pore structure in the scaffold is crucial for tissue integration and vascularisation. Typically, a scaffold should have high amount of interconnected open pore geometry with more than 90% porosity. The average pore size and distribution should match the type of tissue being regenerated. For example, pore sizes on the order of 200 to 500 μm may be needed for tissue engineering bone, while for mammalian skin optimal pore sizes are between 20 to 100 μm . The scaffolds should have a high surface area to volume ratio in order to accommodate large numbers of cells. The scaffold's mechanical properties should match those of the native tissues. Further, the scaffold should degrade such that it retains sufficient structural integrity until the newly grown tissue replaces the scaffolds' supporting function.

Until recently, synthetic biodegradable polymers, such as aliphatic polyesters, *e.g.* polyglycolic acid, polylactic acid and their copolymers, were the most commonly used polymers for tissue engineering scaffolds. In recent years, the limitations of these polymers in many applications have also led the development of a range of synthetic and natural materials for tissue engineering scaffolds (Table I).

Table I List of biopolymers used in tissue engineering and drug delivery applications [3].

Classification	Polymer
Natural polymers	
Protein-based polymers	Collagen, albumin, gelatin
Polysaccharides	Agarose, alginate, carrageenan, hyaluronic acid, dextran, chitosan, cyclodextrins
Synthetic polymers	
Biodegradable	
Polyesters	Poly(lactic acid), poly(glycolic acid), poly(hydroxy butyrate), poly(ϵ -caprolactone), poly(β -malic acid), poly(dioxanones)
Polyanhydrides	Poly(sebacic acid), poly(adipic acid), poly(terephthalic acid) and various copolymers
Polyamides	Poly(imino carbonates), polyamino acids
Phosphorous-based polymers	Polyphosphates, polyphosphonates, polyphosphazenes
Others	Poly(cyano acrylates), polyurethanes, polyortho esters, polydihydropyrans, polyacetals
Non-biodegradable	
Cellulose derivatives	Carboxymethyl cellulose, ethyl cellulose, cellulose acetate, cellulose acetate propionate, hydroxypropyl methyl cellulose
Silicones	Polydimethylsiloxane, colloidal silica
Acrylic polymers	Polymethacrylates, poly(methyl methacrylate), poly hydro(ethyl-methacrylate)
Others	Polyvinyl pyrrolidone, ethyl vinyl acetate, poloxamers, poloxamines

Among these, aliphatic polyesters polylactic acid (PLA) and polyglycolic acid (PGA) and their copolymers have been used extensively in a variety of tissue engineering constructs and drug delivery devices[4]. PLA can exist in two different stereoisomeric forms, which gives rise to several morphologically distinct polymers as shown in Table II. Typical *mer* structures of PLA, PGA and their copolymers are shown in Fig. 2.

Table II Various morphological forms PGA and PLA

PGA	poly(glycolic acid)
L-PLA	poly(L -lactic acid)
D,L-PLA	poly(DL -lactic acid)
L-D,L-PLA	poly(DL -lactic acid <i>-co-</i> L -lactic acid)
D,L-PLG	poly(DL -lactic acid <i>-co-</i> glycolic acid)
PGA-TMC	poly(glycolic acid <i>-co-</i> trimethylene carbonate)
L-PLG	poly(L -lactic acid <i>-co-</i> glycolic acid)

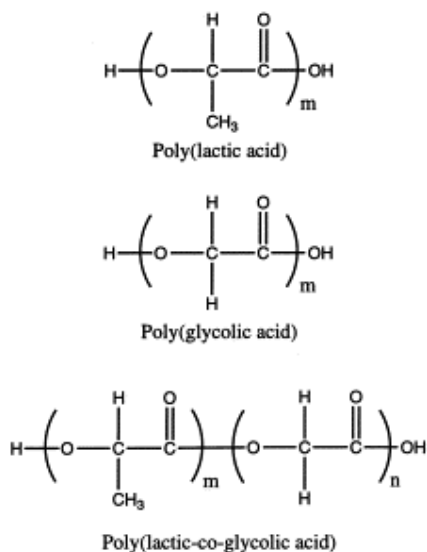


Fig. 2 mer structures of PLA, PGA and their copolymers.

More recently, another aliphatic polyester, Poly(ϵ -caprolactone), (PCL) has received a lot of attention (Fig. 3) PCL is usually more hydrophobic than either PGA or PLA and hence, degrades at a much slower rate than either of these two polyesters. PCL is a semi-crystalline polymer with a low melting point (T_m) and glass transition temperature (T_g) as shown in Table III. PCL is in a rubbery state in room

temperature due to its low glass-transition temperature.

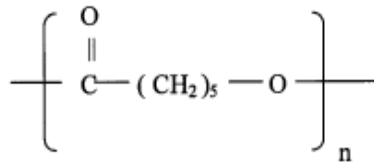


Fig. 3 Mer structure of Poly (ϵ -caprolactone), PCL.

PCL also has a high thermal stability. While most polyesters, have a decomposition temperature between 235 and 255°C, PCL decomposes at temperatures greater than 350°C (Table III). It has also been reported to have an exceptional ability to form blends with a wide variety of polymers [5]. PCL is generally regarded as a nontoxic and tissue-compatible polymer[6.7].

Table III Typical Properties of common Biodegradable Polymers [8]

Polymer	Melting point (°C)	Glass transition temperature (°C)	Modulus* (Gpa)	Elongation
PGA	225–230	35–40	7.0	15–20
LPLA	173–178	60–65	2.7	5–10
DLPLA	Amorphous	55–60	1.9	3–10
PCI	58–63	–65–60	0.4	300–500
PDO	N/A	–10–0	1.5	N/A
PGA–TMC	N/A	N/A	2.4	N/A
85/15 DLPLG	Amorphous	50–55	2.0	3–10
75/25 DLPLG	Amorphous	50–55	2.0	3–10
65/35 DLPLG	Amorphous	45–50	2.0	3–10
50/50 DLPLG	Amorphous	45–50	2.0	3–10
Bone			10–20	
Steel			210	

Although synthetic polymers have been used extensively in tissue engineering there are many drawbacks. They may possess a surface chemistry that does not promote cell adhesion. In addition, they produce a high local concentration of acidic by-products during degradation that can induce an adverse inflammatory response or

create a local environment in the scaffold that may not favor the biological activity of cells being cultured for tissue engineering purposes. Some of them may also undergo degradation during processing. Despite these drawbacks, they are being used to engineer a variety of tissues with reasonable success.

2.2 Scaffold Fabrication

In order to fulfill these structural requirements, a variety of fabrication techniques have been developed. These include solvent casting-particulate leaching, phase separation, gas foaming, emulsion freeze drying, fiber bonding and a combination of these techniques [5]. A plethora of new fabrication methods have been investigated specifically for the design for tissue engineering. The operating principles of some of the important fabrication techniques are reviewed in the following sections.

2.2.1 *Fiber bonding*

In this process, interconnected fiber networks are obtained by depositing a polymer solution onto a mesh of another polymer. For example, PLLA dissolved in a solvent can be deposited on a mesh of PGA fibers. As the solvent evaporates, it leaves behind PLLA and the entire structure can be stabilized or modified through suitable heat treatment. The resulting structure is shown in Fig. 4. This technique is suitable for in many tissue engineering applications, but has several drawbacks including a) trouble of controlling porosity and pore size and b) creating complex three dimensional scaffolds.

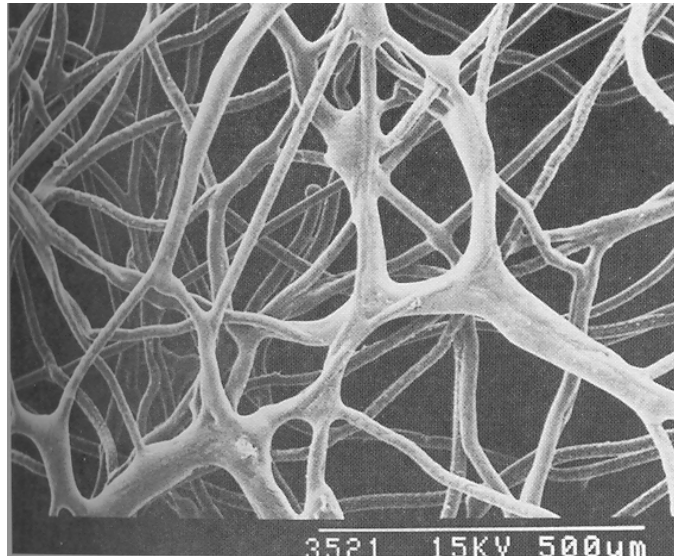


Fig.4 Typical structure in a PGA-bonded fiber mesh, prepared by a fiber bonding technique, embedded in PLLA, heated at a temperature of 195 °C for 90 min and 235 °C for 5 min [5].

2.2.2 Solvent casting and particulate leaching

In this case, insoluble particles are added to a polymer solution that is cast into a mold to produce the desired shape. After the solvent is evaporated a polymer with embedded particles is obtained. The particles can then be leached out by using another solvent in which the polymer is insoluble. Typically NaCl particles are added with synthetic polyesters and water is used as the second solvent to leach out the NaCl. The pore structure can be controlled by controlling the size of particles. Typical structures produced from this process are shown in Fig. 5.

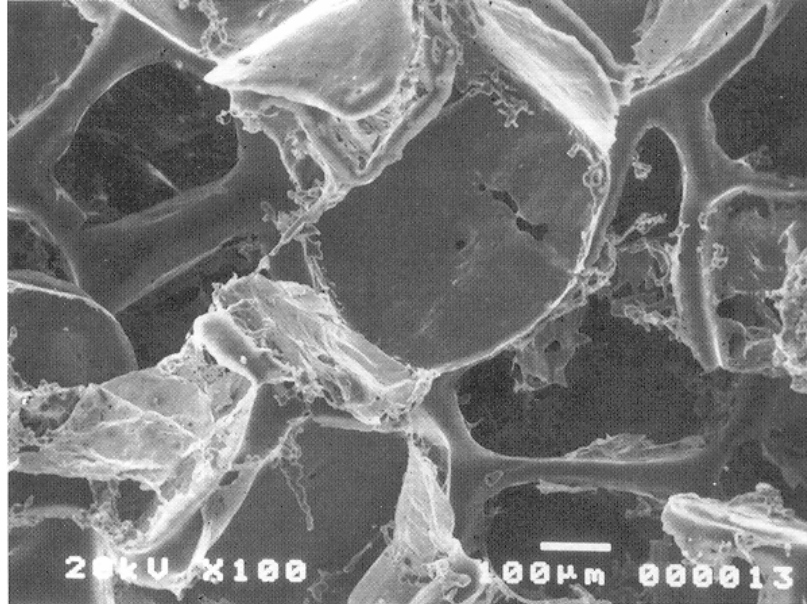


Fig.5 Photograph of a 75:25 PLGA scaffold with porosity, using sodium chloride of size range 300-500 μm as a porogen [5].

2.2.3 Membrane lamination

Three dimensional shapes can be constructed by laminating porous membranes prepared by other techniques. The membranes are contoured appropriately and the 3-D structure is constructed layer by layer. A solvent is used to bond the membranes. A typical structure is shown in Fig.6.

2.2.4 Extrusion

Extrusion has been widely incorporated in the processing of industrial polymers. Recently, it has been developed in combination with the solvent-casting technique to fabricate porous, biodegradable tubular conducts for peripheral nerve regeneration (Fig.7). Although the high extrusion temperature may decrease molecule weight and pore diameter, the salt weight fraction and salt crystal size can be used to control

porosity and pore size.

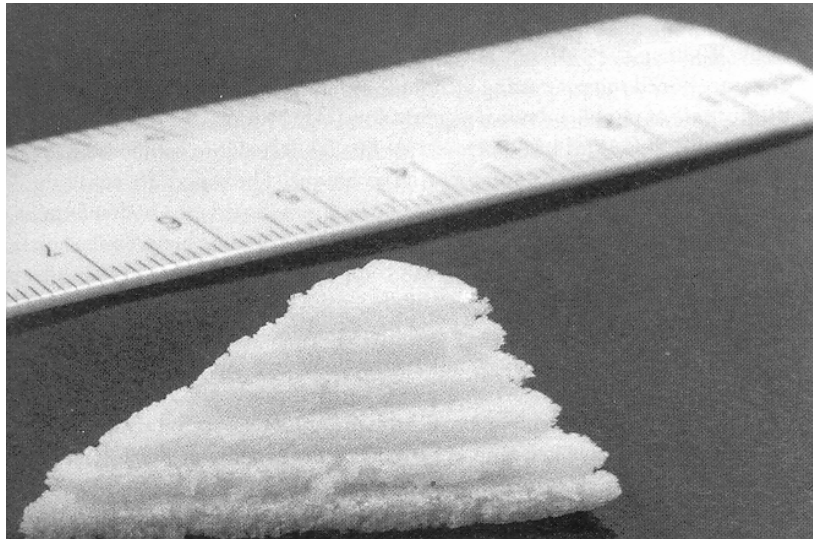


Fig.6 Photograph of a membrane-laminated PLLA scaffold with a nose-like shape [5].

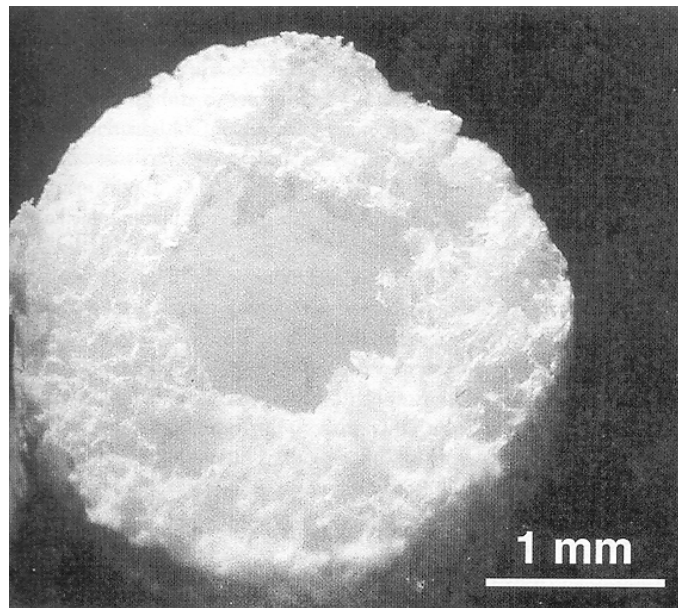


Fig.7 Photograph of a porous tubular PLLA scaffold processed by an extrusion technique for peripheral nerve regeneration[5].

2.2.5 Gas foaming

Gas foaming is an alternative way to overcome the toxic effect of solvent casting and particulate leaching. In this process, salt particles and PLGA pellets are mixed

together and compressed to form solid disks. The pressure is then reduced and the slat particles leached out to produce the final scaffold.

2.2.6 Phase separation

The polymer is dissolved in a solvent and cooled to introduce liquid-liquid phase separation. The resulting structure is quenched to produce a two phase solid. The solidified solvent is removed by sublimation to leave behind a porous polymer structure. This technique is well suited to incorporate biomolecules in the scaffold for eventual site specific release when the polymer scaffold starts to degrade.

The processing techniques mentioned above, although successful, have only resulted in the growth of thin cross-sections of tissue [5]. The primary difficulty is the diffusion constraints in the scaffold, since the pores may not necessarily be interconnected. Since the nutrients are not able to diffuse in and waste products diffuse out, the cells are only able to survive close to the surface. In addition, they also have several other drawbacks including (a) inconsistent macro-and microstructures (b) use of toxic solvents and porogens (c) shape limitations. The advantages and disadvantages of these processes for scaffold fabrication are summarized in Table IV.

In order to overcome the drawbacks mentioned above, the use of solid freeform fabrication (SFF) technology has been examined to produce scaffolds with predefined and reproducible internal morphology [2]. SFF technologies involve building 3D objects of the desired shape using layered manufacturing strategies. There are several commercial variants of SFF technology (e.g. stereolithography, selective laser sintering, laminated object manufacturing, three-dimensional printing, fused deposition

modeling, ink jet printing) and the general process starts with a computer-generated solid model. The solid model can either be designed with the aid of a 3D computer aided design (CAD) package or imported from 3D scanners.. This digital information is then converted to a machine specific cross-sectional format, expressing the model as a series of layers. The file is then implemented on the SFF machine, which produces the physical model in a layer-by-layer fashion. The drawback is that they are time consuming, expensive and require sophisticated equipment. Further, the maximum porosities obtained are limited to approximately 80%.

2.3 Electrospinning

Recently, a relatively new process known as “*electrospinning*” has received considerable attention in the production of porous scaffolds. The electrospinning process can be considered a variation of the better-known electrospray process [9]. It is fairly well established that it is possible to use electrostatic fields to form and accelerate liquid jets from the tip of a capillary. The surface of a hemispherical liquid drop suspended in equilibrium at the end of a capillary will be distorted into a low viscosity liquid (Fig. 8). For high viscosity liquids (~ 1 to 10 Pa.s), the jet does not break up, but travels as a jet to the grounded target. The first case is known as *electrospraying* and is used in many industries to obtain aerosols composed of conical shape in the presence of an electric field. Once a critical voltage, V_c , is exceeded (typically 5 kV for many solutions), a stable jet of liquid is ejected from the cone tip and is accelerated toward the electrically grounded collection target by the macroscopic electric field. As this jet travels through the air, the solvent evaporates leaving behind a polymer fiber (or particle) to be collected on an electrically grounded

Table IV Advantages and disadvantages of processes for scaffold fabrication [2].

Process	Advantages	Disadvantages
Fiber bonding	Easy process High porosity High surface area to volume ratio	High processing temperature for non-amorphous polymer Limit range of polymers Lack of mechanical strength Problems with residual solvent Lack of control over micro-architecture
Phase separation	Allows incorporation of bioactive agents Highly porous structures	Lack of control over micro-architecture Problems with residual solvent Limited range of pore sizes
Solvent casting and particulate leaching	Highly porous structures Large range of pore sizes Independent control of porosity and pore size Crystallinity can be tailored	Limited membrane thickness Lack of mechanical strength Problems with residual solvent Residual porogens
Membrane lamination	Macro shape control Independent control of porosity and pore size	Lack of mechanical strength Problems with residual solvent Tedious and time-consuming Limited interconnected pores
Melt moulding	Independent control of porosity and pore size Macro shape control	High processing temperature for non-amorphous polymer Residual porogens
Polymer/ceramic fiber composite-foam	Good compressive strength Independent control of porosity and pore size	Problems with residual solvent Residual porogens
High-pressure processing	Organic solvent free Allows incorporation of bioactive agents	Nonporous external surface Closed pore structure
High-pressure processing and particulate leaching	Organic solvent free Allows incorporation of bioactive agents Highly porous structures Large range of pore sizes Independent control of porosity and pore size	Limited interconnected pores Lack of mechanical strength Residual porogens
Freeze drying	Highly porous structures High pore interconnectivity	Limited to small pore sizes
Hydrocarbon templating	No thickness limitation Independent control of porosity and pore size	Problems with residual solvent Residual porogens

target. The jet breaks up into droplets as a result of surface tension in the case of sub-micron drops with narrow distributions. When applied to polymer solutions and melts, the second case is known as *electrospinning* and it generates polymer fibers

that are sub-micron in diameter. In addition, electrospun fibers may have a sizable static charge making it possible to manipulate them into three-dimensional (3-D) structures during their deposition. Depending on the solution concentration, voltage and other process parameters, porous structures of varying morphologies can be obtained. The process can be conducted vertically (Fig. 8) or horizontally (Fig. 9). Electrospinning or electrospraying can have several advantages. Sub-micron

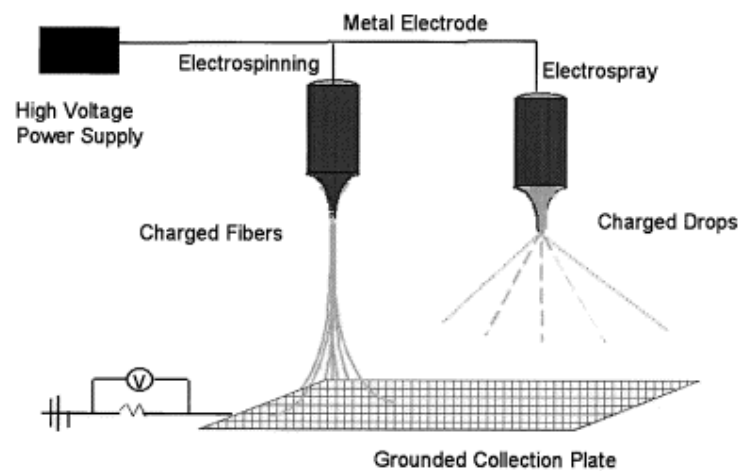


Fig. 8 Schematic of the electrospinning and electrospraying process [9].

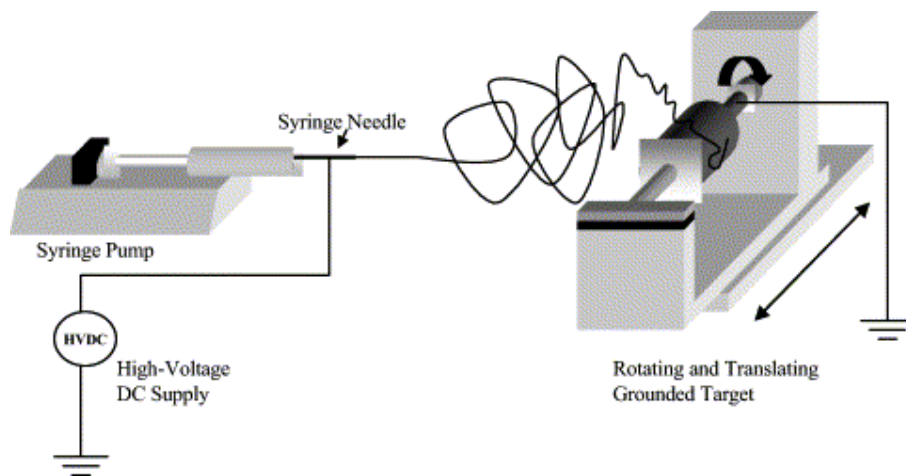


Fig. 9 Schematic of the electrospinning process for producing porous 3-D structures [10].

particles or fibers can be produced with very high surface areas as shown in Fig. 10 [11]. Electrospun 3-D structures may have small pore sizes and very high surface areas, highly suitable for tissue engineering. The degree of crystallinity and orientation in the polymer can be controlled. Drugs, growth factors and/or other biomolecules can easily be added to the solution and be incorporated in the fiber or particles. Multiple solutions can be used to produce graded or layered structures. Organic and inorganic solutions can be used to produce polymer ceramic nano-composites.

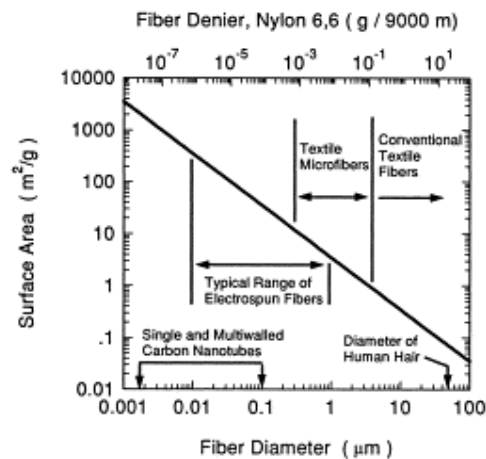


Fig. 10 Surface area in the porous structure as a function of fiber diameter for various processing techniques [11].

The fibers produced by electrospinning belong to non-woven fabrics. More than 40 different types of polymer fibers which have been generated by electrospinning. It has been suggested that this technique can be used to provide a new way to extend the application of biocompatible polymers as a biomaterials[12,13,14,15,16,17,18]. Ko et al.[12] used electrospinning to produce membrane as engineered scaffold of PLGA which have a morphologic similarity to the extracellular matrix of natural tissue and tested its biologic functioning with cells. Hsiao et al.[19] produced PDLA, PLLA membranes and investigated its ability for drug loading and release. Martin et

al.[13,16] used electrospinning to deposit a Silk-Like Polymer with Fibronectin (SLPF) as a thin film onto prosthetic devices designed to be implanted in the Central Nervous System (CNS). Various issues related to electrospinning have been discussed in detail by Reneker et al [19-27].

The mechanism of electrospinning has been studied extensively [13]. Electrospinning can be considered to occur when the surface tension of the solution is overcome by an applied electric field, thereby ejecting tiny jets from the surface. Taylor [28] identified a critical voltage at which this breakdown would occur:

$$V_c^2 = 4 \frac{H^2}{L^2} \left(\ln \frac{2L}{R} - \frac{3}{2} \right) (0.117\pi\gamma R) \quad (1)$$

where V_c is the critical voltage, H , the separation between the capillary and the ground, L , the length of the capillary, R , the radius of the capillary, and γ is the surface tension of the liquid. A similar relationship was developed by Hendricks et al. [29] for the potential required for the electrostatic spraying from a hemispherical drop pendant from a capillary tube:

$$V = 300\sqrt{20\pi\gamma r} \quad (2)$$

where r is the radius of the pendant drop [29]. By examining a small range of fluids Taylor determined that a 49.3° equilibrium angle balanced surface tension with electrostatic forces, and used this value in his derivation. Taylor cones are important to electrospinning since they define the onset of extensional velocity gradients in the fiber forming process. When $V > V_c$, a thin jet of solution will erupt from the surface of the cone and travel toward the nearest electrode of opposite polarity, or electrical ground. An electrospinning jet can be thought of as a string of charged elements connected by a viscoelastic medium, with one end fixed at the point of origin and the other end free.

When a polymer solution held in a capillary by its surface tension is subjected to an electrical field, a charge is induced on the liquid surface [27]. Mutual charge repulsion results in a force opposing the surface tension forces and shear stresses are set up in the liquid. As the intensity of the electrical field is increased, ions in the solution of like-polarity will be forced to aggregate at the surface of the drop. As a result, the hemispherical surface of the solution at the tip of the capillary elongates to form a cone, known as the Taylor cone (Fig. 11). At sufficiently high electrical fields ($V > V_c$), a charged jet of solution is ejected from the tip of the Taylor cone and will travel to an electrode of opposite polarity (or electrical ground).

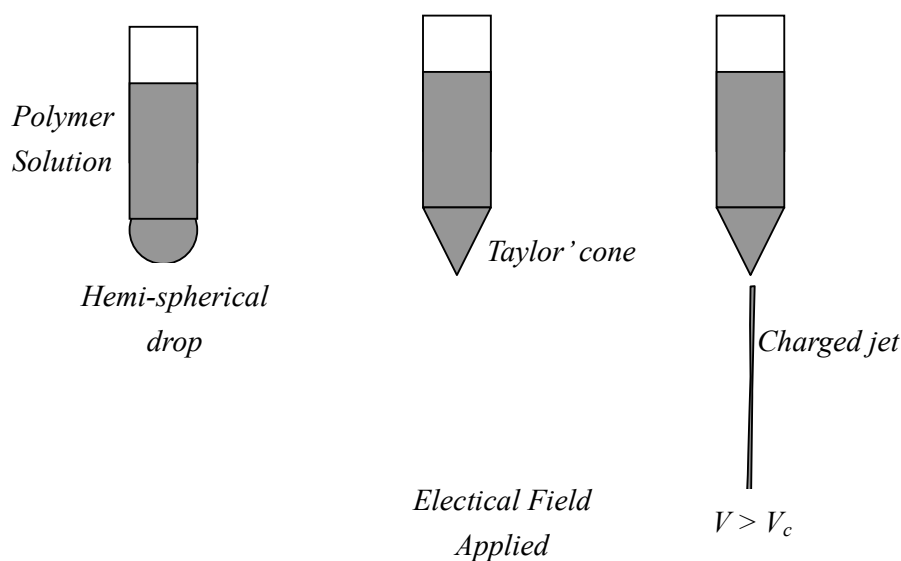


Fig. 11 Schematic illustration of the effects by electric field applied to a solution in a capillary.

Depending on the conditions used during the application of the electrical field, a variety of forced jets may form from the tip of the Taylor's cone as shown in Fig. 12. The characteristics of these jets are shown in Table V. In *dripping* mode, spherical droplets may detach and emerge directly from the Taylor's cone [30,31,32]. In the

spindle mode, the jet is elongated into thin filaments before it breaks up into small droplets. In the *Oscillated jet mode*, drops are emitted from a twisted jet attached to the capillary. In the *precession* mode, a rapidly whipping jet is emitted from the capillary before it breaks into droplets. Most electrospinning is typically conducted in the *Cone jet mode*.

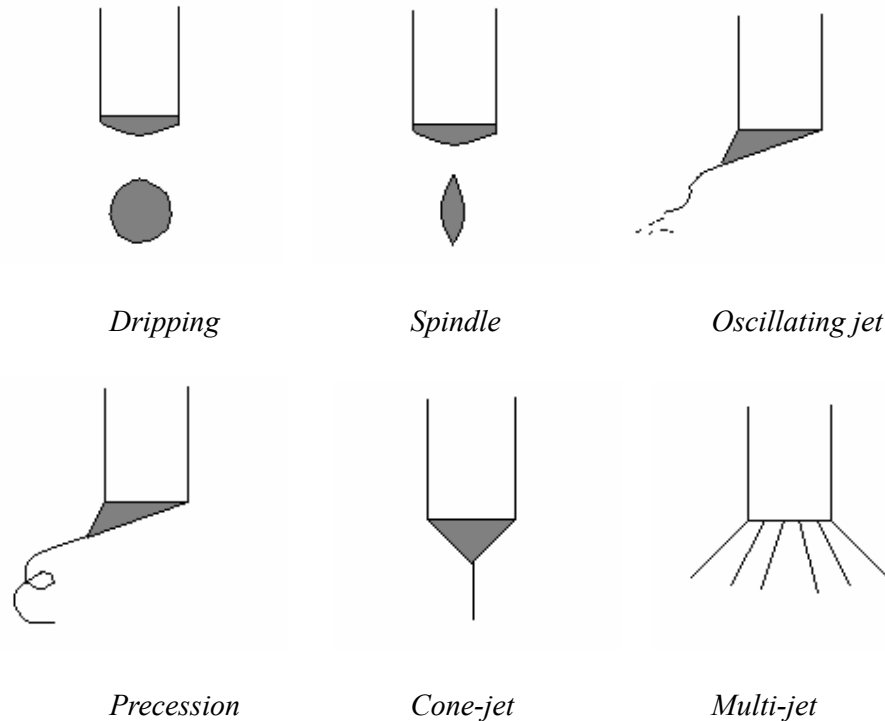


Fig. 12 Schematic illustrating the various modes of charged jet that emanates from the Taylor cone. The essential characteristics of each mode are summarized in Table V [33].

As the jets travel through the air, at some distance from the point of initiation, the viscoelastic fluid begins to experience stress relaxation [21]. The position along the jet at which this stress relaxation begins depends on the strength of the applied electric field. The length of the stable jet increases with increasing voltage. Once stress relaxation occurs, a variety of instabilities may be initiated in the jet as shown in Fig. 13. After the viscoelastic jet starts to flow away from the Taylor's cone, initially it traverses a linear path. The jet slowly starts to bend away from this linear path and

complex shape changes may occur from repulsive forces originating in the charged elements within the electrospinning jet [21]. The jet may undergo large reductions

Table V Summary of the jet characteristics for the different modes shown in Fig. 12 [33].

Mode	Shape of Meniscus	Shape of drop
Dripping	Semi-spherical	Spherical
Spindle	Cone, semi-spherical	Elongated fragments
Oscillating jet	Skewed, oscillating cone	Linear, oscillating in a plane
Precession	Skewed, rotating cone	Spiral, rotating around the capillary axis
Cone jet	Cone	Simple, straight linear
Multi-jet	Flat with small cones on the rim	Linear, multiple

in cross sectional area and spiraling loops may grow from the jet. This phenomenon is usually referred to as *Bending instability*. As a result, the jet can coil and loop as shown in Fig. 14. In the second type of instability known as the *varicose instability*, the centerline of the jet remains straight but the radius of the jet is modulated as shown in Fig. 13. The extent of these instabilities is directly proportional to strength of the electrical field. The last type of instability is the axisymmetric breakdown of a continuous cylindrical column of liquid into spherical droplets *via* the classical *Rayleigh instability*. This instability may be active at low electrical fields, but can be suppressed by high electric fields.

The electrospinning jet can be characterized by 4 regions(Fig. 15): (a) *Base*, a region where the jet emerges from the polymer solution, typically the Taylor cone.(b) *Jet*, region beyond the base, where the electrical force stretches the jet and accelerates the

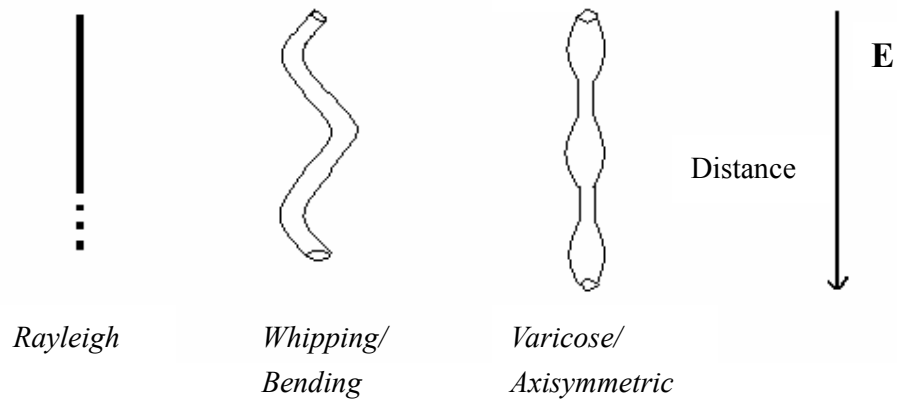
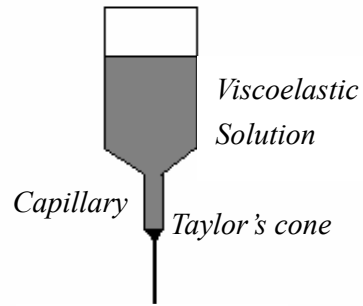


Fig. 13 Various instabilities that may be induced in the viscoelastic jet that is ejected from the Taylor's cone.

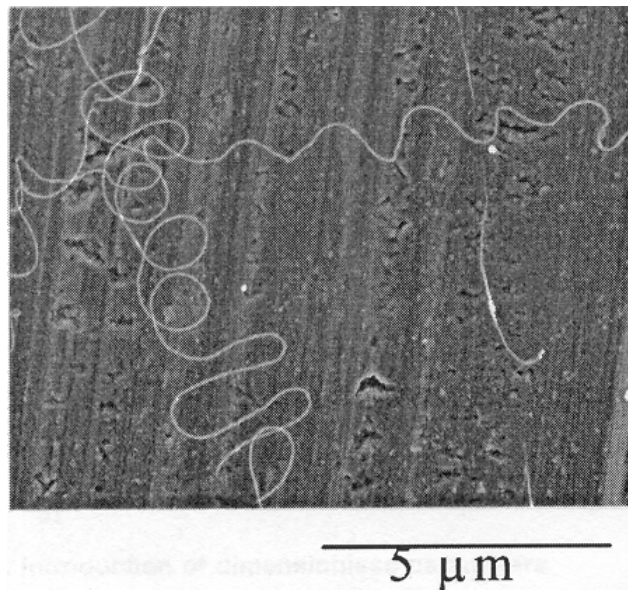


Fig.14. Scanning electron micrograph of coiled or looped nanofibers on the surface of the collector [21].

polymer liquid. The diameter of the jet decreases and the length increases as the jet moves towards the collector. (c) *Splitting and Splaying region*: Splitting refers to the breakup of the jet into two equal parts, while splaying occurs when a single jet divides

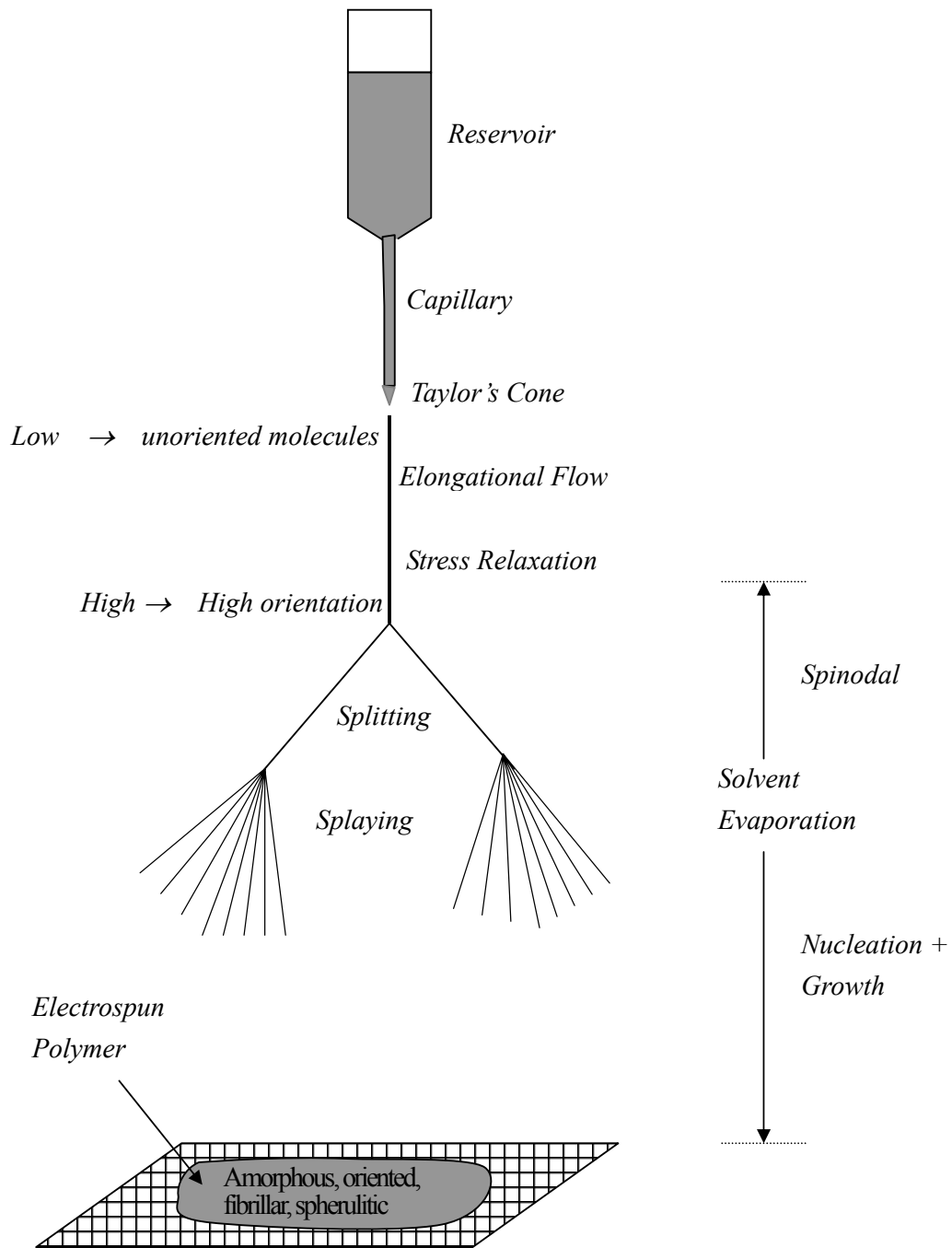


Fig. 15 Schematic illustration of the various physical phenomena occurring during electrospinning a viscoelastic polymer.

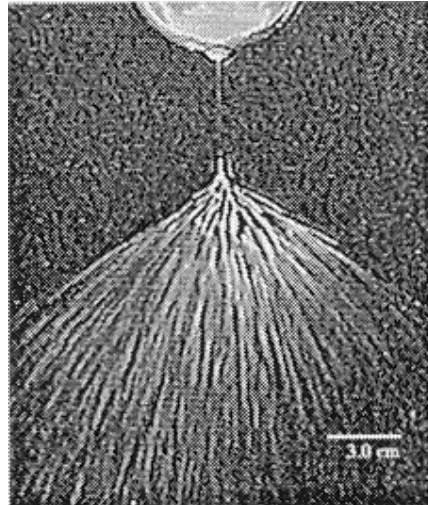


Fig. 16 Example of Splaying in the jet that emerges from the Taylor Cone [21].

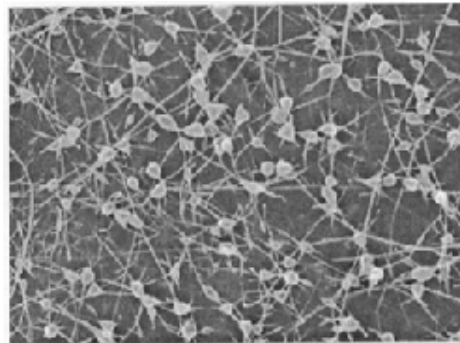


Fig. 17 Example of bead formation during electrospinning. The resulting structure is often referred to as “Bead-on-string” morphology [20].

into many charged jets with approximately equal diameters and charge per unit length. An example of jet splaying is shown in Fig. 16 [21]. In addition, small beads can break up from the jet if the capillary instability driven by surface tension is prevented by significant viscoelastic stresses (Fig. 17). (d) *Collection region*, where the splayed fibers are collected.

2.4 Shapes of Fibers Produced by Electrospinning

Electrospinning may produce fibers with a variety of cross-sectional shapes. Round fibers, branched fibers, flat fibers, split fibers, and collapsed bead fiber have all been produced with various polymers. An example of a round fiber is shown in Fig. 18.

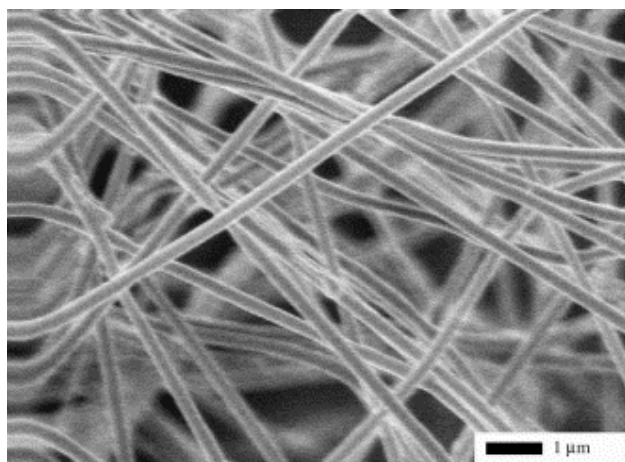


Fig. 18 Photograph showing electrospun PEO fibers with generally circular cross section [32].

The flat fiber shown in Fig. 19 may be generated by the collapse of a hollow fiber during solvent evaporation [22]. A hollow fiber with a bead-on-string morphology may also collapse to yield the structure shown in Fig. 19. Examples of branched and split fibers are shown in Figs. 20. The evaporation of the solvent and elongational flow of the jet can change the shape and the charge per unit area carried by the jet. The balance of electrical force and surface tension shifts quickly, so the shape of a jet becomes unstable. This unstable jet can reduce its local charge per unit surface area by ejecting a smaller jet from the surface of the primary jet. This breakdown leads to the formation of the branched fiber and is similar to the ejection of a jet from a charged droplet. Split fibers can be formed by splitting into two smaller jets from the primary jet [22].

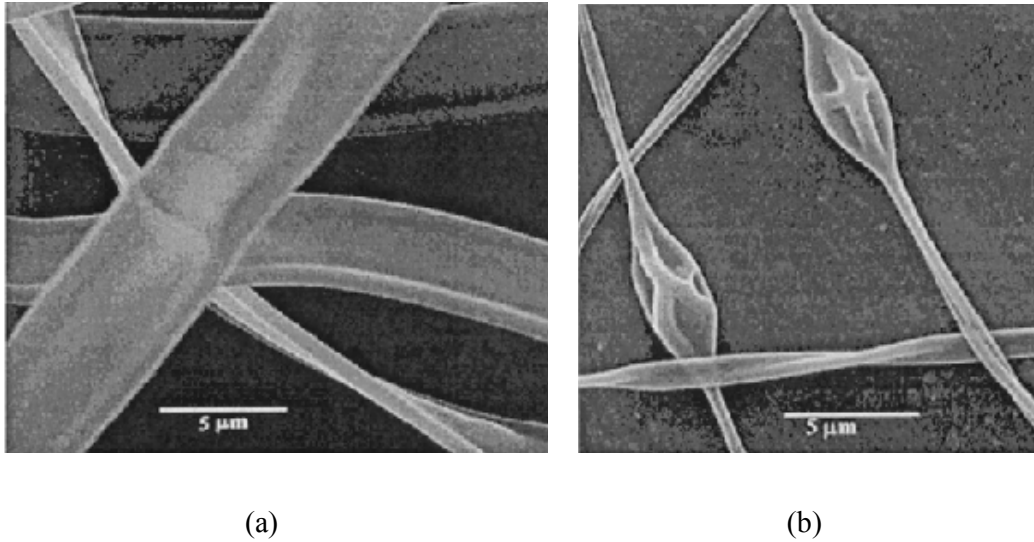


Fig.19 Photograph of flat fibers (a) and toroids (b) produced by electrospinning. The toroids may form by the collapse of beaded fibers [22].

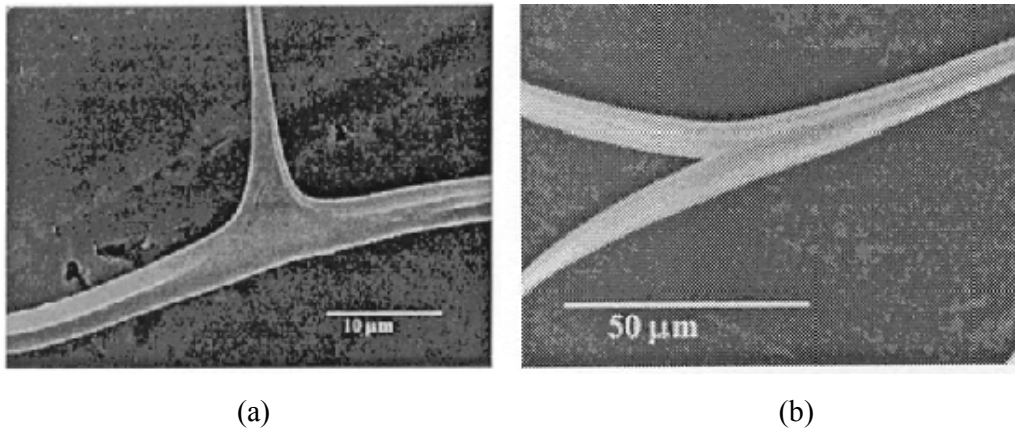


Fig. 20 Photographs showing branched (a) and split (b) fibers formed during electrospinning [22].

2.5 Structure in Electrospun Polymer

Electrospinning can be used to produce novel fibers with the diameters in the range from *nm* to μm . As the solvent evaporates, the polymer molecules can come together by either a phase separation through a spinodal reaction or through classic nucleation and growth of the crystalline phase. As a result, the structure in the polymer deposited on the collector can consist of a totally amorphous, an oriented, a

spherulitic or a textured fibrillar structure shown in Fig. 21. In the fibrils, a *shish kebab* morphology shown in Fig. 22 (typically observed in some semi-crystalline polymers) has been detected in electrospun polyethylene and in electrospun silk [13, 34]. This type of structure was found to result from flow conditions imposed on the polymer solution, and typically comprised a chain-folded lamellae on a fibrillar

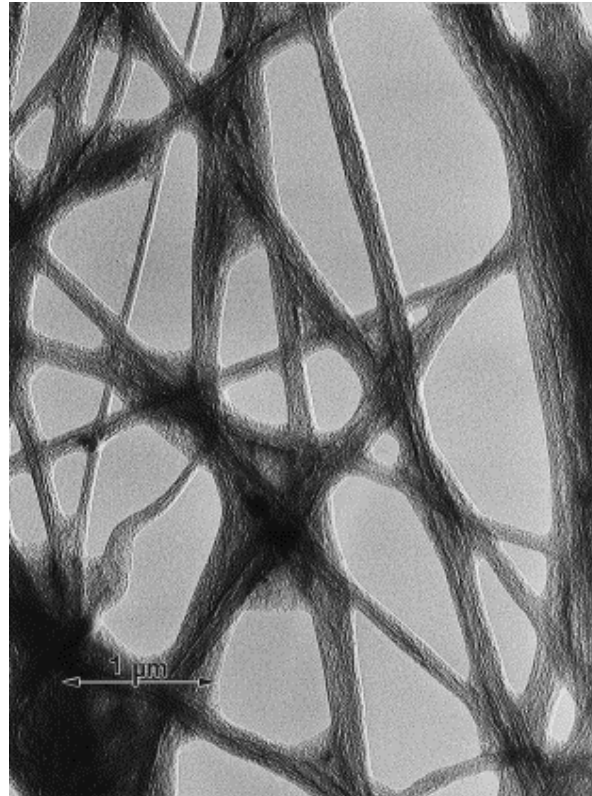


Fig. 21 Bright field TEM photograph showing a fibrillar structure in electrospun products. bright field TEM of electrospun SLPF filaments reveals a fibrillar texture. Crystallites can be seen at the thinnest parts of the filaments [13]

backbone. It is generally recognized that electrospinning may lower the degree of crystallinity in the polymer [9, 35]. The exact reasons for this behavior are not clear. It has been suggested that the development of structure in electrospinning occurs much more rapidly than other processes and this kinetic effect may result in lower

crystallinity [13]. A high degree of orientation may also be observed in the fibrils. The degree of orientation of the molecules in the amorphous regions is directly proportional to the amount of extensional flow.

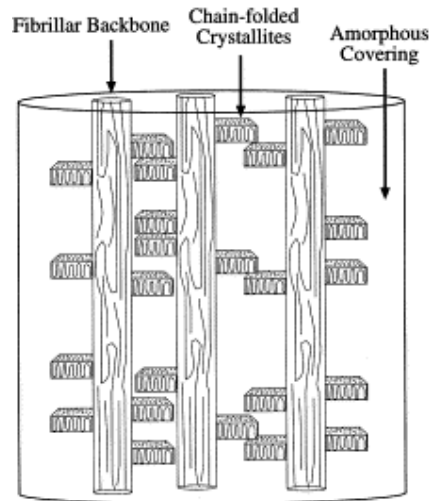


Fig. 22 Schematic of the shishkebab structure of the crystalline region in electrospun silk filaments [13].

2.6 Effects of Process Variables

Many parameters can influence the structure and properties of the electrospun polymer as shown in Table VI. These variables can be related to the base polymer, the solution and the operating conditions. Among these, the effects of applied field strength, solution concentration and deposition rate have been studied extensively in the literature. It has been indicated that the shape of the initiating droplet at the exit of the capillary may depend on the preceding parameters [14]. Consequently, the resulting fiber morphology can be changed by varying these parameters.. The balance between the surface tension and the electric force is critical in the initial formation of the Taylor's cone. When the applied voltage increases, the jet velocity increases and the solution may be discharged from the tip more rapidly. In general, the diameter of

the fiber decreases applied field strength is increased as shown in Fig. 23.

Table VI Various process parameters associated with electrospinning

Polymer	Solution	Process
Molecular weight	Type of solvent	Applied field strength
Polydispersity Index	Concentration	Deposition distance
T _g	Viscosity	Flow rate
	Electrical conductivity	Deposition time
	Dielectric strength	Solvent evaporation rate
	Surface tension	Size of capillary
	Additives	Collection technique
	Temperature	

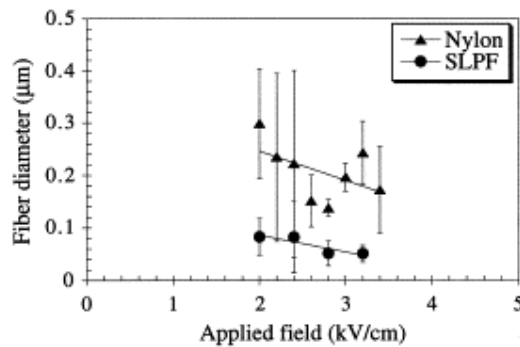


Fig. 23 Effect of applied field strength on the average fiber diameter [13].

The solution concentration has a major effect on the structural morphology and fineness of the electrospun polymer. The concentration may affect the viscosity and surface tension significantly as shown in Fig. 24. There is a minimum concentration or (viscosity), below which the polymer flow rate is too high to stabilize the jet. Beyond this lower limit, a mixture of large beads (drops) and fibers may be obtained (Fig. 25). As the concentration is increased further, the fibrous structure is stabilized

beyond a critical concentration (or viscosity). Further increases in concentration

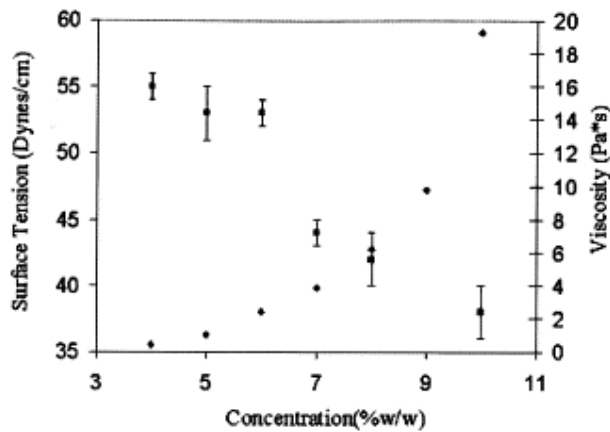


Fig. 24 Viscosity and surface tension of the polymer solution as a function of concentration [9].

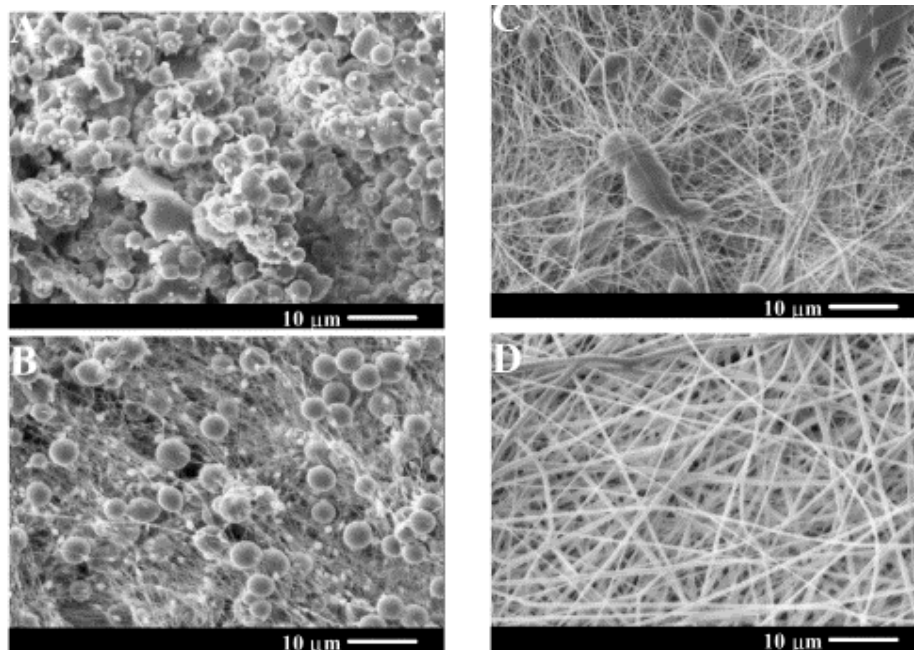


Fig. 25 Effect of solution concentration on the structure of electrospun D,L-PLA fibers A. 20 wt% B. 25 wt% C. 30 wt% D. 35 wt%. [14].

result in an increase in the diameter of the fiber. For each polymer-solvent combination, there is also an upper limit of concentration, beyond which the droplet at the tip of needle dries out before the onset of a stable jet. Between this lower and

upper limits in concentration, the morphology (*i.e.* fibrous, bead-on-string etc.), the diameter of the fiber and the interfiber spacing depend strongly on the solution concentration. The effects of concentration outlined above are also reflected in Fig. 26, where the structure in the polymer for various viscosities is shown. At low viscosities, isolated beaded drops are observed. As the viscosity increases, small strands of the polymer appear to connect the beads. The bead structure also changes from spherical to spindle-like. As the viscosity increases further, the number of beads decreases and eventually the beads disappear completely and a fibrous structure is observed. It should be noted that concentration of the polymer is one of the variables controlling viscosity. Other factors including molecular characteristics of the polymer (*i.e.* MW and PI), solvent used, temperature and additives may have an appreciable influence on viscosity and thereby influence the final structure.

The deposition distance also has a significant effect on the morphology and fineness of the electrospun polymer as shown in Fig. 27. Low deposition distances typically correspond to wet fibers or wet drops hitting the surface of the substrate. This impact can lead to collapse, flattening and coalescence of the fibers. Since the solvent may not have evaporated completely upon impact, the wet polymer may promote intra- and inter-layer bonding. At high deposition distance, however, the solvent may evaporate completely and consequently round fibers with a highly open structure may be obtained. However, as the deposition distance increases, the electrical field strength/unit length can be reduced and this may affect the fiber morphology as indicated above. The effects of these process variables on structure are summarized in Fig. 28.

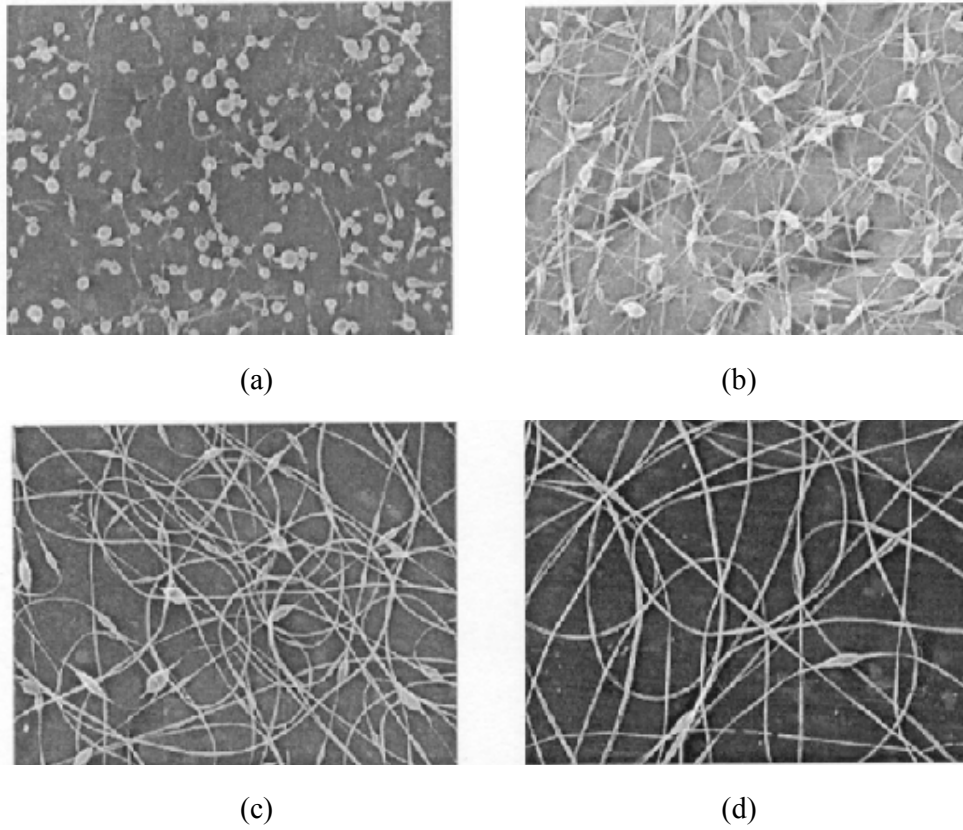


Fig. 26 Effect of solution viscosity on the structure in the electrospun product (a) 13 mPa.s (b) 74 mPa.s (c) 289 mPa.s (d) 527 mPa.s [20] .

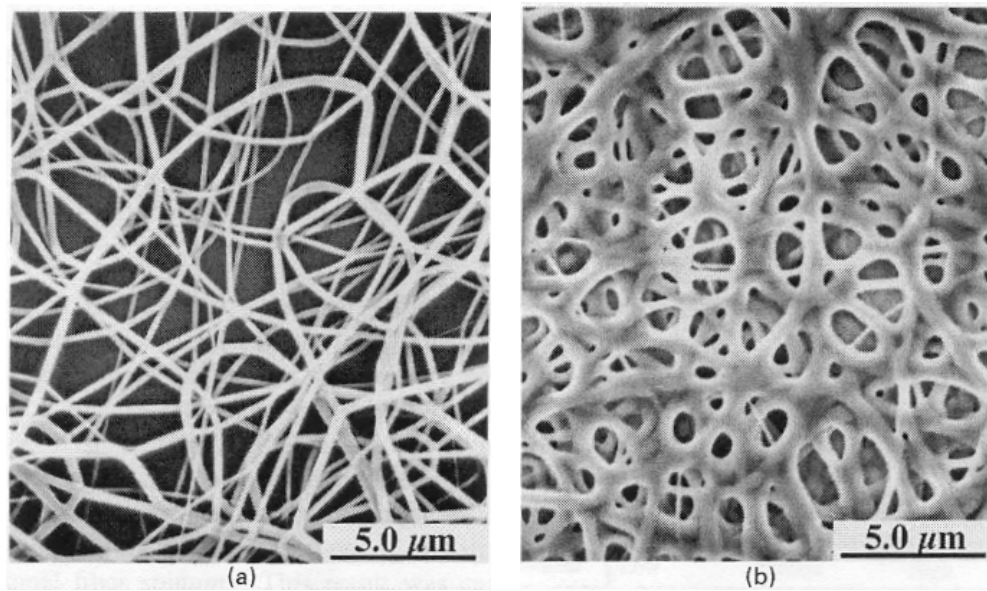


Fig. 27 Effect of deposition distance on structure of electrospun polymer a) 2.0 cm (round fibers) b) 0.5 cm (flat fibers) [13].






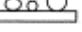






Parameter	Normalized Magnitude		
	Low	Average	High
Solution Concentration top view	 Beads		 Filaments
Deposition Distance side view	 Flat		 Round
Applied Field Strength top view	 Wide		 Narrow
Deposition Time side view	 Thin		 Thick

Fig. 28 Schematic illustration of the effects of process parameters on the the structure of the electrospun product [13].

2.7 Applications of Electrospinning

A variety of synthetic and natural polymers have been used for electrospinning. Biodegradable polymers, such as PLA, PGA, PVA, EVA and collagen have been used to produce porous structures for drug delivery, and tissue engineering. The range of microstructures that can be obtained from these polymers can be seen the photographs shown in Fig. 29. Drugs, growth factors and cellular components have been added to the solution to incorporate them in the porous matrix for eventual controlled release [14]. Because the nanofibers exhibit a high surface area to volume ratio and because of the short diffusion distances in the channel, the drug release profiles and degradation properties of electrospun structures are significantly different from those of the bulk films with the same sample thickness. This technique can provide several advantages for controlled delivery of drugs, proteins over extended periods to obtain

zero order release as shown in Fig. 30.

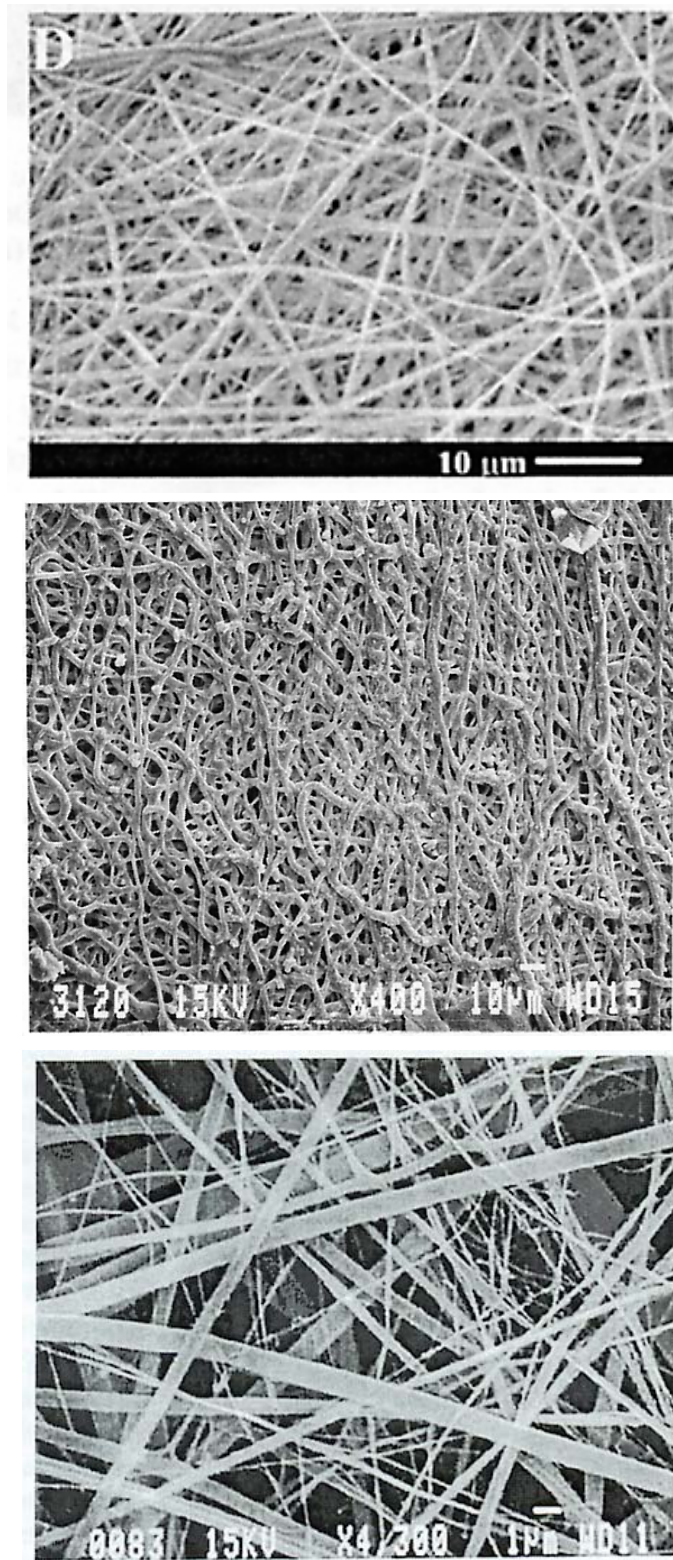


Fig.29 Photographs showing the range of structures that can be produced with various biopolymers by electrospinning.

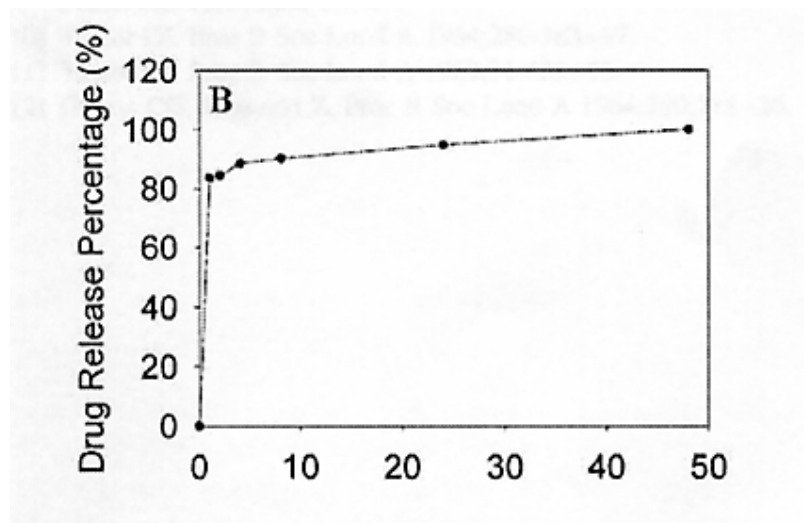


Fig.30 Release profile for Mefoxin from electrospun PDLA membranes [14].

Several investigators have explored the use of electrospun polymer scaffolds for tissue engineering [6]. The architecture of an engineered tissue substitute plays an important role in modulating *in vivo* differentiation and growth. The role of the engineered tissue is to restore and maintain biological function lost in the host tissue. Biologic functioning is regulated by signaling from and between growth factors, extracellular matrix (ECM), and the surrounding cell. Li *et al* [12] indicate that a homogenous, three-dimensional scaffold consisting of a wide range of pore size distribution, high porosity, and high surface area to volume ratio, are ideal for cellular attachment, growth, and proliferation. Such structures can be produced by electrospinning. This novel technique can be used to mimic the architecture of the natural extracellular matrix to produce cell-specific scaffolds. Recently, electrospinning has also been used to produce organic-inorganic nanocomposites [36]. Shao *et al* [36] have used electrospinning to produce PVA/silica composites. Other novel applications include membranes, textiles for protective clothing and coatings [11].

In summary, electrospinning is a novel technique that can be used to produce nano-scale porous structures with a variety of morphologies. The fiber size and distribution and interfiberspacing (*i.e.* porosity) and distribution can be varied significantly by controlling the process parameters. Drugs and growth factors can be incorporated easily into the structure for biomedical applications. The porous structure produced by electrospinning can have a very high ratio between surface area and volume and is ideally suited in applications such as drug delivery and tissue engineering. Although the effects of basic process parameters such as electrical field strength, solution concentration and deposition distance have been studied extensively, many of the basic mechanisms controlling structure formation have not been understood. Since the process can be used to produce novel structures that may be used in diverse applications, it is imperative that various factors associated with structure formation be examined thoroughly.

3. OBJECTIVES

The overall objectives of this work are to develop a suitable processing scheme to produce porous Poly(ϵ -caprolactone) scaffolds by electrospinning. The specific goals are:

- to produce porous polymeric scaffolds from Poly(ϵ -caprolactone) by electrospinning.
- to characterize the structure in the porous polymeric scaffolds
- to study the effects of process variables such as applied voltage, solution concentration and deposition distance on structural parameters
- to examine the physical phenomena occurring during electrospinning through high speed photography
- to determine potential additives to the solution to control the structure in the porous scaffold

4. MATERIALS AND METHODOLOGY

Poly(ϵ -caprolactone, TONE Polymer 767) with a weight average molecular weight of 40,000 g/mol was obtained from Union Carbide Corporation, Danbury, CT. The physical properties of this polymer are shown in Appendix A. Chloroform was as the solvent to dissolve the PCL. In some experiments, (N,N-dimethylformamide), DMF was used as an additive to the solution in order to control the structure. Both these chemicals were analytical grade and were used as received from Sigma (St. Louis, MO).

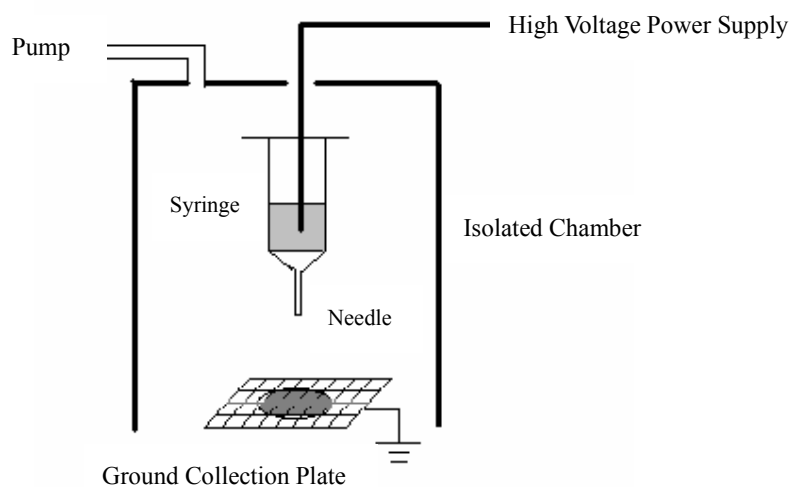


Fig.31 Schematic of the electrospinning apparatus.

A schematic of the electrospinning apparatus is shown in Fig. 31. A solution of the desired concentration of PCL was poured into a 20 ml syringe, typically equipped with 20 gage needle (Inner diameter = 0.58mm, 39 mm long). The flow rate of the solution through the metal capillary was controlled to be on the order of 0.1 ml/min. A copper wire was inserted into the syringe and used to connect to the high voltage

power supply (CPS-60 K02v1, ChungpaEMT, Co., Korea). A copper mesh (100 mm

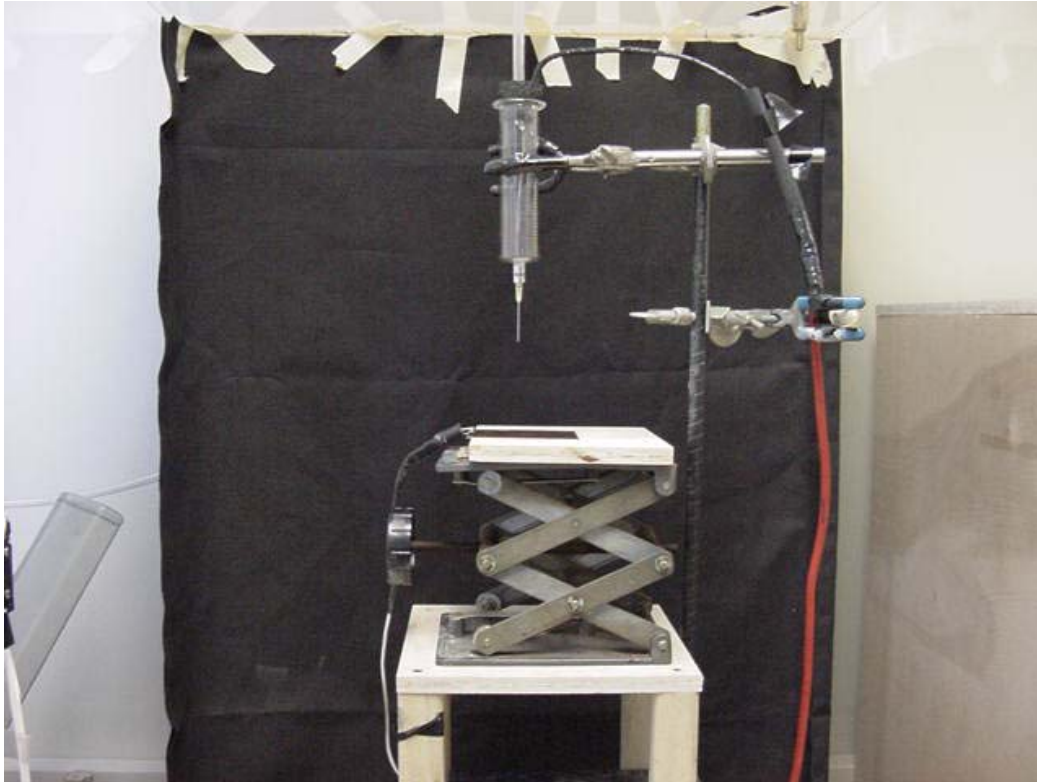


Fig. 32 Photograph of the electrospinning apparatus. .

x 100 mm) with aluminum foil on top was used as the grounded collector. The syringe and the grounded collector were enclosed in a plexiglass chamber. A photograph of the experimental set-up is shown in Fig. 32. When the voltage was applied, a fluid jet ejected from the capillary. This jet accelerated towards the grounded collector and the polymer was deposited on the aluminum foil, typically in the form of a porous non-woven fabric. The voltage was applied for a time of 2 min. After this time, the voltage was turned off and the amount deposited on the collection plate was weighed and stored in a desiccators. When desired, small sections about 5mm x 5mm were cut from the central portions of the deposited layer for microscopic examination. The specimens were mounted on aluminum stubs, sputter-coated with gold-palladium and examined in a JSM-840 scanning electron microscope. The images from the scanning electron microscope were analyzed with *Micosun 2000/s*

image analysis software to obtain data on the distribution of particles and fibers obtained in the electrospun PCL. This image analysis was conducted at magnifications of 1000X, 5000X and 10,000X. At least three images at various locations in the electrospun polymer were analyzed under each condition. The total number of fibers, whose diameters were measured, was typically between 50 and 100.

Differential scanning calorimetry (DSC) was used to study the physical properties of the electrospun polymer. The samples were analyzed in a Perkin-Elmer DSC-7 at a heating rate of 10°C/min. The glass transition temperature, melting temperature and the degree of crystallinity in the sample were calculated from the DSC data.

In order to study the effects of process parameters on the structure of electrospun PCL, experiments were conducted under several different conditions. The effects of applied voltage, solution concentration, deposition distance and capillary diameter were examined (Table VII). The deposition distance was measured from the tip of the needle to the top of the grounded collector. Several experiments were conducted under similar conditions in order to check for reproducibility. In some experiments, DMF (N,N-dimethylformamide) was added to the solution to study its influence on the structure. The ratio between chloroform and DMF was varied from 6/1 to 12/1 (v/v) using 5 wt% polymer solution.

Table VII Summary of experimental conditions used during electrospinning of PCL

Applied Voltage	20 kV, 25 kV, 30 kV, 40 kV
Solution concentration	1 wt%, 3 wt%, 5 wt%, 7 wt%, 9 wt%
Deposition distance	75 mm, 100 mm, 125 mm, 150 mm, 175 mm

Capillary size

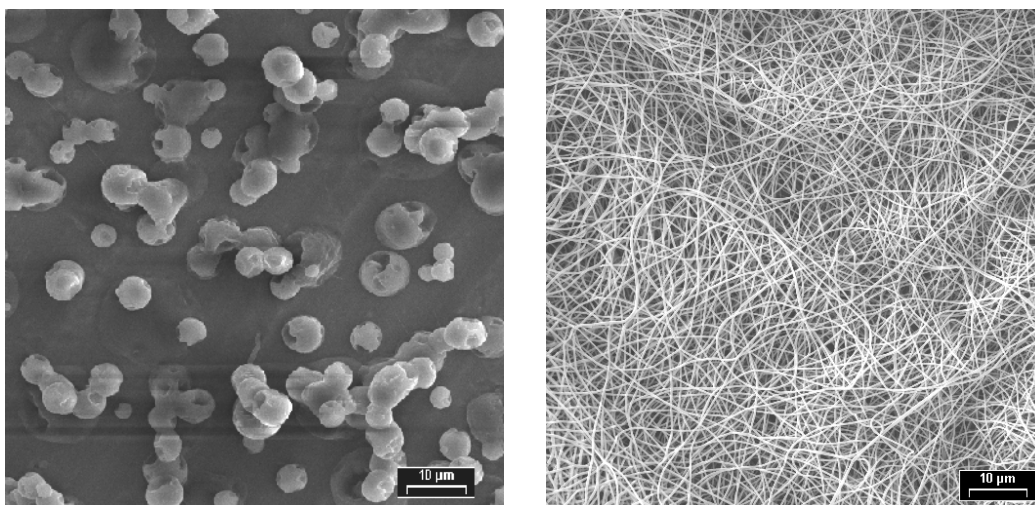
0.9 mm and 0.46 mm

High speed digital photography was used to study the physical phenomena occurring during electrospinning. A sony camera (DCR-TRV900) that can acquire images at the rate of 30 frames/s was positioned outside the chamber so as to record the transit of the polymer from the capillary to the grounded collector plate. The *Avid* software was used to analyze the images.

5. RESULTS AND DISCUSSION

5.1 Structure in Electrospun PCL

The structure in the electrospun polymer for two extreme conditions is shown in Fig. 33. In Fig. 33(a), the polymer was dissolved to produce a dilute solution, where chain entanglements are not significant enough to produce a stable jet (*electrospraying*). In this case, nearly spherical particles can be obtained as the liquid from the tip of the Taylor's cone breaks up into several droplets. If the deposition distance is not high enough for complete solvent evaporation,



(a)

(b)

Fig. 33 Photographs showing the structure in electrospun PCL for two extreme conditions corresponding to electrospraying (a) and electrospinning (b). (a) concentration = 3wt%, $V = 30kV$ (b) concentration = 5wt%, $V = 40 kV$.

some of the particles can agglomerate as can be seen from Fig. 33(a). The breakdown on the jet into droplets may be favored at low molecular weights in the polymer and at low concentrations in the solution. If extensive chain entanglements exist between the polymer molecules, the jet emerging from the

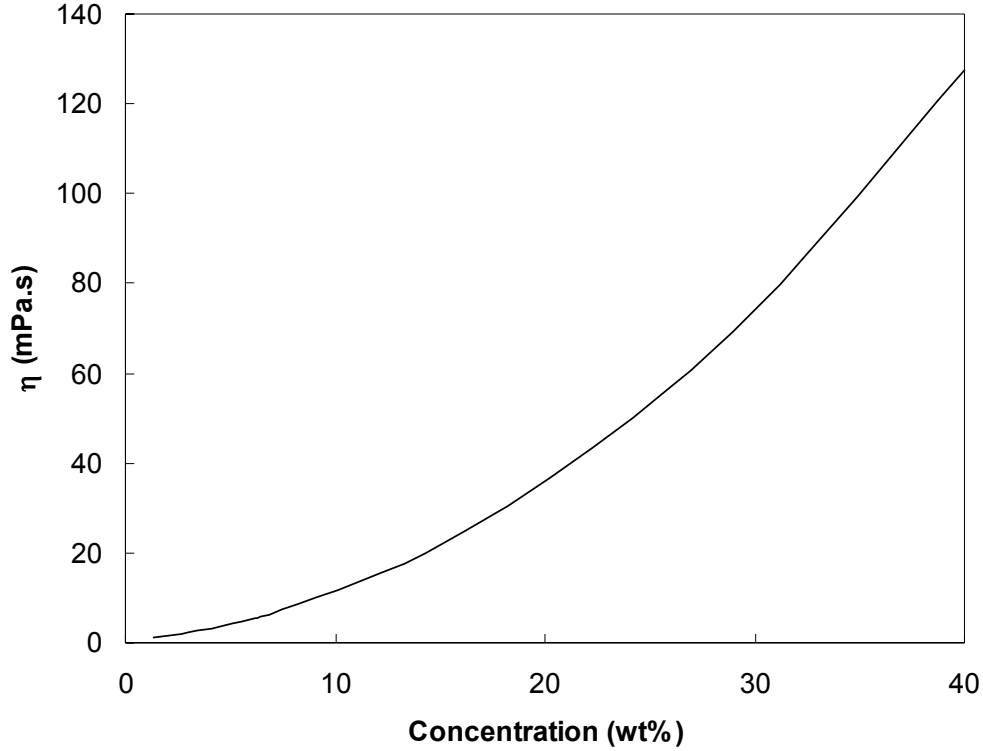


Fig. 34 Calculated variation of solution viscosity with concentration for the chloroform-PCL system.

Taylor's cone is stabilized and the fibrous structure shown in Fig. 33(b) is observed. The onset of significant chain entanglements can be estimated by the variation of solution viscosity with concentration. In dilute solutions, Huggins equation can be used to estimate the viscosity as a function of concentration [37]:

$$\frac{\eta_{sp}}{c} = [\eta] + k'[\eta]^2 c \quad (3)$$

where η_{sp} is the specific viscosity, c is the concentration and k' is a constant that is typically about 0.35 for most polymer-solvent systems [37]. The intrinsic viscosity, $[\eta]$, for PCL can be obtained from the following equation [38]:

$$[\eta] = 9.94 \times 10^{-5} M_w^{0.82} \quad (4)$$

The weight average molecular weight, M_w , for the PCL used in this study was 40,000 g/mol. The viscosity of the solvent chloroform is 0.58 mPa.s [39]. The viscosity of

the solution can then be calculated as a function of concentration as shown in Fig. 34. The onset of the rise in viscosity typically corresponds to a more stable fibrous structure. For example, a stable fibrous structure (eg. Fig. 33(b)) was typically observed above a concentration of 5 wt%. Similar results have been reported by Kenawy *et al* for PLA in chloroform [10].

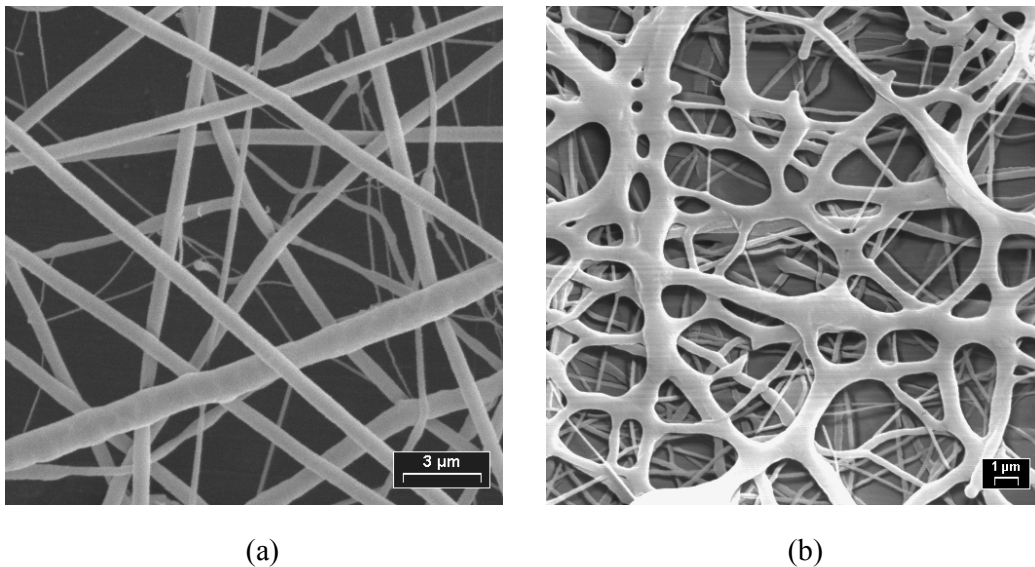
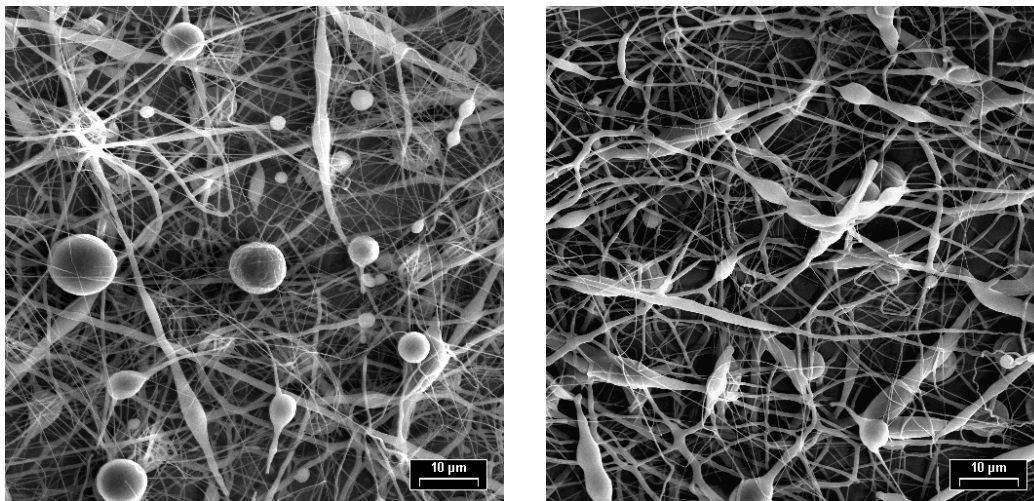


Fig. 35 Photographs showing general fiber crosssections in the electrospun PCL (a) round fibers (b) flat fibers.

Two general fiber morphologies were observed in the electrospun samples as shown in Fig. 35. In the first case, the fibers were generally straight (indicating significant elongational flow) with a round cross section. These fibers are typically observed when the solvent has evaporated completely before reaching the collector. A wide distribution may be observed in the fiber diameter. Flat fibrous structures (Fig. 35(b)) are obtained with wet fibers when the solvent has not evaporated completely. The round wet fibers may flatten upon impact on the collector. The wet fibers may also undergo redissolution and coalescence as indicated by the large size of the fibers in Fig. 35(b). An interesting combination of round and flat fibers can be produced by

controlling the solvent evaporation rate. Such graded structures can be very useful in many tissue engineering applications.



(a)

(b)

Fig. 36 Photographs showing the structure in the electrospun polymer (a) fibers mixed with round beads (b) fibers mixed with spindle-like beads.

The structure shown in Fig. 36, with a combination of fibers and beads was observed under many conditions. Such structures are often referred to as “bead-on-string” structures and are generally related to the instability of the jet of polymer solution [40]. The formation of beaded structures during electrospinning is fairly common and has been reported by several investigators [20]. Although the exact reasons for bead formation are not clear, it has been shown that the viscoelasticity of the solution, charge density in the jet, and the surface tension of the solution are the key factors that control this behavior [20]. At low viscosities (*i.e.* low concentrations), the beads are typically spherical (Fig. 36(a)), while spindle-like beads are observed at high viscosities (or concentrations), as shown in Fig. 36(b). A combination of round and spindle-like beads embedded in the fibers (flat and round) is also observed under many conditions (Fig. 37). Such structures may be especially suitable for some

tissue engineering and drug delivery applications. The small fibers may provide the large surface area desired and the relatively large beads can act as reservoirs of drug or biomolecule that may enable targeted controlled release.

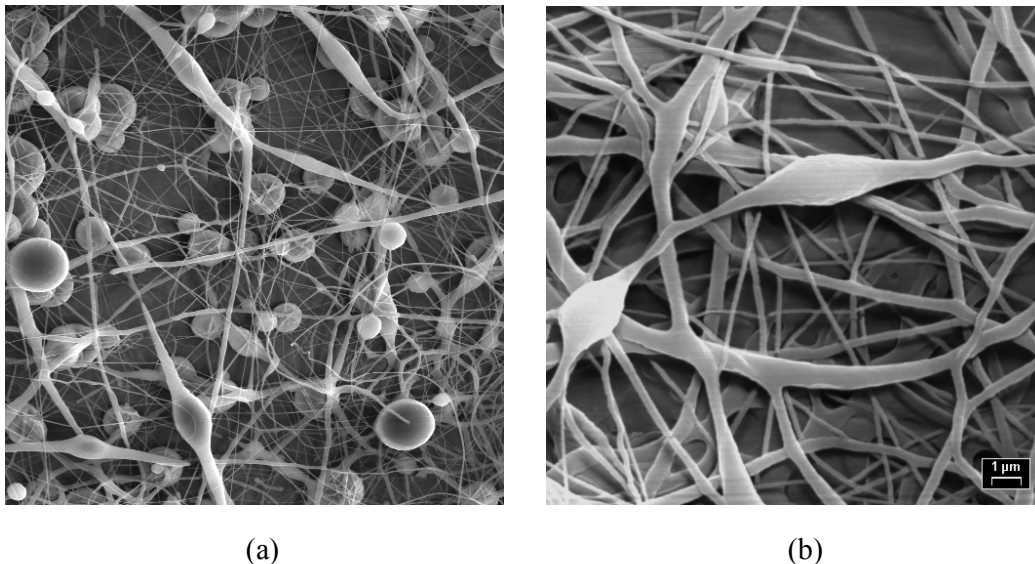
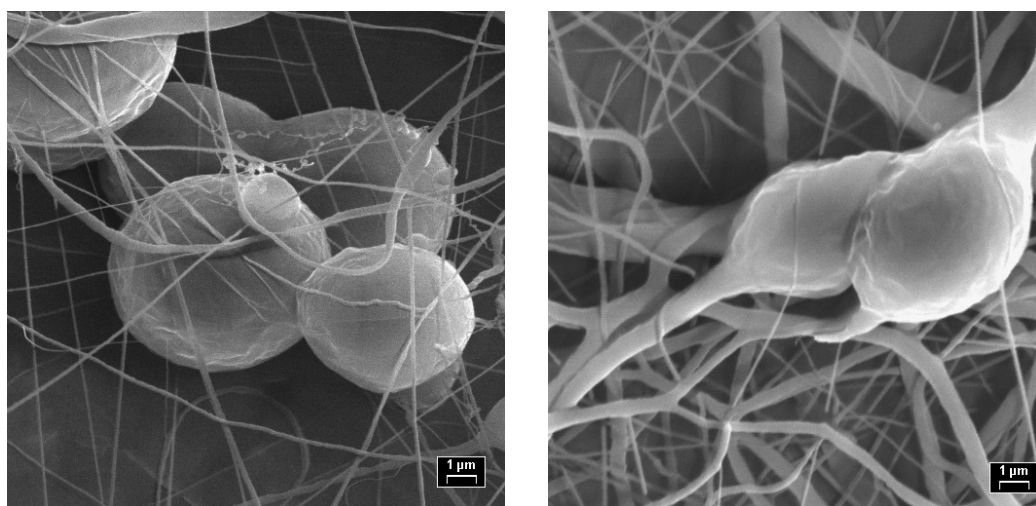


Fig. 37 Photographs showing the structure in electrospun PCL showing “bead-on-string” morphology with a combination of round and spindle-like beads (a) and (b) flat and round fibers and spindle-like beads.

The pattern of breakup of the polymer jet solution is radically different from the breakup of jets in solutions with low viscosity. In polymer solutions, small filaments between the droplets can be stabilized as shown in Fig. 38(a). The coiled macromolecules in these filaments are transformed into highly oriented molecular networks by elongational flow [20]. As a result, the typical bead-on-string structure is produced. In highly viscoelastic polymers, the spherical beads can also be gradually transformed to spindle-like beads by subsequent elongational flow (Fig. 38(b)). Surface tension and viscoelastic properties of the polymer have a major influence on the type of structure produced. The effect of surface tension is to minimize surface area/unit volume and thereby breakup the jet into spherical particles. Viscoelastic forces resist this phenomenon and favor the formation of smooth fibers.

The formation of the final structure is determined by a balance between surface tension and viscoelastic forces. It would appear, therefore, that decreasing the surface tension in the polymer solution would promote the formation of smooth fibers. The surface tension of PCL has been reported to be 40 mN/m[40]. Additives to the solution may be considered to lower this value surface tension to produce predominantly fibrous mats. This aspect will be addressed in the following sections.



(a)

(b)

Fig. 38 Photographs showing stabilized filaments between droplets (a) spherical and (b) spindle-like.

The sample obtained on the grounded collector may contain many regions of unmerged or merged fiber contact, (Fig. 39). If the solvent has evaporated at the onset of contact, there may be side by side growth of the round fibers leading to unmerged contact [13]. Merged contact in the fibers (or fiber merging) may be observed if the solvent has not evaporated at the point of contact. Some of the fiber merging may occur in flight, while some merging can occur upon impact on the collector (Fig. 39). Furthermore, the fibers can be flattened if they are still wet at the point of impact on the collector as can be seen in Fig. 39. Fiber merging of large

fluid segments in wet fibers may lead to the nucleation and growth of small spherulites in these regions [13]. By comparison, the round fibers may exhibit a highly oriented structure with a significant presence of spherulites.

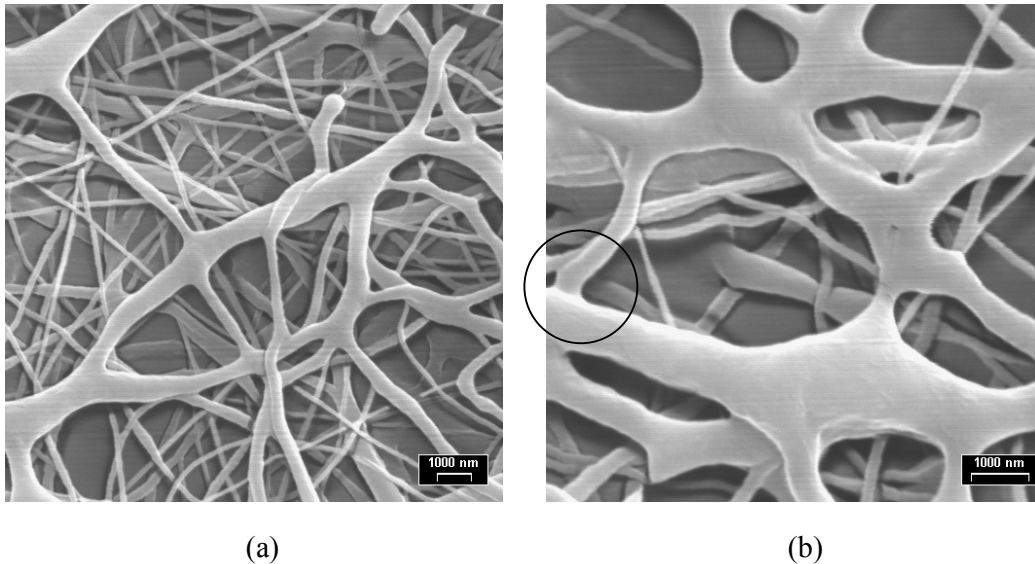


Fig. 39 Photographs showing fibers with large and small diameters. Many points of fiber contact may be observed in the structure. (a) Fiber merging, side by side growth, branching and flattening are observed at several locations. (b) Significant fiber flattening and fiber merging (inset).

The breakdown of the jet through splitting and splaying was discussed in chapter 2. The evidence of splitting and splaying can also be seen in the final polymer structure obtained on the collector. The emergence of many fibers from a bead as shown in Fig. 40 is a result of splaying. Various levels of splaying wherein 2 or more fibers may emerge from a single spherical bead may be observed in Fig. 40. Note also that that the wet beads may coalesce (*i.e.* bead merging) and sinter to produce large particles shown in Fig. 40(c). The photographs in Figs. 40(b) and (c) highlight the effects of bending instability and viscoelastic flow respectively. An examination of the fibers obtained on the collector indicates numerous sites where they may split or

splay. Examples of fiber splitting (or branching) and splaying can be seen in Fig. 41.

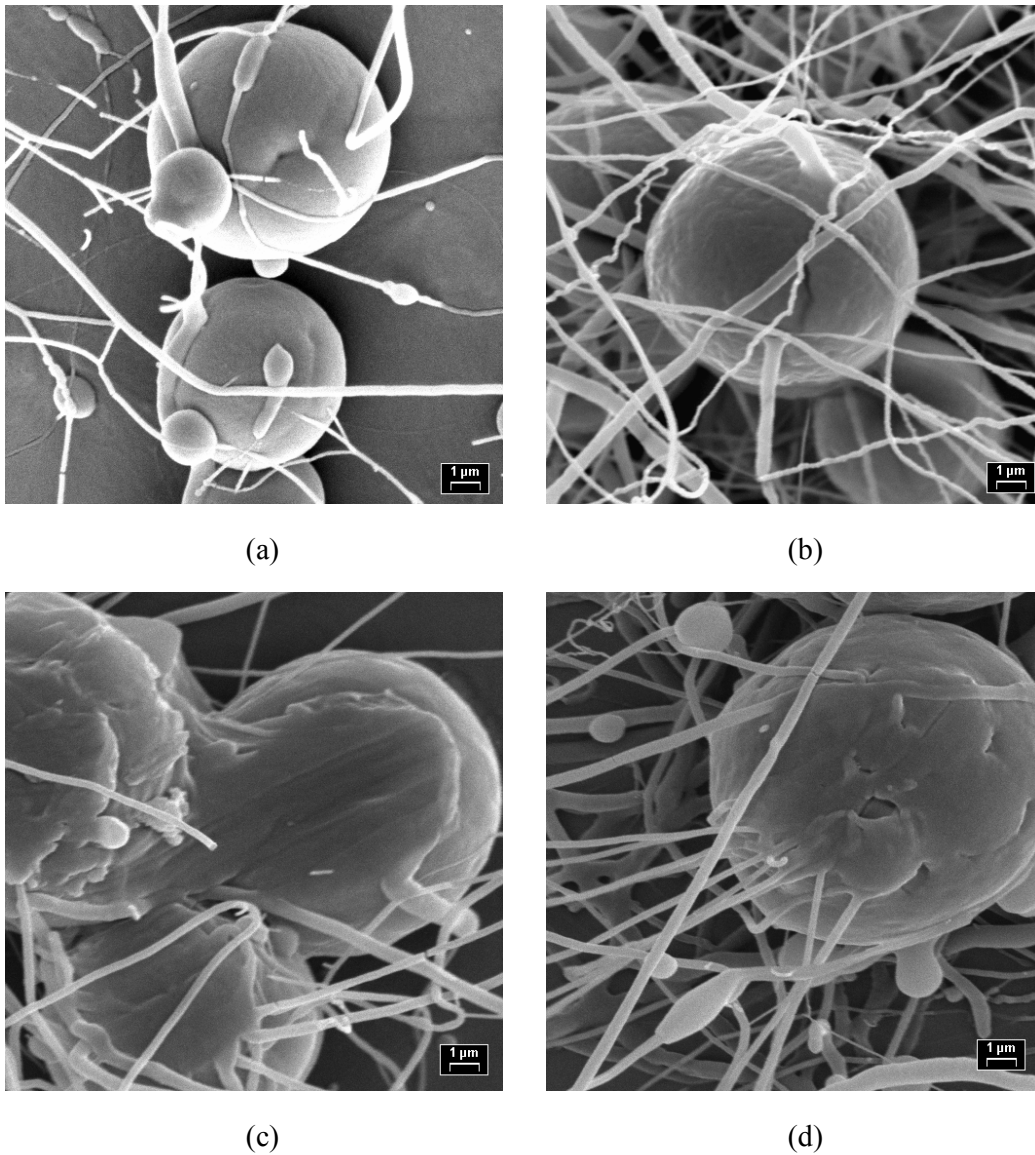


Fig. 40 Photographs showing various levels of splaying from beads.

The fibers exhibit a variety of coils, loops and bends resulting primarily from the bending instability. The coiling and looping can be seen in the photographs of Fig. 42. The bending, coiling and looping can occur over relatively large distances as can be seen from the low magnification photograph shown in Fig. 42. The bending instabilities resulting from electrically driven forces cause the path of the jet to traverse a cone shaped envelope as the jet extends under elongational flow. The

multitudes of open loops that are formed may not come into contact during their transit to the collector, but are grouped together in the dry fibers obtained on the collector. Some fibers can be made up of numerous fibril that have bundled and coiled together to form one thick filament. The surface of the fibers may also exhibit characteristic undulations from the local effects of bending, whipping and Rayleigh instabilities (Fig. 43).

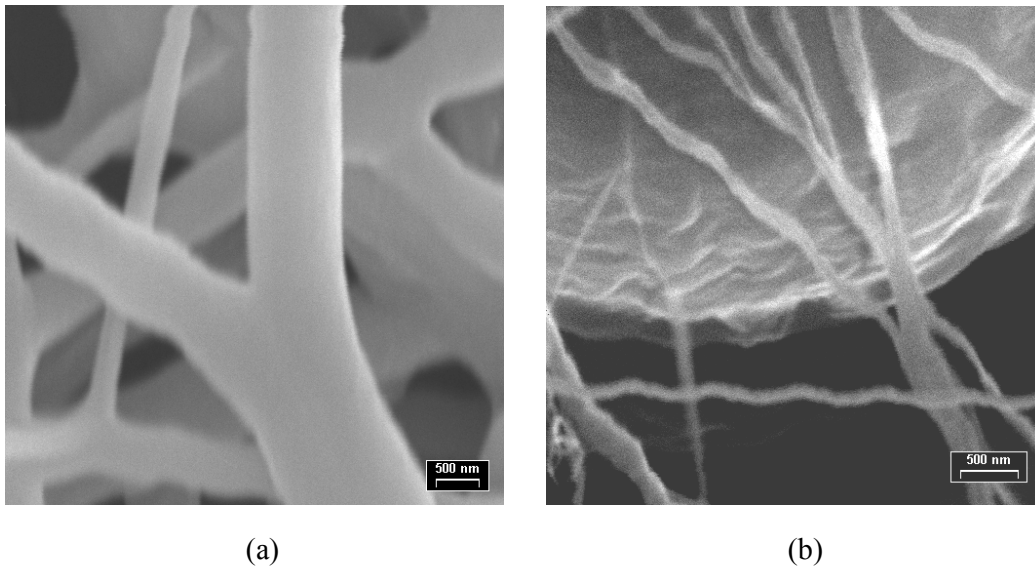


Fig. 41 Photographs showing fiber splitting (a) and splaying (b).

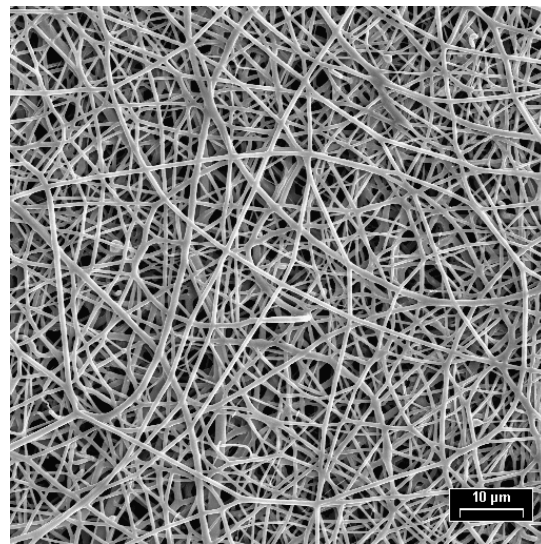


Fig. 42 A low magnification photograph of fibers showing bending, coiling and looping of fibers due to bending instability.

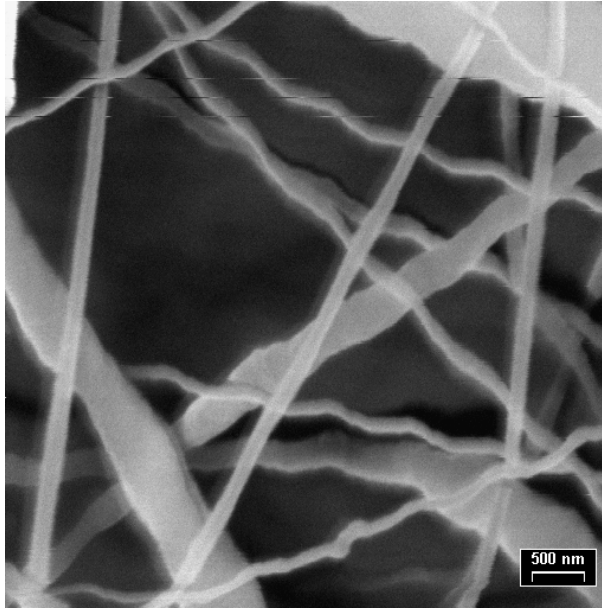


Fig. 43 Photograph showing surface undulations of characteristic wavelength resulting from bending instability.

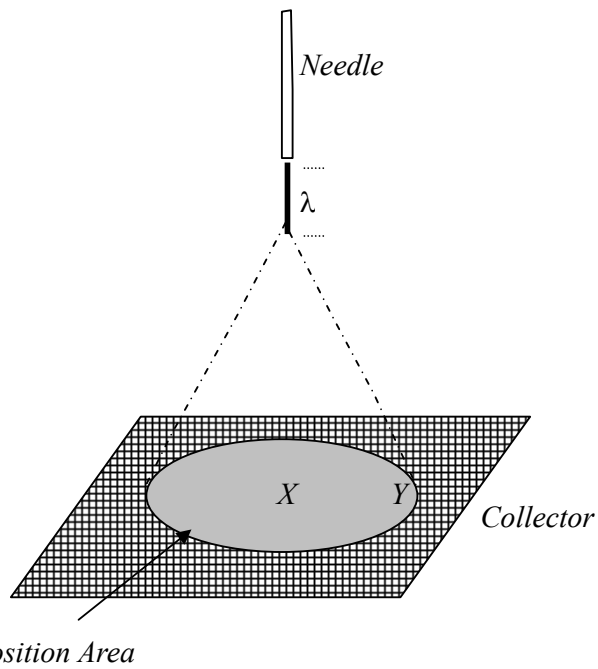


Fig. 44 Schematic illustration of the deposition area. The distance of elongational flow (λ) and the deposition area (A) depend strongly on experimental conditions. In most experiments, the structure was examined at the centre of the deposition area (X).

5.2 Deposition Area

The jet emerging from the Taylor's cone travels towards jet and deposition takes place along a conical envelope as shown in Fig. 44. The characteristics (*e.g.* area) of the conical envelope depend on the conditions used for the deposition such as voltage, concentration and deposition distance. The deposition area was typically between 1 cm² and 5 cm². The structure in the electrospun sample varied from the centre (*X*) to the periphery (*Y*) of the deposition area (Fig. 45). Typically, the central portions contained a lesser number of beads than the outer portions of the deposition area. In addition, the mass deposited in the central portions (*X*) was also higher than on the periphery (*Y*), thereby producing a more compact structure as shown in Fig. 45(a). This behavior can be attributed to the variations in local electrical field strength per unit length of flow (ϵ). The extent of splaying is much larger at position *X* where ϵ is much higher than at position *Y* [22]. In most experiments, the structure at position *X* was examined.

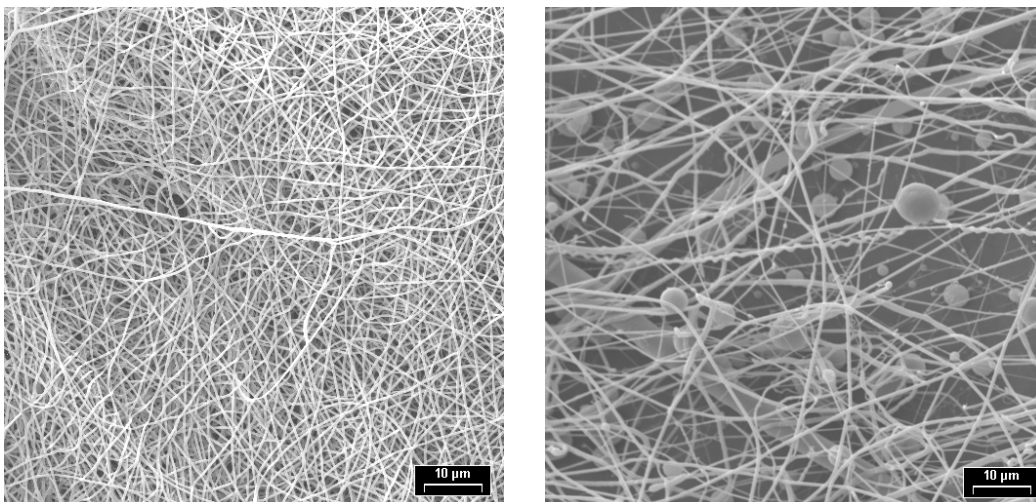


Fig. 45 Photographs showing the structure at (a) the center (*X*) and (b) the periphery (*Y*) of the deposition area. (Concentration = 5wt%, Voltage = 40 kV)

5.3 In situ *Observations*

High speed digital photography was used to study the effects of electrical voltage on the nature of the jet emerging from the needle. In the absence of any electrical field, the dripping of the solution can be observed in the image shown in Fig. 46. As the solution concentration increases, the droplet becomes bigger and the velocity of flow is reduced. The mass flow rate is inversely proportional to the concentration.

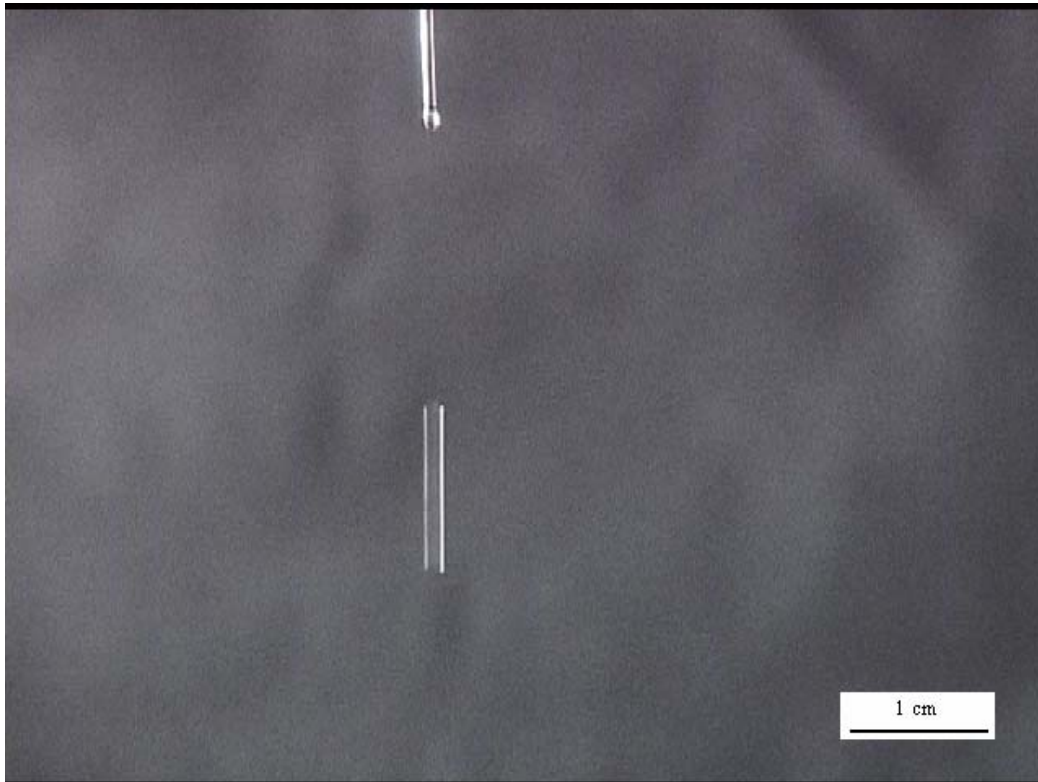


Fig. 46 Photograph showing the dripping of the solution in the absence of an electrical field (solution concentration = 3wt%).

When a voltage is applied, the Taylor cone is generated and at a critical voltage a jet is ejected from the tip of the needle as shown in Fig. 20. This critical voltage, V_c , can be calculated from the Taylor equation [28]:

$$V_c^2 = \frac{4H^2}{L^2} \left(\ln \frac{2L}{R} - \frac{3}{2} \right) (0.117\pi\gamma R) \quad (5)$$

where H is separation distance between the needle and the collector, L is the length of the needle (or capillary), R is the radius of the needle and γ is the surface tension of the solution. The surface tension of PCL in methylene chloride has been reported to be on the order of 40 mN/m [40]. Using this value in eqn(3), V_c was calculated to be 5.1 kV. It was observed experimentally that a stable jet ejected from the needle at a voltage of 5.5 kV and 6.8 kV for solution concentrations of 3 wt% and 9 wt% respectively (Table VIII). These values compare well with the predicted value of V_c . Note that eqn (3) indicates that $V_c \propto \sqrt{\gamma}$, indicating a stable jet may form at a lower voltage as γ is reduced. The data shown in Table VIII indicate that surface tension decreases as the solution concentration is increased.

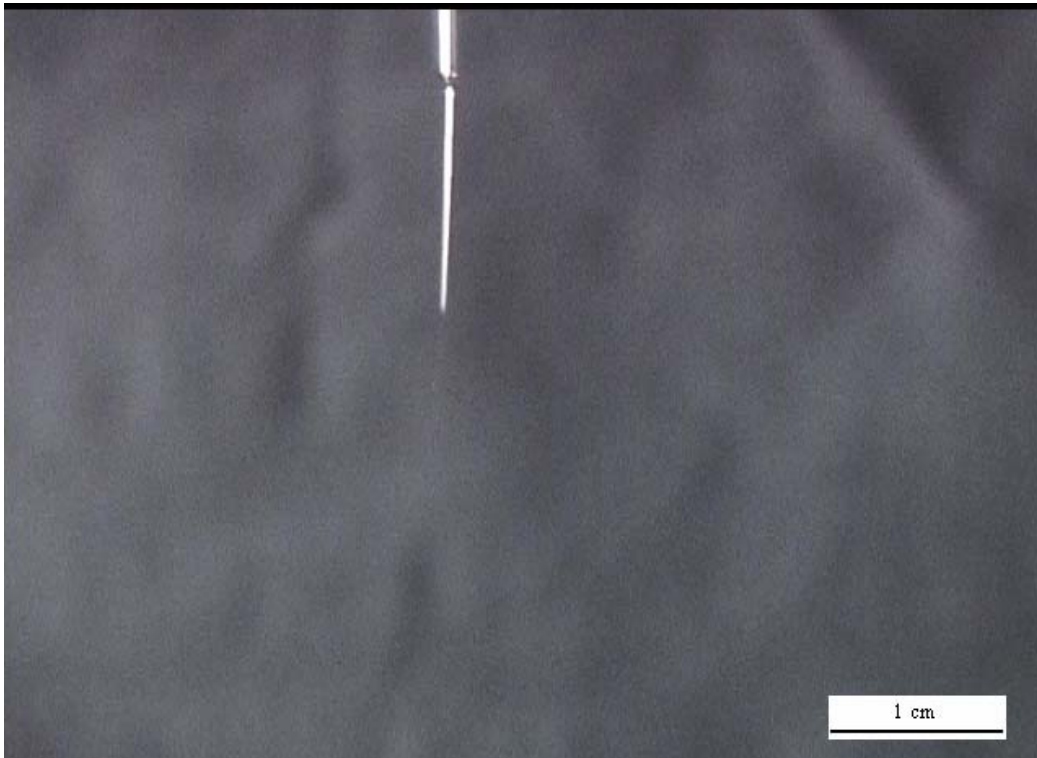


Fig. 47 Photograph showing the ejection of a stable jet from the tip of the needle at a critical voltage.

Table VIII Experimentally measured values of the critical voltage at which a jet shoots out from the tip of the needle. Data have been shown for various solution concentrations. At each concentration, at least 10 and up to 15 measurements were conducted. The measured critical voltages have been used to calculate the surface tension of the solution based on the Taylor's equation (eqn (5)).

Concentration (wt%)	Voltage (kV)	γ (mN/m)
3	6.7±0.7	69
5	6.5±0.6	65
7	5.9±0.6	53
9	5.5±0.4	46

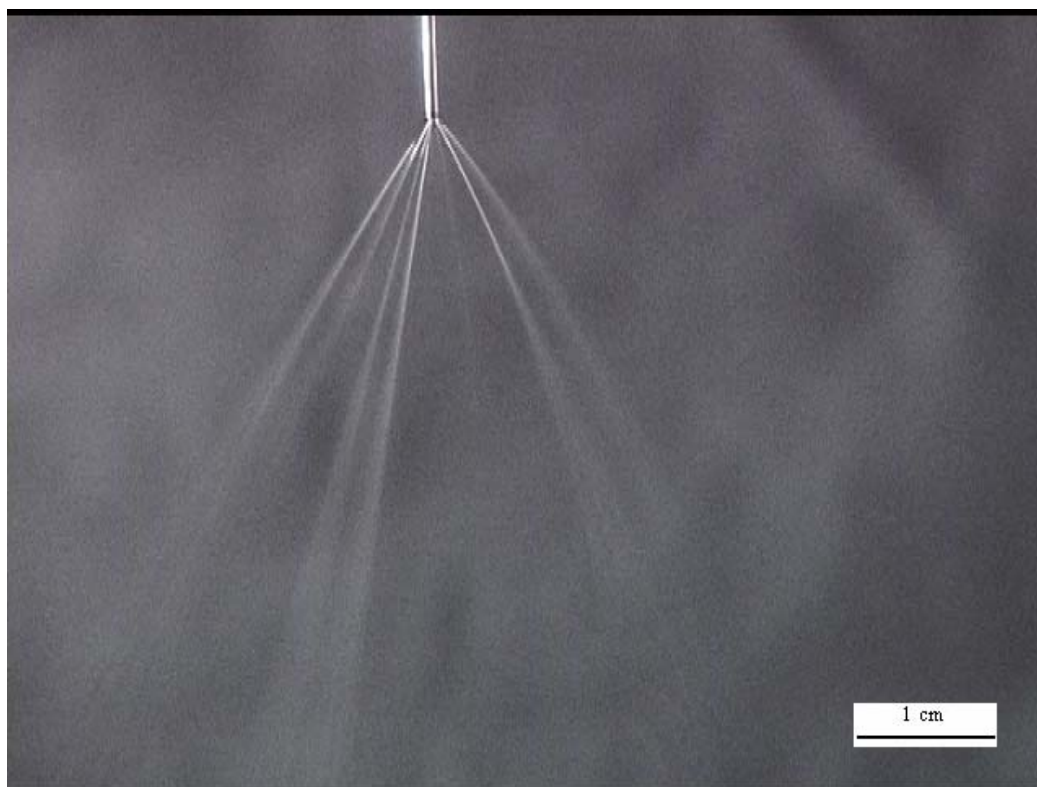


Fig. 48 Photograph showing the breakdown of the jet.

Three major types of breakdown of the jet were identified. After the formation of the Taylor cone, the jet may split into a multitude of major jets almost at the end of the needle. Each major jet can then split into many smaller mini jets, with each jet

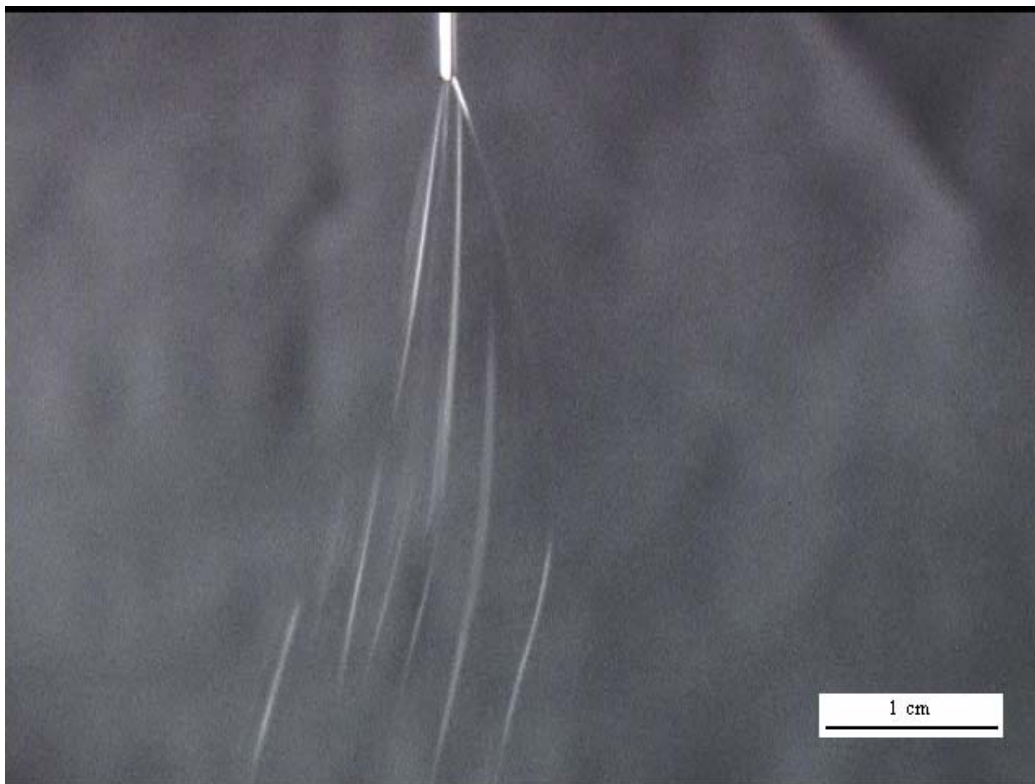


Fig. 49 Photograph showing the breakdown of the primary jet.

gradually disintegrating into small droplets. The electrospun polymer on the collector will consist typically of round powders. This condition represents the sequence of events in electrospraying. In the second type of breakdown shown in Fig. 49, the jet may again split into a multitude of major jets almost at the tip of the needle. As before, each major jet can breakdown into several mini jets, but now the mini jets are stabilized due to high viscosity. The polymer in the mini jet undergoes some extensional flow and is accelerated towards the collector. In this case, a fibrous structure with the typical bead-on-string morphology may be obtained in the final sample. In the last type of breakdown shown in Fig. 50, the jet can undergo significant elongational flow before it starts to splay. This splaying occurs when the radial forces from the electrical charges carried by the jet become larger than the cohesive force inside the jet. After the elongational flow, the jet may divide into

may smaller jets with almost equal diameters. Depending on the local conditions of solvent evaporation and electrical field strength, all three modes of breakdown may be observed in a single experiment. The jet may oscillate between one breakdown mode to the other depending on local conditions. The last 2 types of breakdown corresponding to the photographs in Figs 49 and 50 were typically observed in most experiments. The effects of process parameters such as concentration and electrical field strength on the breakdown of the jet will be discussed in the following sections.

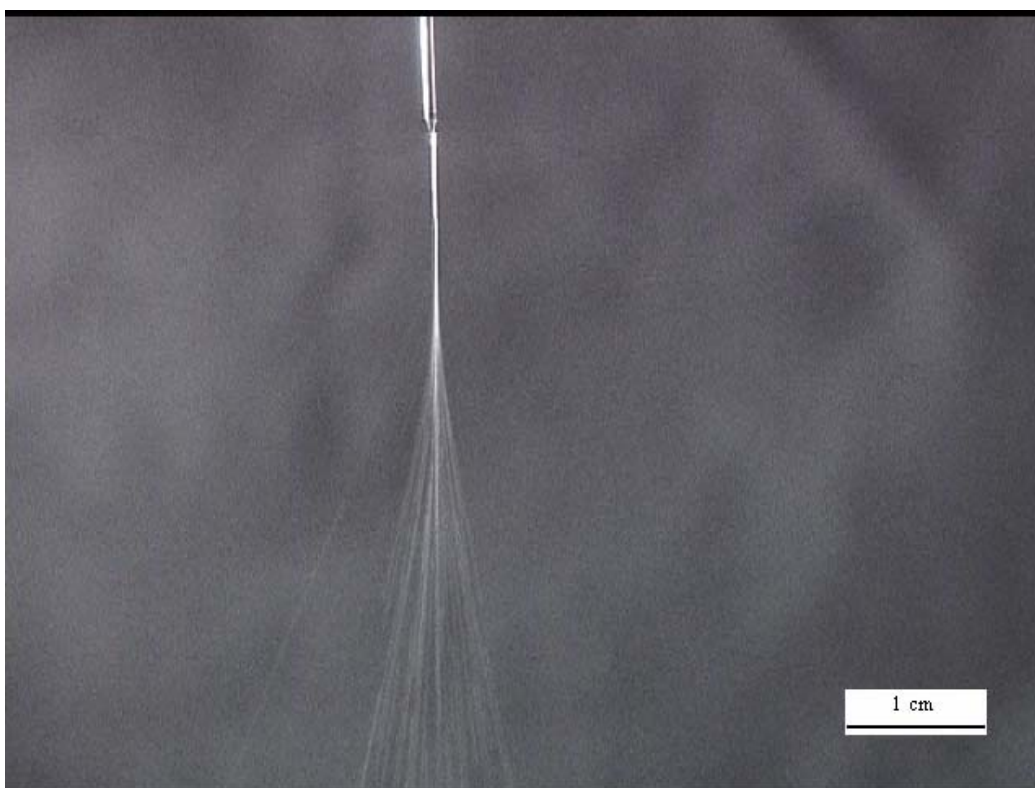


Fig. 50 Photograph showing elongational flow at the tip of the needle and splaying of the jet.

5.4 Effect of Solution Concentration

The solution concentration has a significant effect on the structure in the final polymer obtained on the collector. The viscosity of the solution increases with

concentration and hence, the mass of PCL deposited in a given time decreases as shown in Fig. 51. Typical flow rates were between 0.125 g/min and 1.25 g/min. The deposition area decreases with increasing concentration. For example, deposition areas have been measured to be about 2.0 and 1.5 cm² for solution concentrations of 5 wt% and 9 wt% respectively. As the concentration increases, there is greater amount of elongational flow. This viscoelastic stretching may

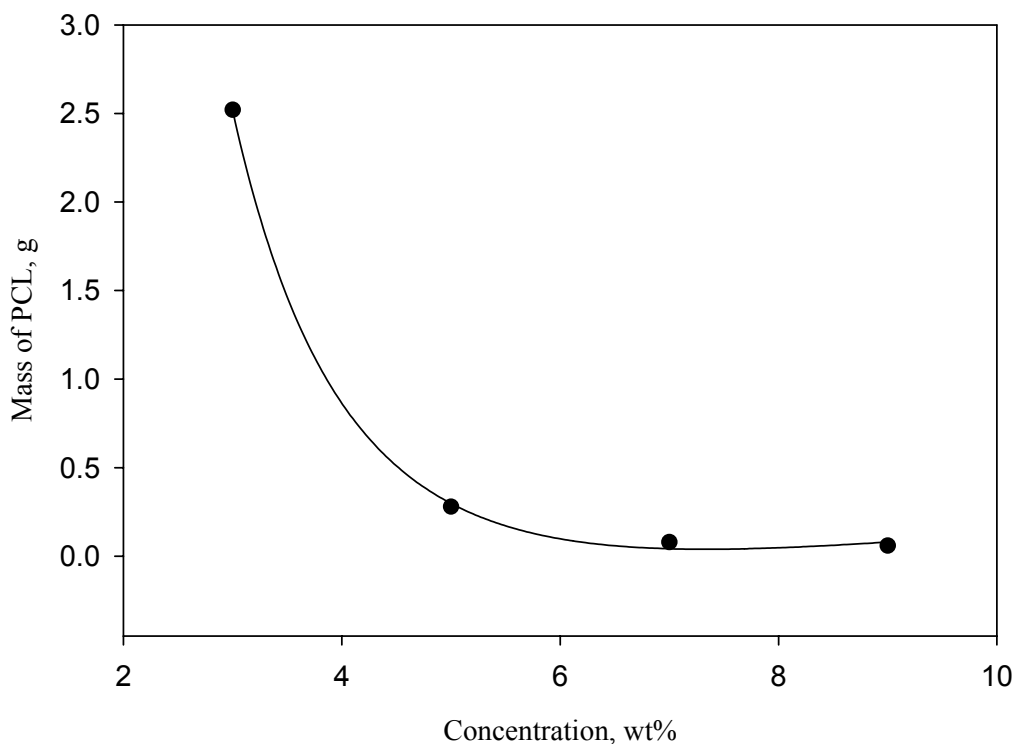
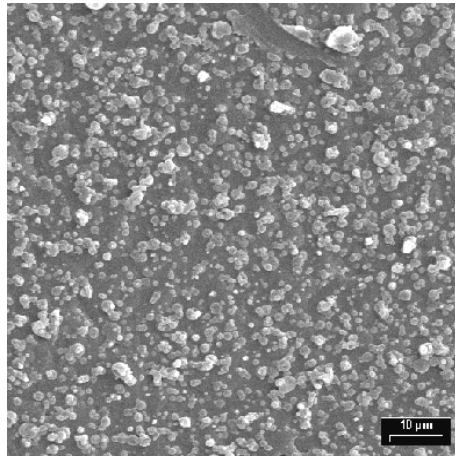


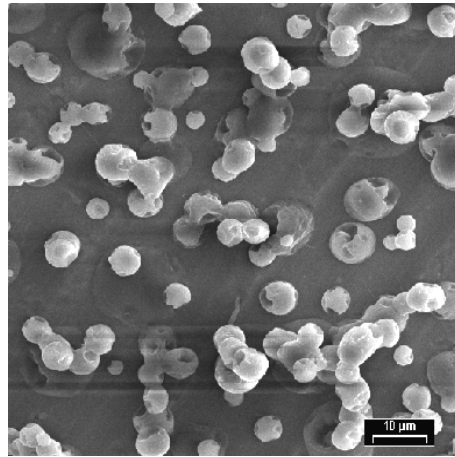
Fig. 51 Mass of PCL deposited on the collector in 2 min as a function of solution concentration (Voltage = 30 kV, Needle size =20 gauge)

reduce the extent of spraying (or droplet formation) and thereby lower the deposition area. Typical structures in the electropun polymer for various concentrations are shown in Fig. 52. At low concentrations (< 1%), the viscosity was so low that the polymer could not be electrosprayed or electrospun. When a 20 gage needle that was typically used with other concentrations was used, the flow rate was so rapid that

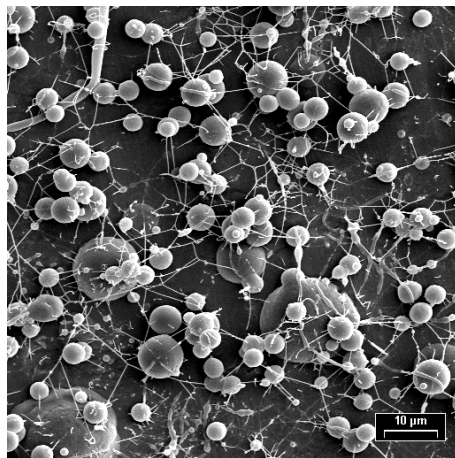
the application of a voltage did not have any significant effect. So, a 26 gage needle was used with this concentration. In this case, a jet of solution of 1 wt% PCL was broken down into droplets (electrospraying) and almost spherical beads were obtained on the collector. These beads are generated by electrospraying due to the low solution viscosity. The mean size of the beads is about 0.9 μm as shown in shown in Fig. 53(a). It was observed that the sub-micron beads were generally spherical while those beads with a diameter greater than 1 μm exhibited an irregular shape. The large beads with irregular shape may be generated because of the agglomeration of small wet beads that reach the collector. Because of the low concentration, the organic solvent may not evaporate completely before the drops strike the collector, leading to surface dissolution and agglomeration. A similar behavior is observed at a solution concentration of 3 wt%, although the average particle size increases significantly as shown in Fig. 53(b). Note that a wide distribution of beads (with some very large beads resulting from agglomeration) is observed at a concentration of 3%. The mean size of the particles is now around 5 μm (Fig. 53 (b)). At this condition, a lot of particles are generated with a thin skin where the solvent evaporates rapidly.



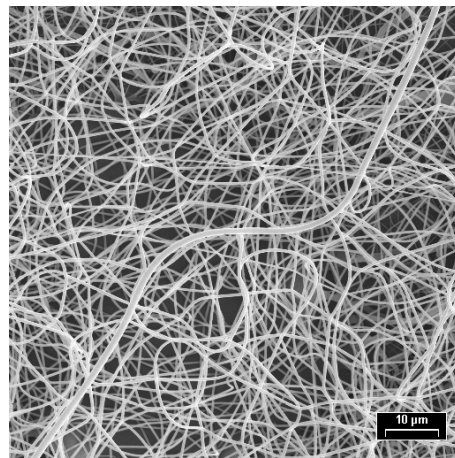
(a) 1 wt%



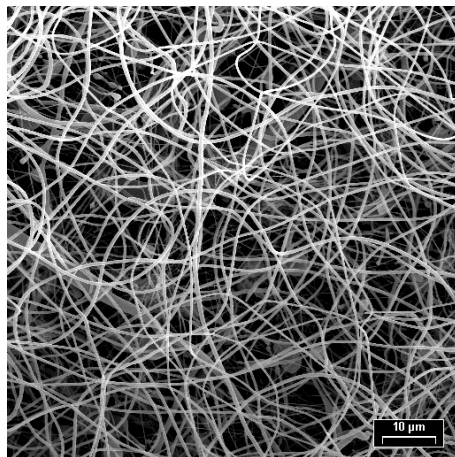
(b) 3 wt%



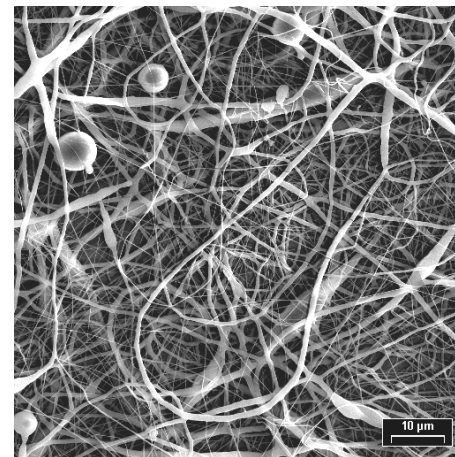
(c) 4 wt%



(d) 5 wt%

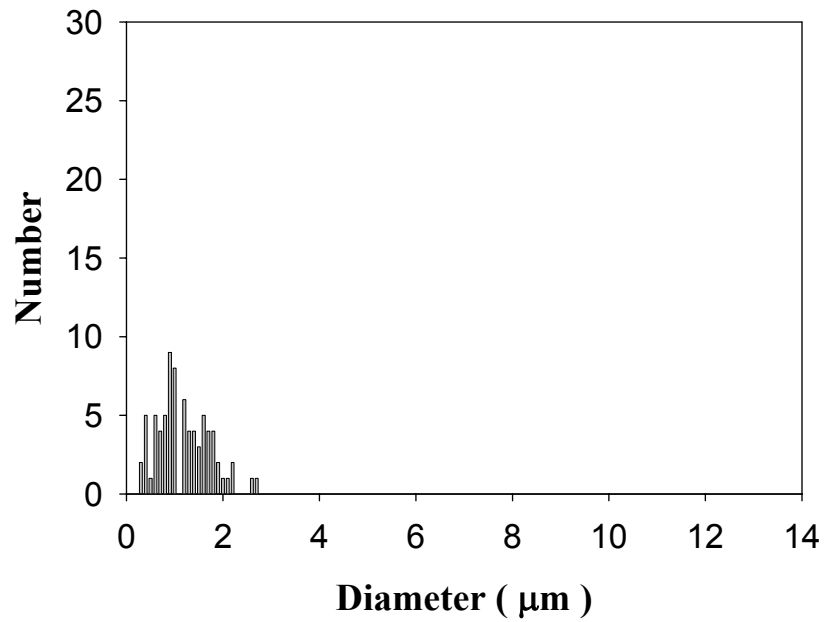


(e) 7 wt%

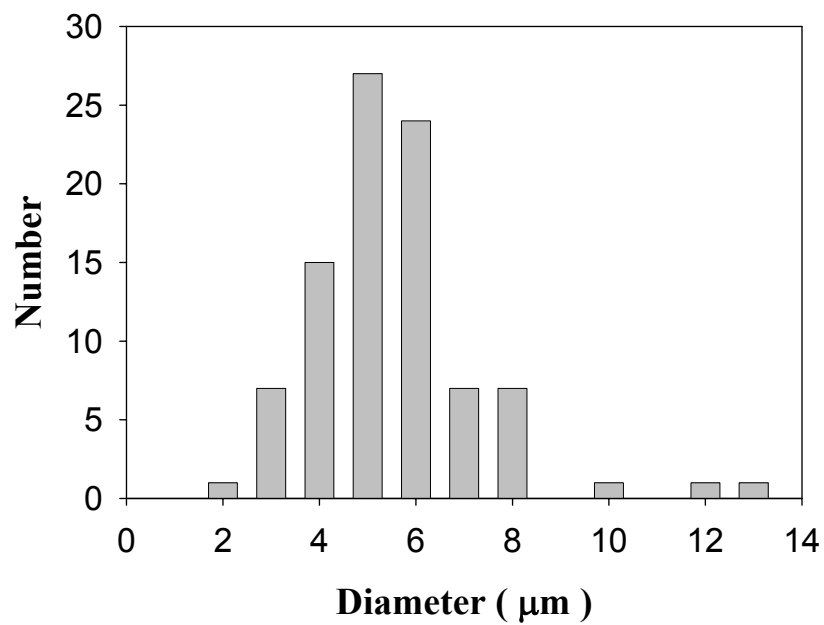


(f) 9 wt%

Fig. 52 Photographs showing the structure of electrospun PCL for various solution concentrations.



(a)



(b)

Fig. 53 Bead size distribution in the polymer obtained on the collector for solution concentration of (a) 1% (30 kV, 26 gauge needle) (b) 3% (30kV, 20 gauge needle).

Further evaporation of the solvent slows down because of diffusion barriers through this skin layer. When the organic solvent inside the bead finally escapes, the atmospheric pressure tends to collapse the particle. As a result, cavities are formed on the surface of the particle as shown in Fig. 54.

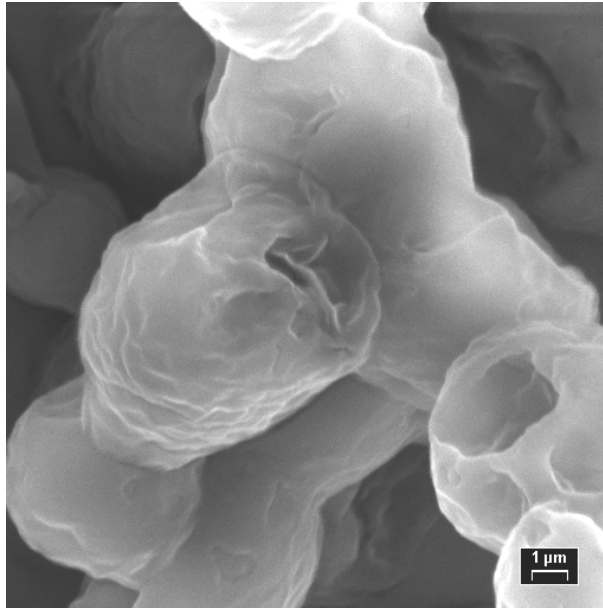


Fig. 54 Photograph showing cavities on the surface of the beads. Hollow beads can be produced by electrospinning.

These results indicate that sub-micron sized (solid or hollow) particles of PCL can be produced by electrospinning by controlling the solution concentration. The solution does not undergo significant extensional flow and hence, the beads are not likely to exhibit significant orientation between the molecules. Drugs and other biomolecules can be added to the solution to produce nano-sized particles that may be very useful in targeted drug delivery.

The transformation from beads to fibers begins at 4 wt% PCL in solution as can be seen from Fig. 52(c). In this case, small filaments between the droplets become

stabilized. Finally at 5 wt% PCL, a completely fibrous interconnected structure with a web of sub-micron fibers is observed. As indicated previously, this concentration may correspond to the rapid rise in viscosity as shown in Fig. 34. Note that the mass deposited on the collector drops considerably because of the increase in viscosity (Fig. 51). A similar fibrous interconnected structure is also obtained at 7 wt%. A small number of beads also start to appear in the structure to produce bead-on-string type of morphology. When the concentration is increased to 9 wt%, the fibrous structure is not uniform, with large amounts of thick fibers and beads. A spindle-like morphology was observed in most of the beads. The average diameters of the fibers and beads and the average distance between the beads increase as the viscosity of the solution increases. The distribution of the fibers is shown in Fig. 55. At concentrations greater than 5%, two distinct classes of fibers can be observed in the structure indicating a bimodal distribution. The mean diameter of the 1st group and the 2nd group is around 0.26 μm and 0.51 μm respectively. At 7 wt% PCL in solution, the corresponding diameters of the 2 groups are 0.17 μm and 0.59 μm . At 9 wt% PCL, the structure is more complicated with extensive amounts of beads and fibers, but again a bimodal distribution is observed. In this case, the mean diameters of the first group and second group are around 0.17 μm , and 0.85 μm respectively. It was not possible to electrospin at concentrations greater than 9% because the viscosity was so high that the solvent evaporated before the the formation of stable jet, thereby clogging the flow. Thus, there is an upper and lower limit for solution concentration during electrospinning.

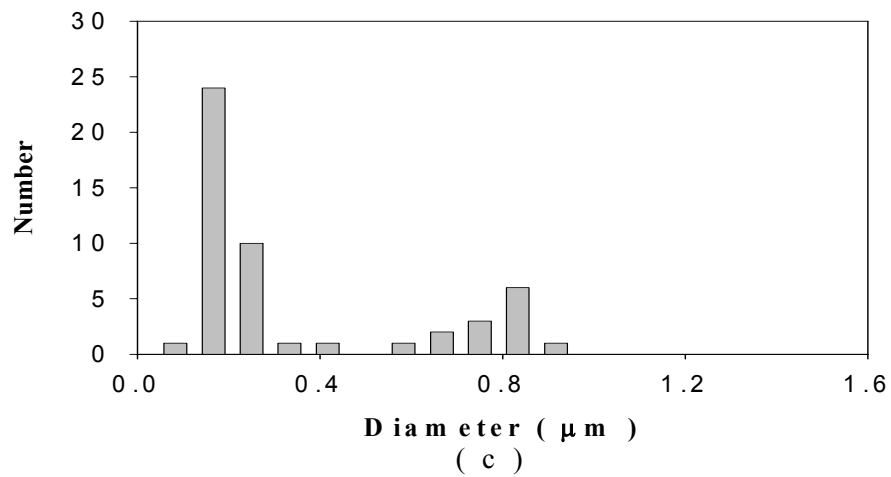
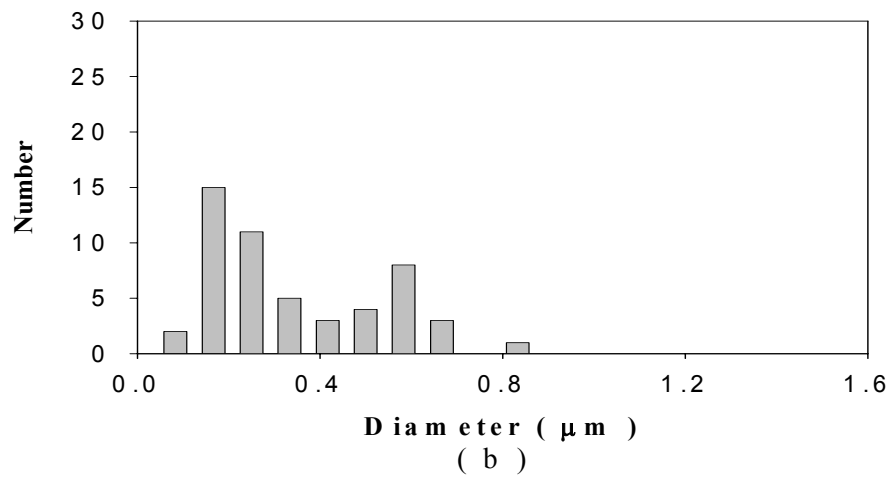
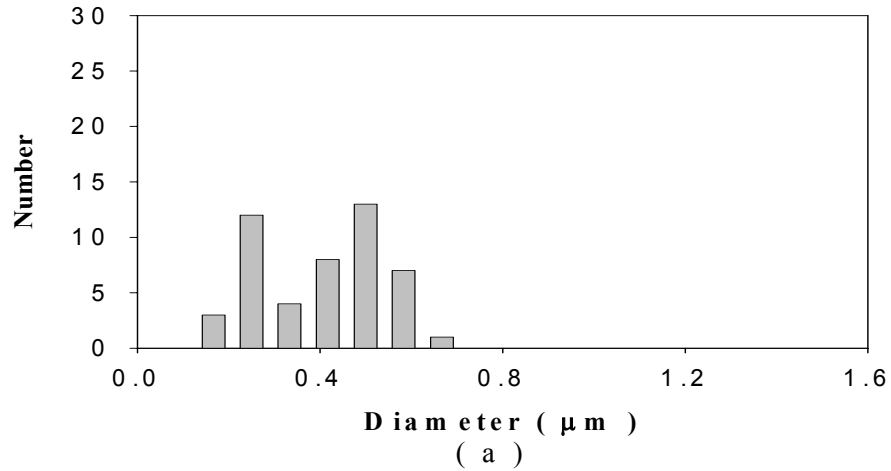


Fig. 55 Fiber diameter distribution in the polymer obtained on the collector for a solution concentration of (a) 5 wt% PCL (b) 7 wt% PCL (c) 9 wt% PCL (30 kV, 20 gauge needle).

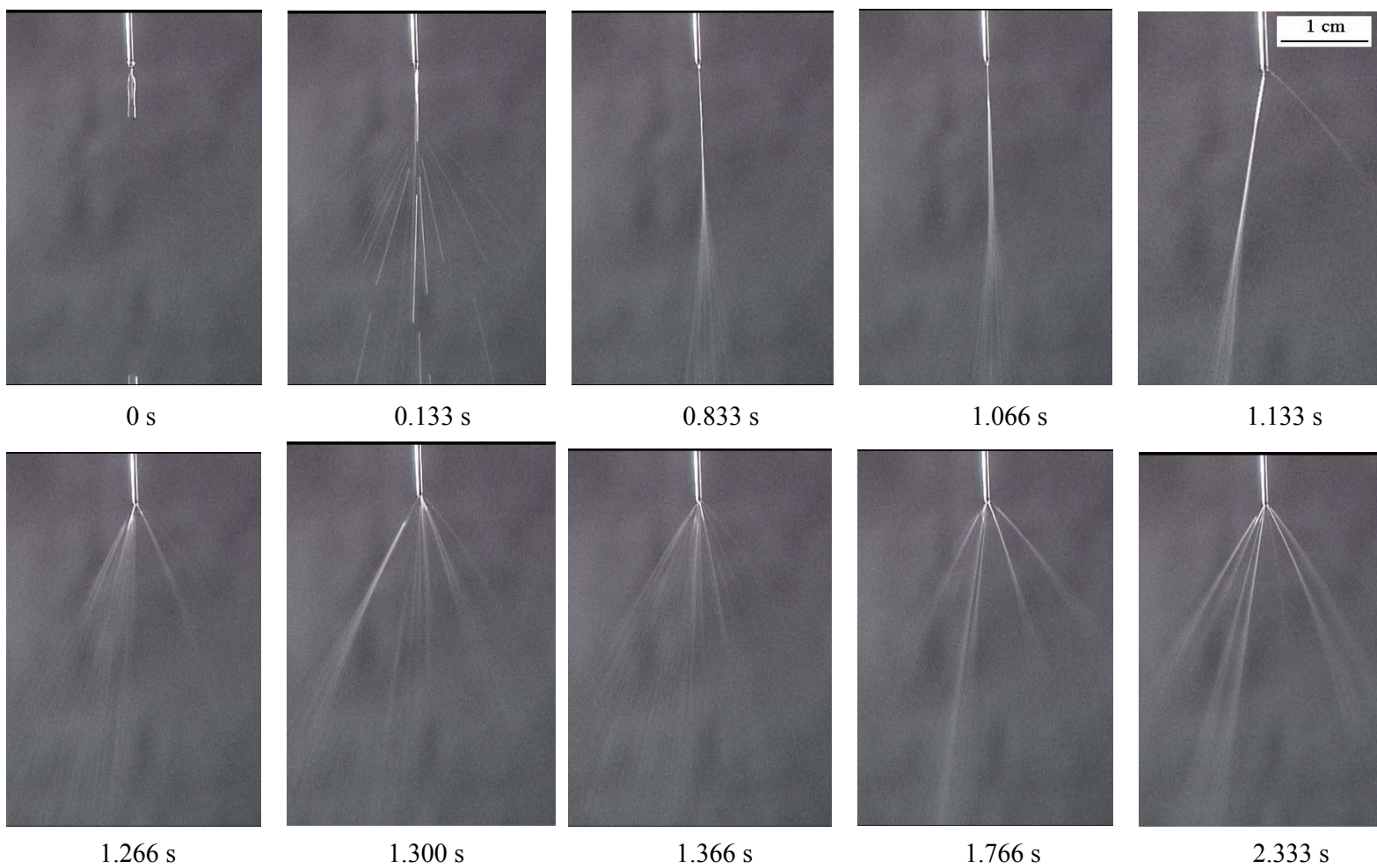


Fig. 56 Sequential images showing the breakdown and splaying of the jet during electrospaying. (3wt% PCL, 30 kV)

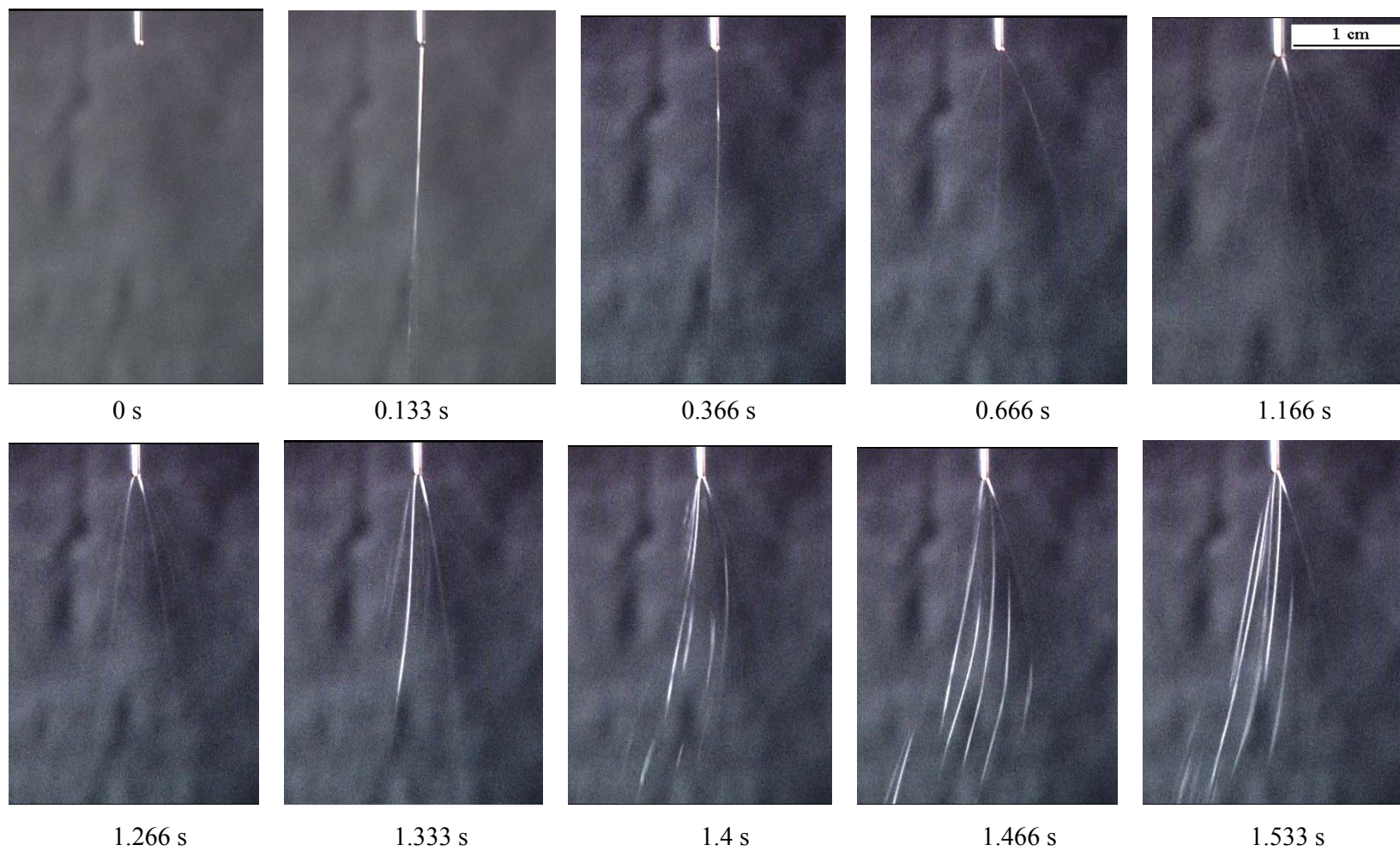


Fig. 57 Sequential images showing the breakdown and splaying of the jet during electrospinning. (9 wt% PCL, 30 kV)

Sequential stages during the breakdown of the jet are shown in Fig. 56 and 57 for 2 different concentrations. An analysis of the digital images leads to the following observations listed sequentially for 3 wt% (electrospraying) and 9 wt% (electrospinning).

(a) 3% PCL (*electrospraying*):

1. Initial dripping of the solution from the needle
2. Cone-jet generates and primary splaying (major jet) occurs at the end of the jet.
3. Cone-jet becomes thinner with an increase of voltage and tilts gradually to the left (*i.e.* bending instability).
4. Cone-jet splits into two jets at the end of the needle.
5. Cone-jet splits into multitude of major-jets at the end of the needle (primary splaying of major-jets), and each jet further splits into many (secondary splaying) mini-jets.
6. Each major jet may change the direction at different times.
7. Each mini-jet gradually disintegrates into small droplets with an increase of time.

(b) 9% PCL (*electrospinning*):

1. Initial light dripping of the solution from the needle.
2. Cone-jet generates and primary splaying (major jet) occurs at the end of the jet.
3. Cone-jet becomes thinner and tilts gradually to the left (*i.e.* bending instability).
4. Cone-jet splits into three jets at the end of the needle.
5. Cone-jet splits into multitude of jets (primary splaying of major jets) and spinning jet occurs.
6. Multi-spinning jets generate at the end of the needle and continuous movements of the jets can be observed through the different frames.
7. Each spinning jet splits into many (secondary splaying) mini-jets, with each mini-jet gradually evaporating and solidifying with an increasing time.

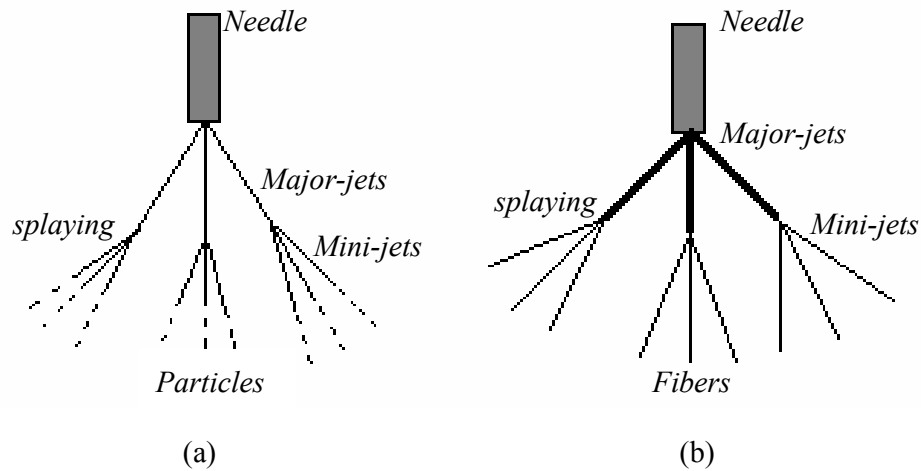


Fig.58 Schematic illustration of the breakdown of the jet at 3 wt% PCL (a) and 9 wt% PCL (b). These conditions correspond to the breakdown of the jet in electro spraying (a) and electro spinning (b).

These results are schematically illustrated in Fig. 58 to highlight the differences between electro spraying that occurs at low concentrations and electro spinning that occurs at high concentrations. The instabilities shown in Figs. 56 and 57 indicate that varicose instability dominates the morphology in low viscosity solutions, highlighting the formation of a large number of beads. On the other hand, high solution viscosity opposes varicose instability and favors bending instability. In electro spraying of extremely diluted solutions, the collapse of the liquid jets into droplets leads to the formation of particles between 0.9 μm to 5 μm . In this low viscosity condition, the electrically forced jets oppose the development of stable fibers and favor the formation of beads (or particles). Electro spinning conditions are attained between 5 wt% to 9 wt% and various morphologies in the polymer can be obtained depending on the collection procedure. In this investigation, the stationary mesh yields a web of highly porous interconnected sub-micron fibers. During electro spinning, the coiled macromolecules of the base polymer are transformed through elongational flow of the jet into oriented, entangled networks that persist as

the fiber solidifies [20]. Under conditions of elongational flow, the highly oriented jet may splay into many smooth fibers as in Fig. 52(c).

It can be seen from Fig.51, that from 5 wt% to 9 wt%, the mean of the small diameter group of fibers does not change much, but the mean of the larger group shifts to the right. This result indicates that the 2nd group (with a higher mean diameter) of fibers becomes thicker with increasing concentration. In addition, the fraction of fibers in the larger group decreases with an increase in concentration. These results suggest that a high solution viscosity may favor the formation of thick fibers. A plausible explanation for this behavior is given below. Two competing physical phenomena may govern structure formation during electrospinning: electrical repulsion force and viscoelastic force. The repulsion force will make the jet thinner and finally split below the needle (*i.e.* splaying). Inter and intra molecular entanglements may increase at high viscosity. The entangled network may increase, viscoelastic properties significantly that it makes it difficult for the fibers to split, thereby producing thick fibers.

As the solution concentration is increased from 3 wt% to 9 wt%, it can be observed that the microstructure transforms from beads (or particles), to fibrous matrices, to an interconnected membrane structure with a web of fibers. The beads become larger from 5 μm to 8 μm and the average distance between the beads increases. The shape of the beads change from sphere to something like a spindle as the viscosity is increased. Image analysis data showed that the average pore size between the fibers was around 3.5 μm to 4.5 μm .

5.5 Effect of Voltage

The applied voltage determines the strength of the electrical field experienced in the solution and hence has a significant effect on the breakdown of the jet. Increasing voltages generally lead to an increase in the jet current. The jet current is proportional to the transport of electrons and thus establishes the extent of mass flow from the tip of the needle to the collector [41]. Hence the mass of PCL obtained on the collector increases with applied voltage as shown in Fig.59. The deposition area also increases with voltage and was estimated to be on the order of 2 cm² and 3 cm² at voltages 25 kV to 40 kV respectively.

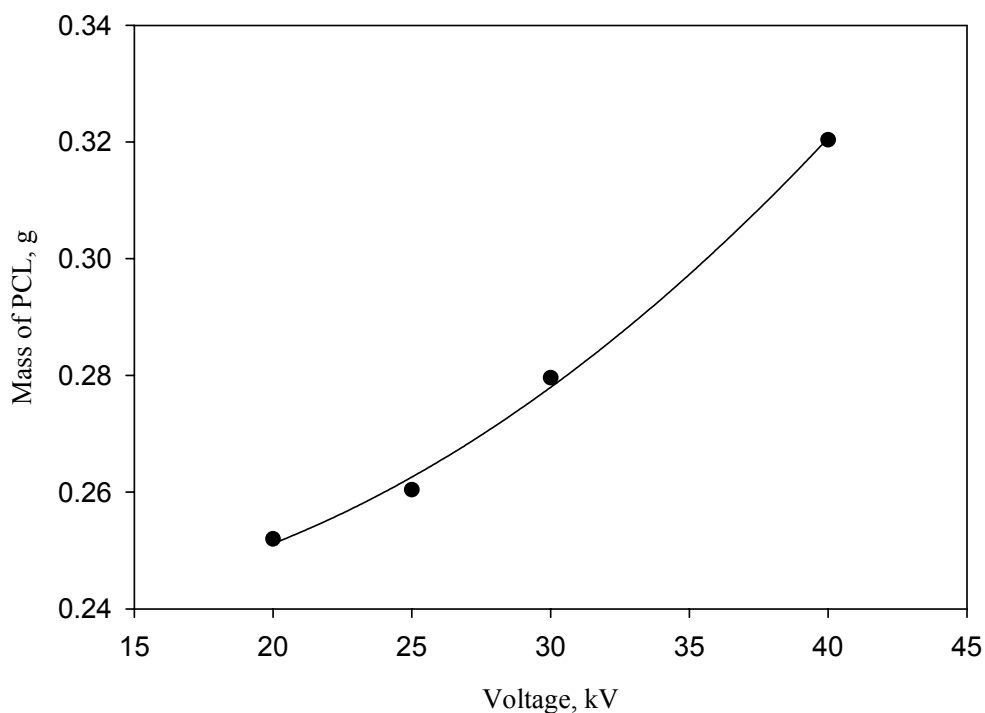


Fig. 59 Mass of PCL deposited on the collector in a time of 2 min for various voltages (Solution concentration = 5 wt%).

The effect of voltage on the structure in the electrospun polymer is shown in Fig. 60. At low voltage (20 kV), the structure consists mostly of spherical beads with small

filaments between the beads indicating that the bending instability is beginning to stabilize the jet. As the voltage is increased to 25 kV, a completely fibrous structure is obtained. A similar structure is also obtained at 30 kV. At 40 kV, the flow rate is so high that the fibers are packed together more densely as shown in Fig. 60 (d). The distribution of the fiber diameters in the sample is show in Fig. 61. A bimodal distribution is again observed in the fiber diameter. The diameter of the mean diameter of the first group is around $0.26\ \mu\text{m}$ for all the voltages. The mean diameter

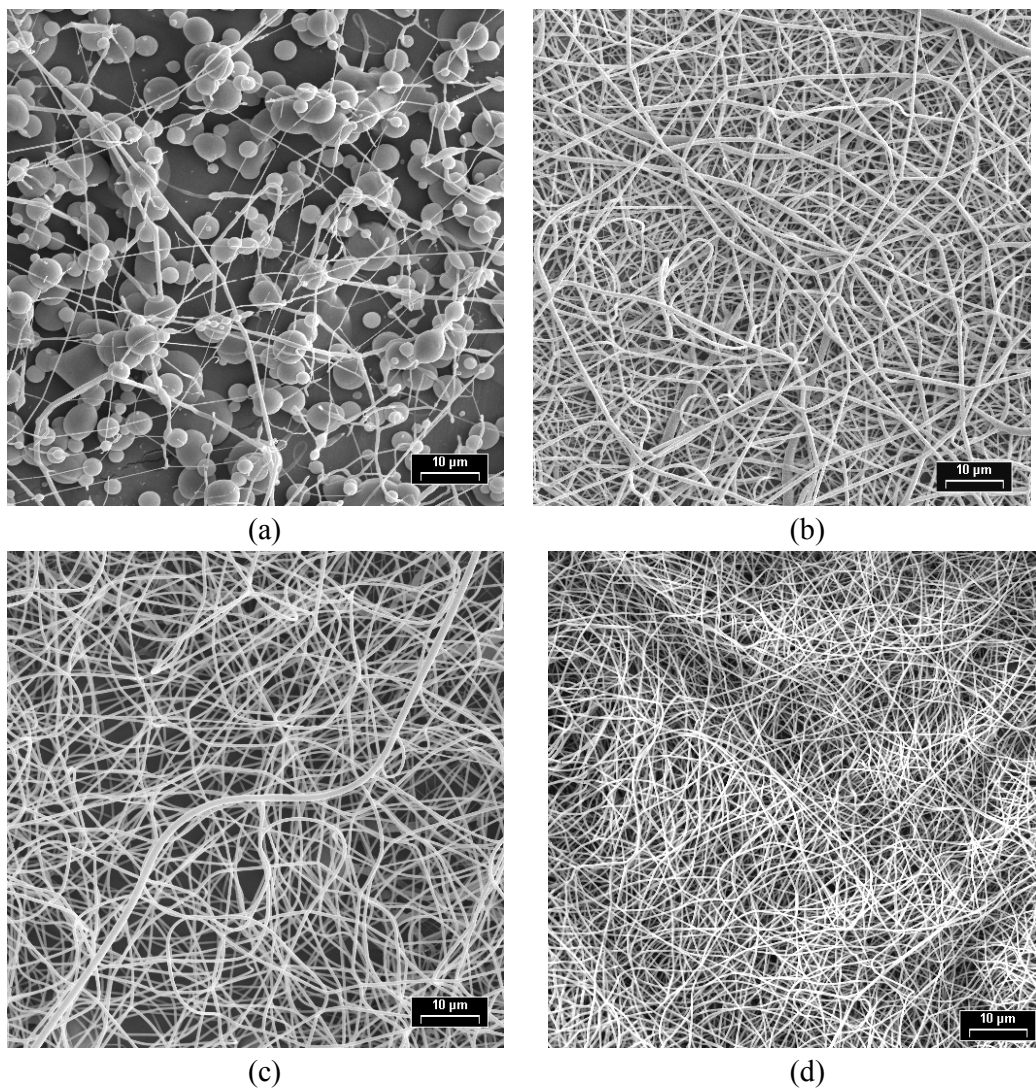
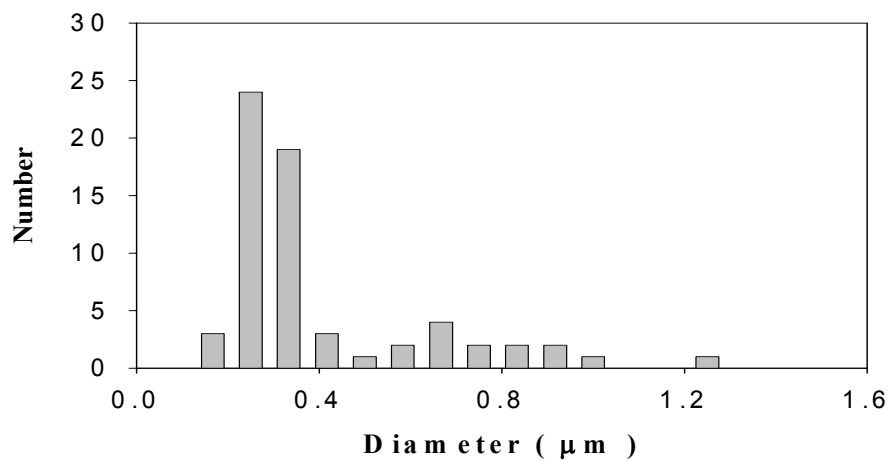
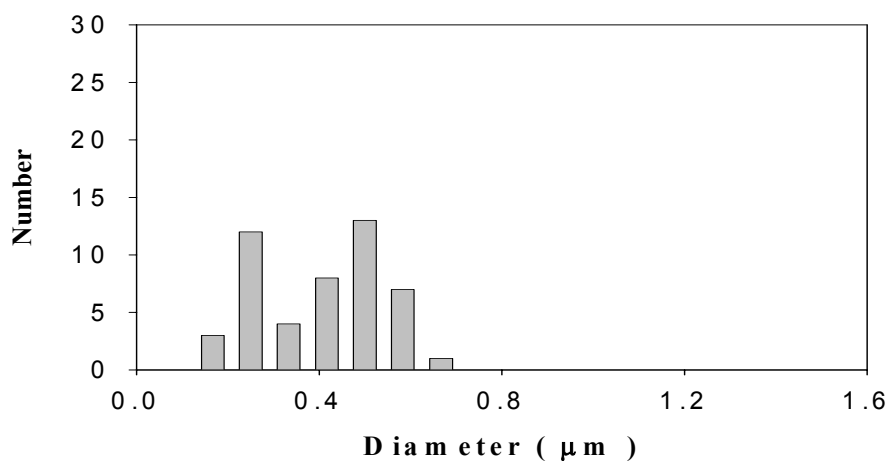


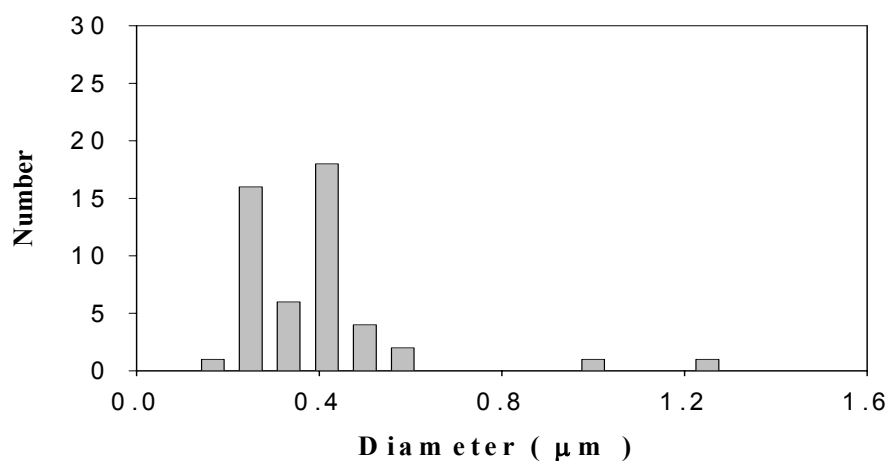
Fig. 60 Photographs showing the effect of applied voltage on the structure in the electrospun polymer (solution concentration 5 wt%, deposition distance = 75 mm). (a) 20 kV (b) 25 kV (c) 30 kV (d) 40 kV



(a)



(b)



(c)

Fig. 61 Fiber diameter distribution in the polymer obtained on the collector for a voltage of (a) 25 kV (b) 30 kV (c) 40 kV (concentration = 5 wt% PCL).

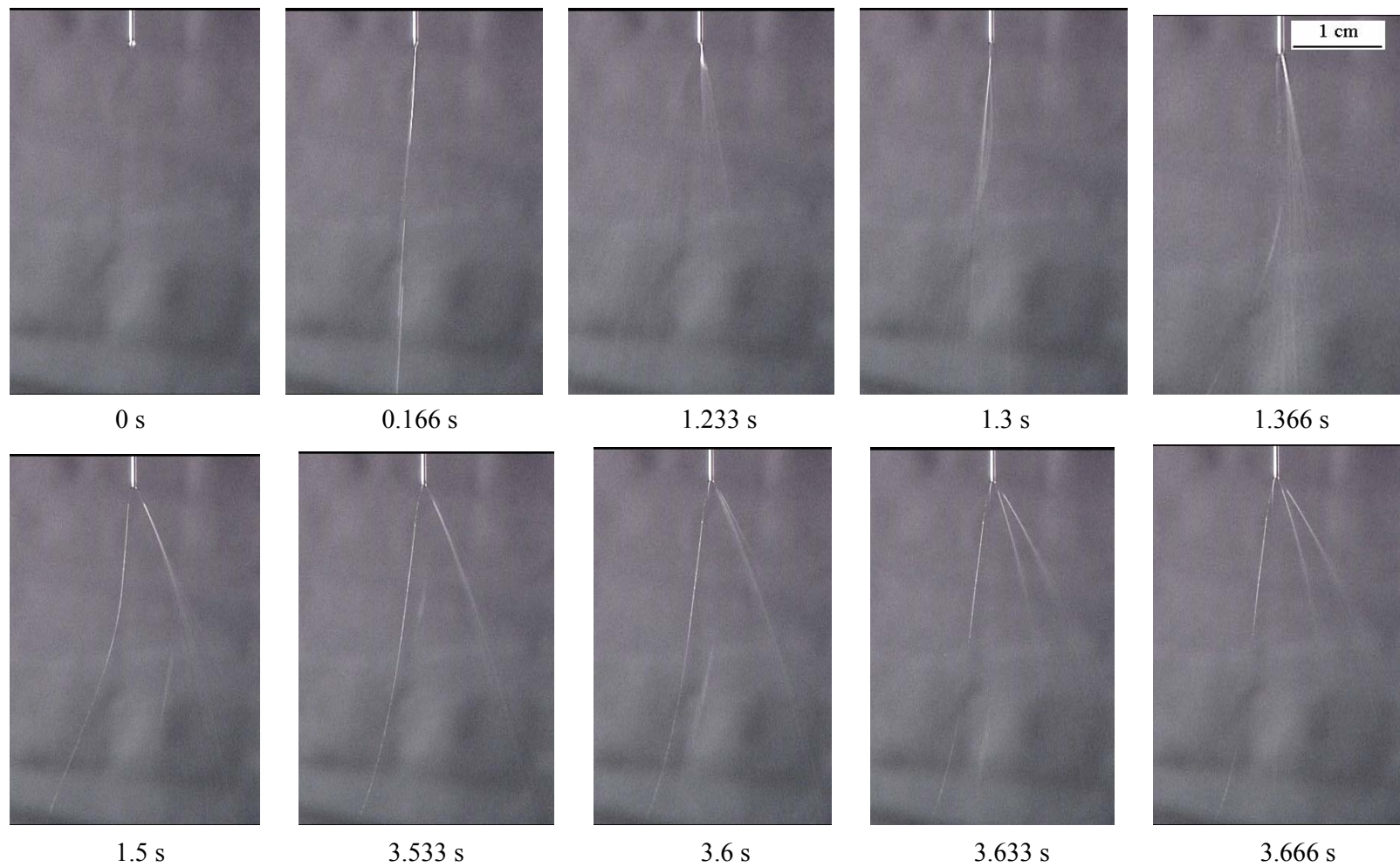


Fig. 62 Sequential images showing the breakdown and splaying of the jet during electrospinning. (5wt% PCL, 20 kV)

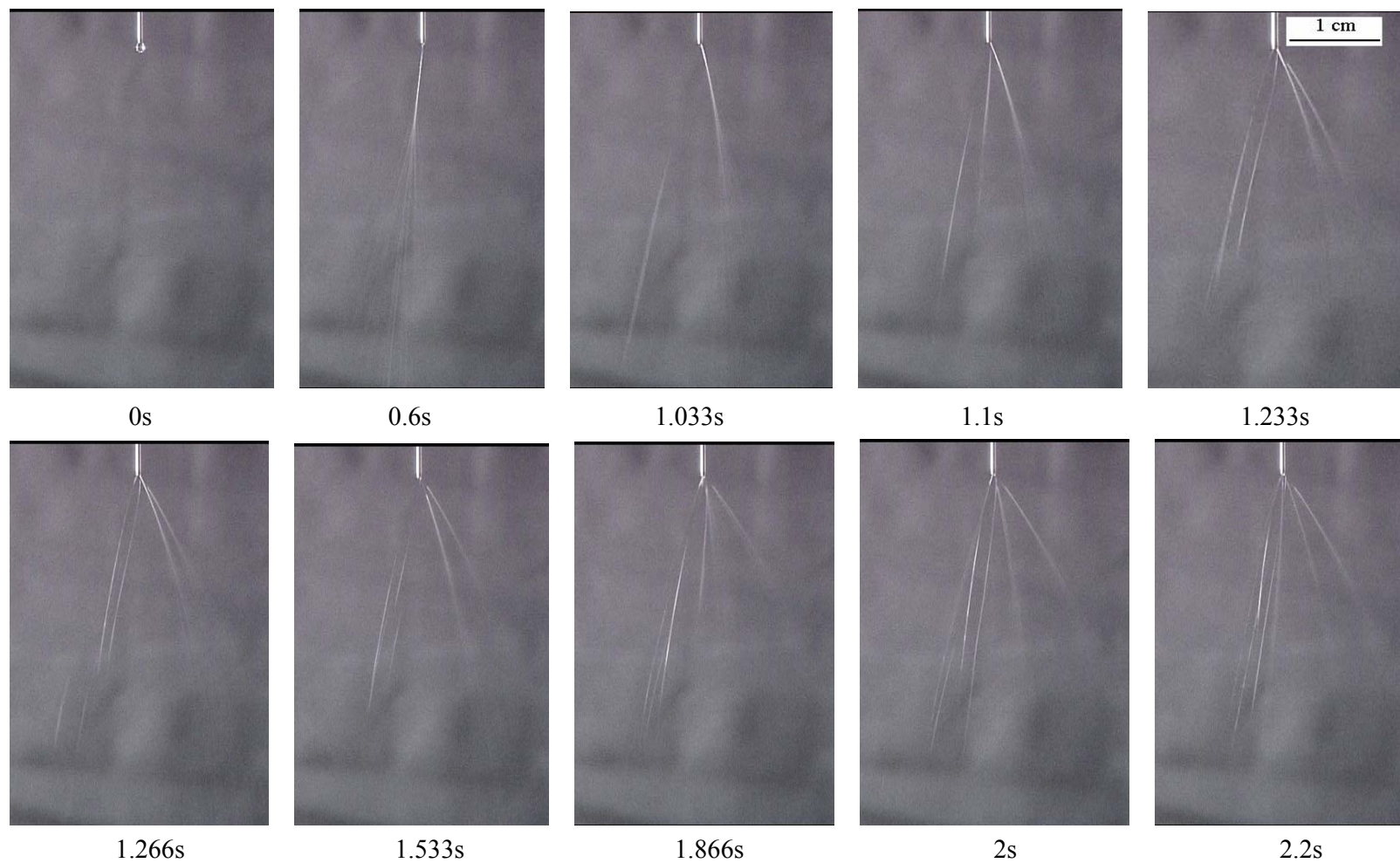


Fig. 63 Sequential images showing the breakdown and splaying of the jet during electrospinning. (5wt% PCL, 40 kV)

of the 2nd group in the distribution shifts to the right with decreasing voltage (0.43 μm at 40 kV, 0.51 μm at 30 kV and 0.67 μm at 25 kV). Sequential images of the jet during electrospinning at 2 different voltages are shown in Figs. 62 and 63. The principal observations from these photographs are given below:

Electrospinning 5 wt% solution at 20 kV (Fig. 62)

1. Dripping.
2. Cone-jet forms and primary splaying (major jet) occurs at the end of the jet.
3. Cone-jet becomes thinner and tilts gradually to the left.
4. Cone-jet splits into two jets at the end of the needle.
5. Cone-jet splits into three to four jets (primary splaying—major jet) and spinning jet occurs.
6. Three to four spinning jets are generated at the end of the needle and continuous movements of the jets can be observed in the different frames.
7. Each spinning jet splits into many (secondary splaying—mini-jets), with each mini-jet gradually solidifying on the collector after solvent evaporation.

Electrospinning 5 wt% solution at 40 kV (Fig. 63)

1. Dripping.
2. Cone-jet forms and primary splaying (major jet) occurs at the end of the jet.
3. Cone-jet becomes thinner and tilts gradually to the left.
4. Cone-jet splits into two jets at the end of the needle.
5. Cone-jet splits into 3-4 jets (primary splaying—major jet) and spinning jet occurs.
6. Six to eight spinning jets are generated at the end of the needle and continuous movements of the jets can be observed in the different frames.
7. Each spinning jet splits into many mini-jets, with each mini-jet gradually solidifying on the collector after solvent evaporation.

It was observed that when the applied voltage is removed, the solution reverts back to initial state of dripping over a period of time. This incubation time between the elimination of the electrical field and the start of dripping increased with increasing voltage. As the voltage is increased, the structure changes from primarily beads to predominantly fibers. The change in structure results from the increased splaying

that occurs from the beads at high voltages. For example, compare the splaying in Fig. 64 at 20 kV (a) and 40 kV (b). The higher charge density and stronger charge repulsion at high voltages enhance bending instability at the expense of varicose instability [30]. In addition, the resulting mini jet may splay repeatedly and to reduce the overall fiber diameter significantly at high voltages (Fig. 64). Note in Figs. 62 and 63 that there are generally only about 3 to 4 jets emerge from the needle tip at 20 kV, while at 40 kV, 7 to 8 jets may be observed. This splaying may result from the high repulsive force established at high voltages. Hence, an increase in voltage not only favors the formation of fibers, but also promotes the development of thin fibers. Note also that the size of the beads that may form in the structure decreases with voltage as shown in Fig. 65.

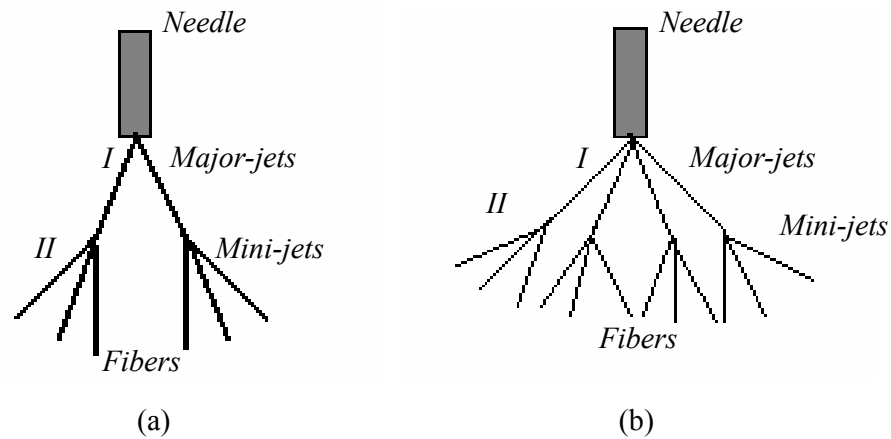


Fig. 64 Schematic illustration of the breakdown of the jet at an applied voltage of 25 kV and (b) 40 kV. Regions of primary splaying (I) and secondary splaying (II) are indicated.

The change in fiber morphology with voltage may also be correlated to changes in the shape of the initial droplet forming at the needle tip [14]. At low voltages, a droplet of solution remains suspended at the end of the syringe needle, and the fiber jet emerges from a cone at the bottom of the droplet. The cone has a semi-vertical angle of 49.3° as predicted by Taylor. In this case, the jet originates from the bottom of a

drop whose diameter is larger than the capillary diameter. The nanofibers produced under these conditions generally have a cylindrical morphology with few beads present. As voltage is increased, the volume of the droplet decreases, the cone may recede and the jet may originate from the liquid surface within the syringe tip. The

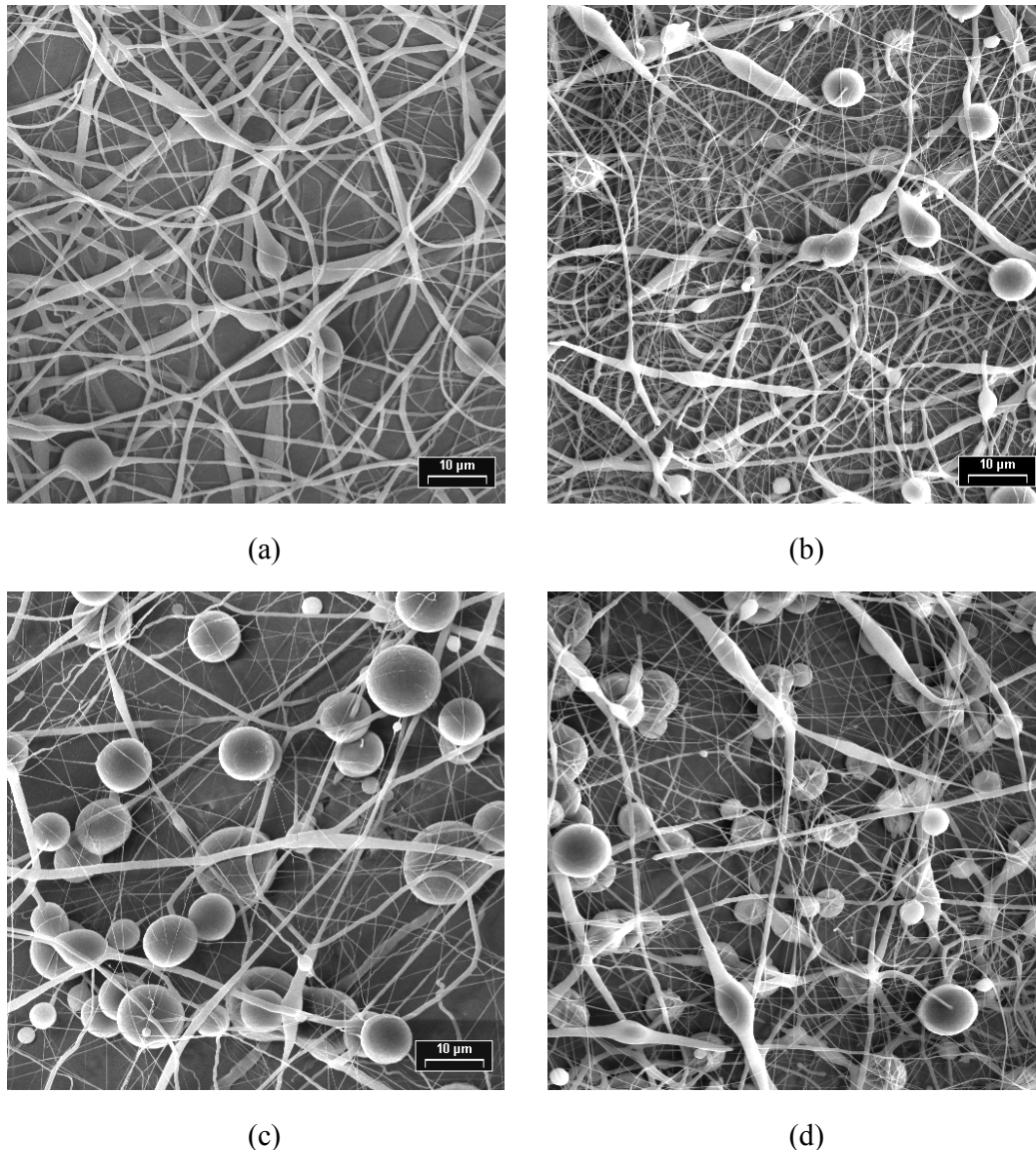


Fig. 65 Photographs showing the structure in the electrospun polymer obtained from a 9 wt% PCL solution. (a) 10 kV, Position X, Center (b) 30 kV, Position X, Center (c) 10 kV, Position Y, Periphery (d) 30 kV, Position Y, Periphery. The positions correspond to the sample locations shown in Fig. 44.

fibers still have a cylindrical shape, but more beads may form. At sufficiently high voltages, the solution jet may initiate directly from the needle tip with no externally visible droplet or cone. At this voltage, the jet may originate on the inside surface of the needle, where the edge of the liquid surface meets the needle wall. The fibers produced under these conditions may have a high density of bead defects.

5.6 Effect of Deposition Distance

The distance between the needle and the collector has a significant influence on the structure. Large deposition distances enable complete solvent evaporation before collection and so produce dry fibers or round spherical particles. By contrast, short deposition distances yield wet fibers or powders. Wet coating elements promote intra- and inter-layer bonding. The residual solvent may lead solvent bonding and produce a more dense structure. If the deposition distance is increased to large values, however, the field strength per unit length decreases. Large deposition distances can lead to round fibers and beads (Fig. 35(a)), while small distances typically produce irregular powders or flat fibers (Fig. 35(b)).

Typical structures obtained with 9 wt% sample at various deposition distances are shown in Fig. 66. The corresponding fiber distributions are shown in Fig. 67. At a distance of 7.5 cm, the interconnected membrane type web structure can be observed throughout the specimen. A bimodal distribution is observed again as can be seen from Fig. 67(a). The mean diameter of the 1st group of fibers is still around 0.17 μm , and for the 2nd group it is 0.85 μm . When the deposition distance is increased to 12.5 cm, the morphology of the electrospun fibers changes dramatically. The fibers exhibit a three dimensional architecture compared with flat structure at 7.5 cm. The

bigger round beads cover the entire sample. The sample produced at a distance of 7.5 cm is more compact than the sample obtained at a distance of 12.5 cm. The bimodal distribution is still present in this sample. The mean diameter of the 1st group is still around 0.17 μm , while the mean diameter for the 2nd group decreases to about 0.52 μm .

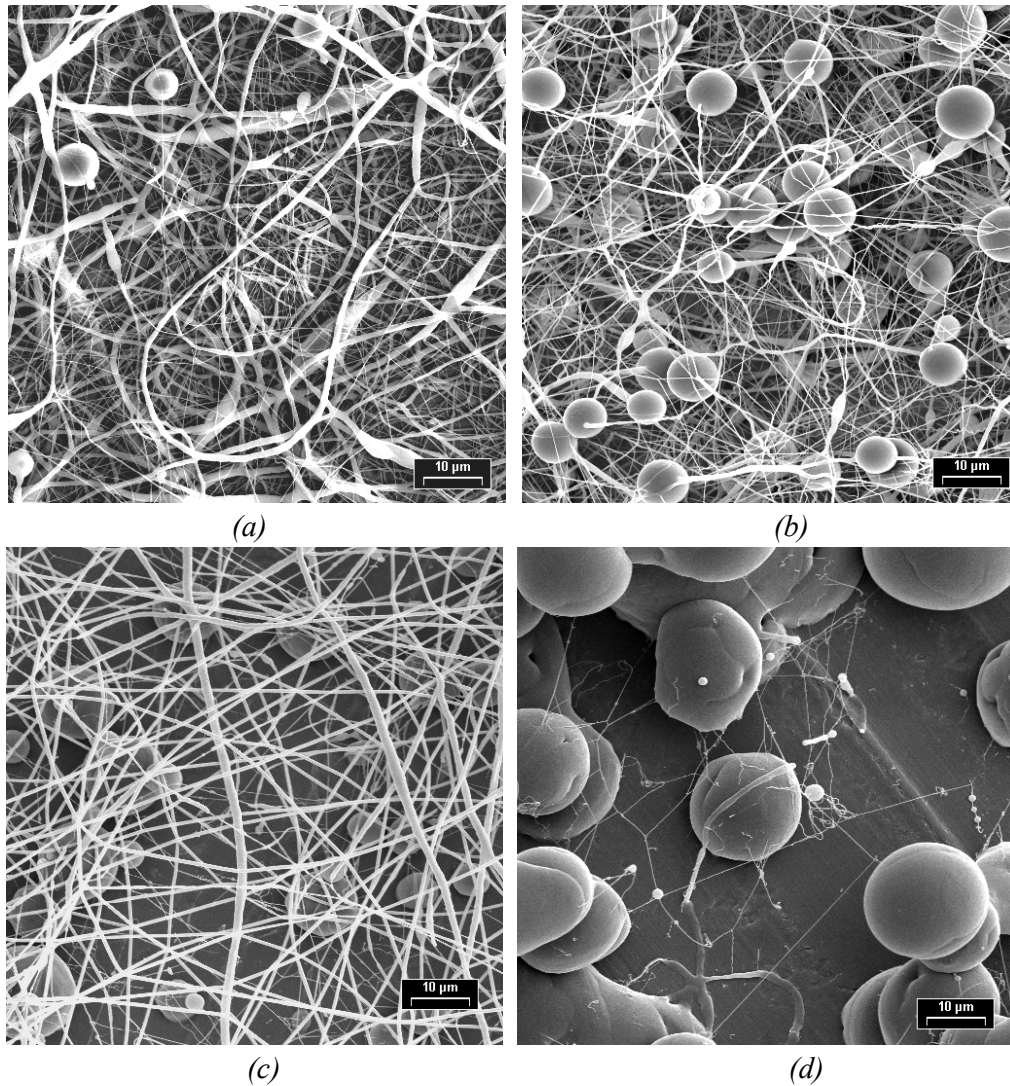
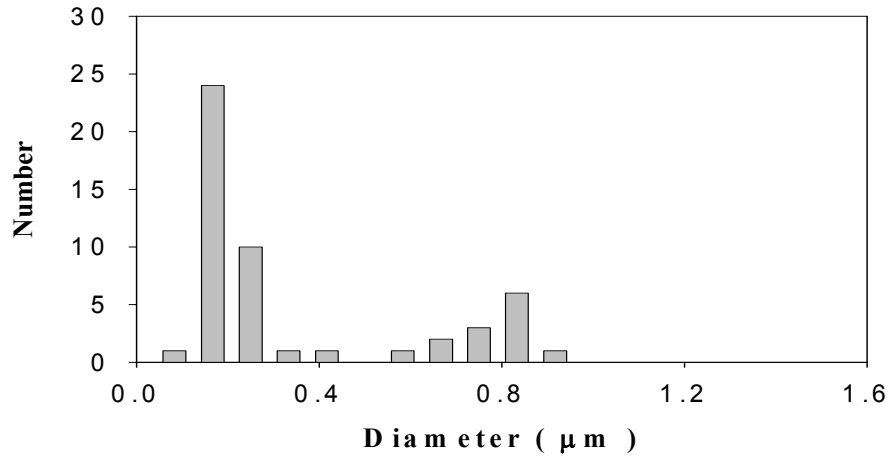
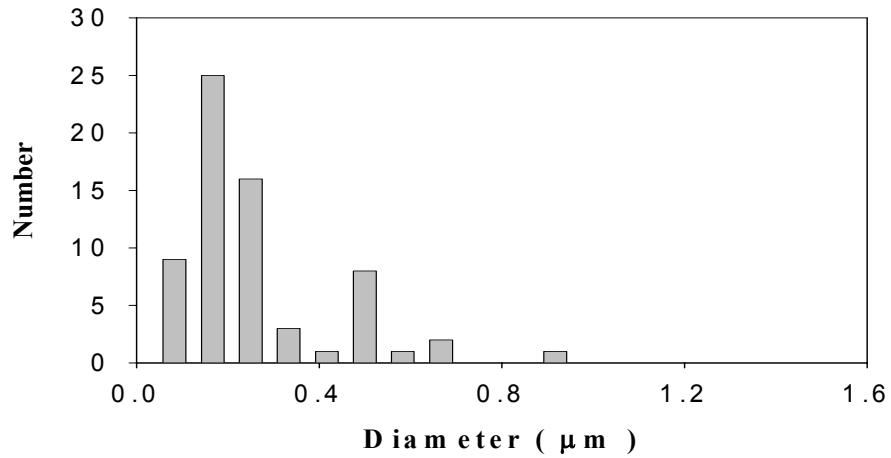


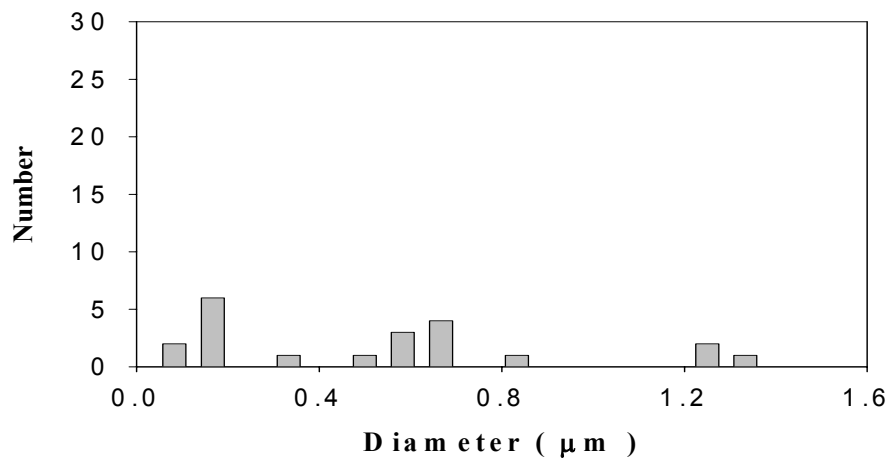
Fig. 66 Photographs showing the structure in the electrospun polymer for various deposition distances (a) 7.5 cm (b) 12.5 cm (c) 15 cm (d) 17.5 cm (Solution concentration 9 wt%, $V = 30$ kV).



(a)



(b)



(c)

Fig. 67 Fiber diameter distribution in electrospun PCL for various deposition distances (a) 7.5cm (b) 12.5 cm, (c) 15 cm (9 wt% PCL, $V=30$ kV)

By increasing the deposition distance to 15 cm, the morphology is different compared to that for a deposition distance 12.5 cm. Under this condition, the structure isn't as compact as the structure in Fig. 66(b). It was also observed that the deposition area increases significantly under this condition. This increase in area could also account for the change in morphology. In this case, a tri-modal distribution of fibers is obtained as shown in Fig. 67 (c). The three different distributions of fibers appear to be present in equal proportions compared to the previous samples where the 1st group (in the bimodal distribution) dominates the mass fraction. The morphology at a deposition distance of 17.5 cm consists primarily of large beads. The fibers present here are fragments of electrospun fibers.

5.7 Effect of DMF

The properties of the solution have a significant effect on the structure of the electrospun polymer. The viscosity, surface tension, electrical conductivity and dielectric constant of the solution play an important role in controlling the structure [20]. These parameters are governed by the properties of the base polymer and of the solvent. The use of additives to control the properties of the solution and thereby control the architecture in the polymer has been studied previously [20,40]. The additives are used to control the properties listed above. One additive that has been used previously is *N,N*-dimethylformamide (DMF) [40]. The effect of chloroform/DMF ratio is shown in Fig. 68. At Chloroform/ DMF volume ratio = 6:1, mostly wet fibers were produced. The wet fibers dissolved and bonded together and only few fibers were obtained observed after solidifying (Fig. 68(d)). Note that with pure chloroform, a completely fibrous structure is produced (Fig. 68(a)). DMF

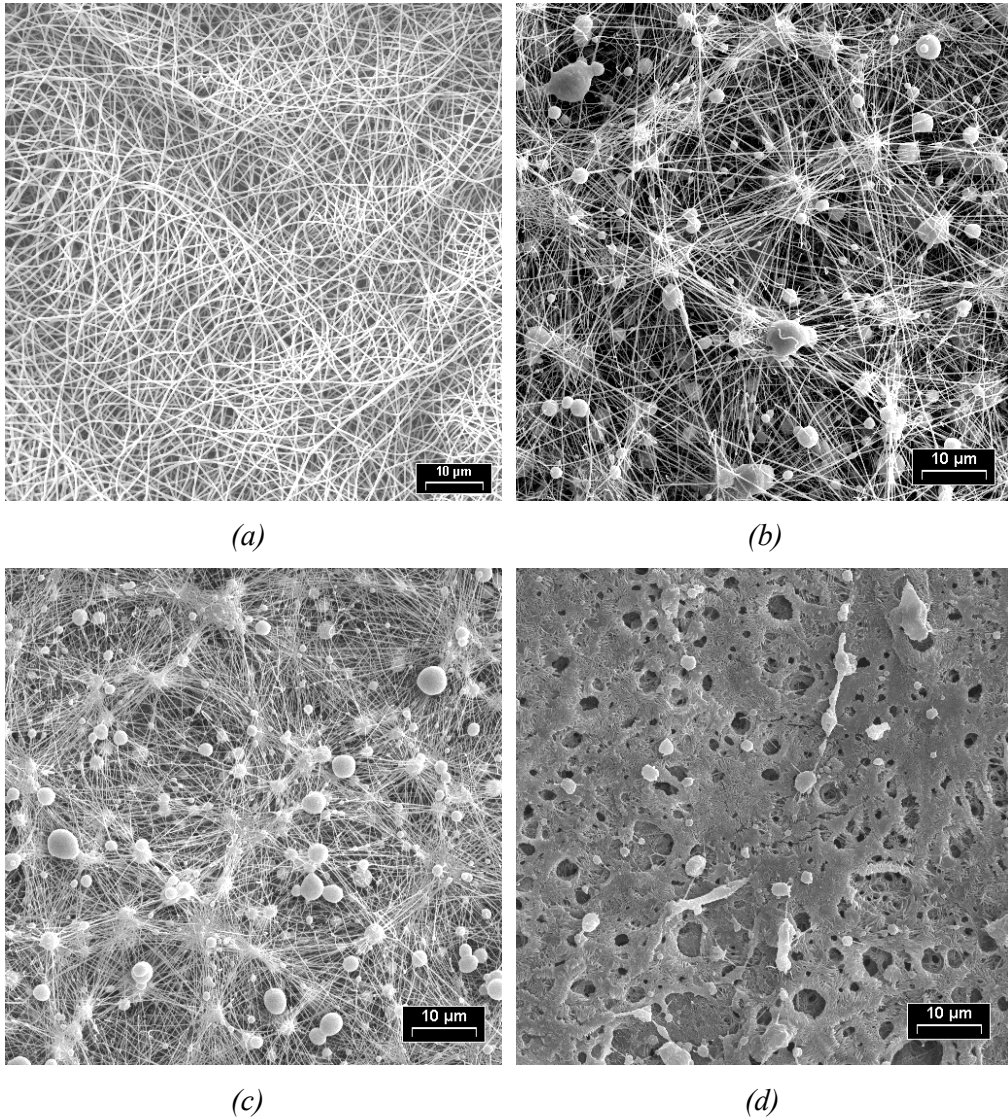
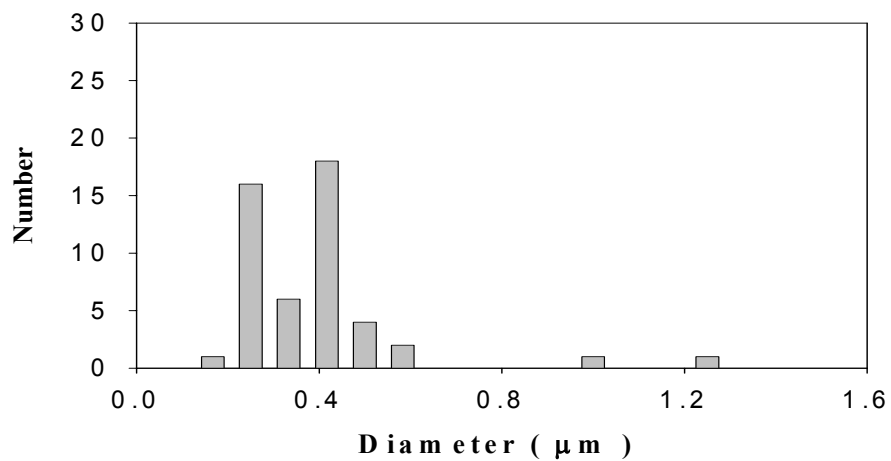
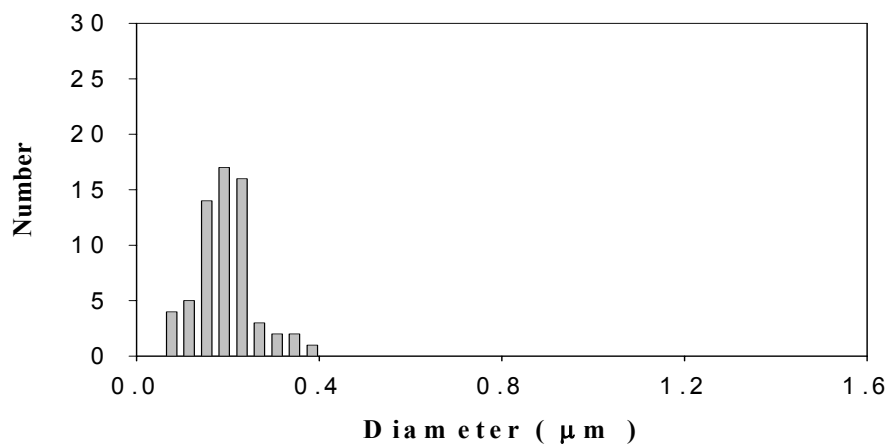


Fig. 68 Effect of chloroform/DMF ratio(v/v) on structure of electrospun PCL. (a) Pure chloroform at 7.5cm (b) 12: 1 at 10cm (c) 9: 1 at 10cm (d) 6:1 at 7.5cm deposition distance (5 wt%, 40 kV, 20 gage needle).

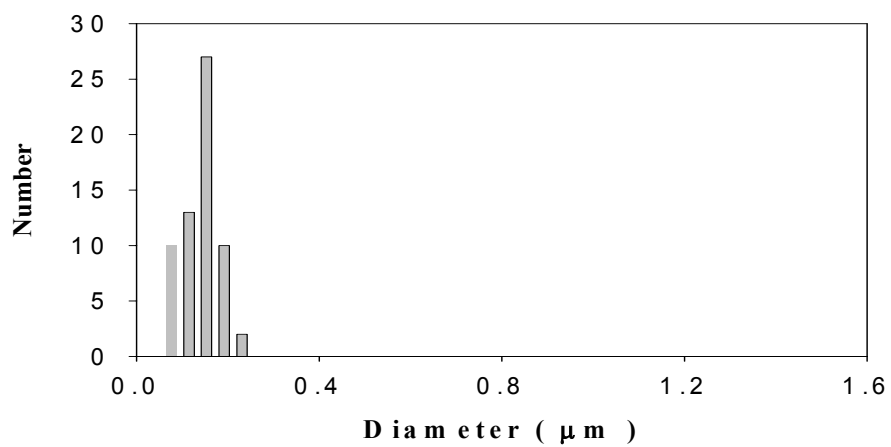
has a boiling point of 153°C and is not a solvent for PCL. As a result, the rate of evaporation of liquids (solvent+DMF) from the jet decreases upon the addition of DMF. In order to increase the solvent evaporation rate, the amount of DMF was reduced and the deposition distance was increased. At chloroform/ DMF volume ratio = 12: 1, the deposition distance 10 cm, a well-interconnected microstructure of bead-fibers is generated (Fig. 68(b)). The numerous ultra-thin fibers splaying from



(a)



(b)



(c)

Fig. 69 Fiber diameter distribution for various chloroform/DMF ratios (v/v) (a) Pure chloroform (b) 12:1 (c) 9:1

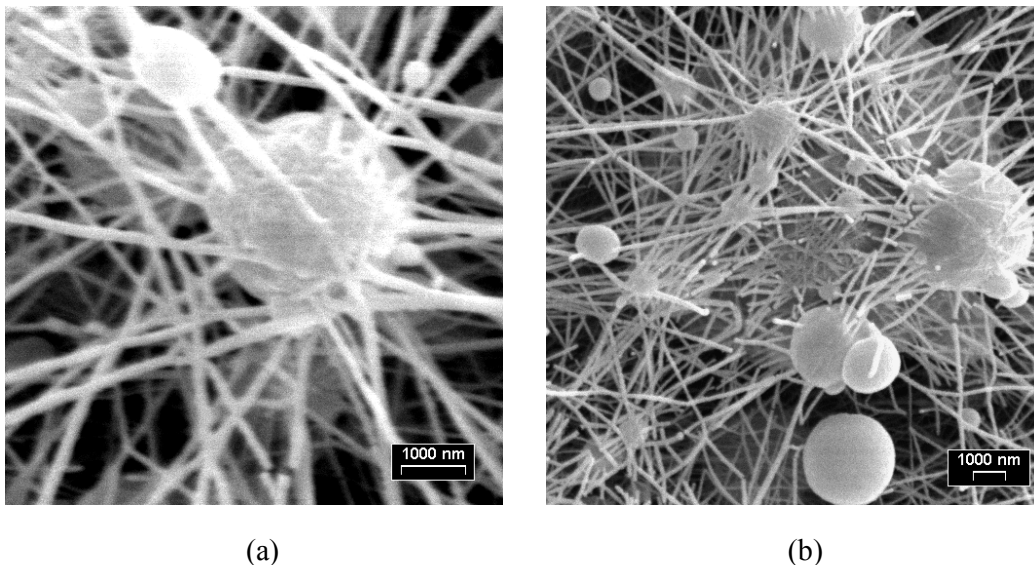
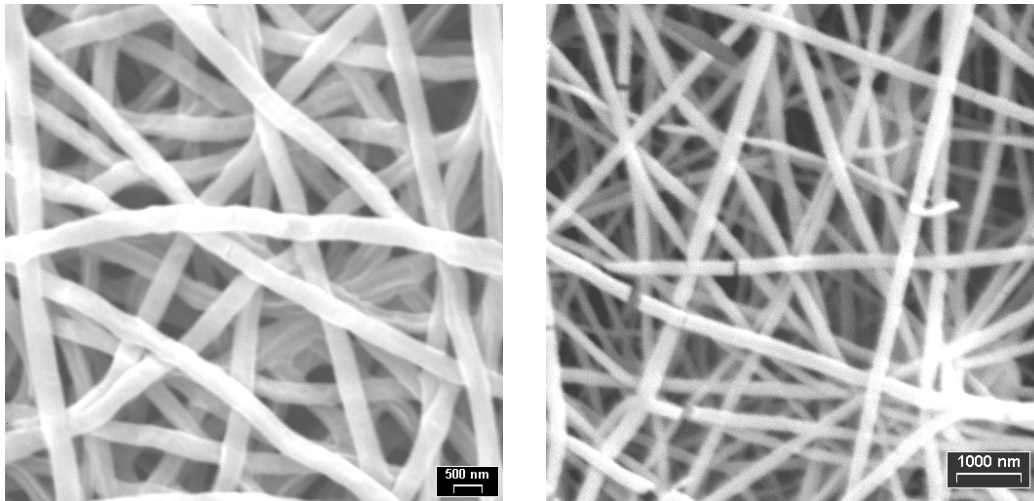


Fig. 70 Photographs showing (a) extensive splaying from a single bead and (b) fibers connecting different beads in samples with chloroform/DMF ratio of 9:1. (40 kV, 5 wt%, 20 gage needle, deposition distance = 10 cm)

the bead can be seen in Fig. 70(a). Further, the space between two beads has numerous connecting fibers (Fig. 70(b)). A unimodal distribution of ultrathin fibers is observed in this case, compared to the bimodal distribution of fibers without DMF (Fig. 69). The mean diameter of the fibers is around 200 nm. The smallest interconnected fibers are produced at chloroform/ DMF volume ratio = 9: 1 (Fig. 68(c)) The mean diameter of fibers decreases to about 150 nm.

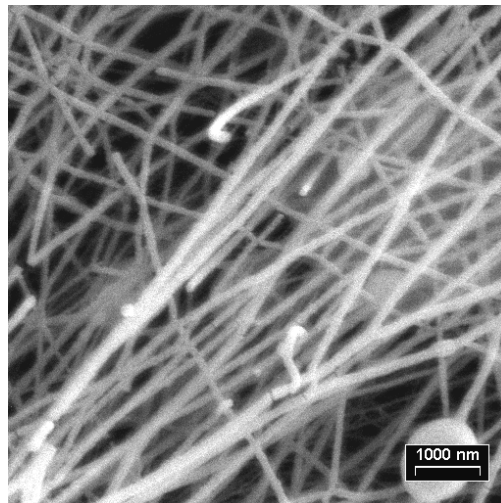
The addition of DMF may improve the conductivity and dielectric strength and lower the surface tension of the solution [40]. As a result, the jet may split and splay repeatedly to produce ultra-thin fibers. The deposition rate and area increase dramatically as the jet can form, splay and accelerate more easily towards the collector upon the addition of DMF. The nature of splaying upon DMF addition is shown in Fig. 72. The observations from these sequential images are listed below:

1. Dripping.



(a)

(b)



(c)

Fig. 71 Photographs showing fiber morphology for various chloroform/DMF ratios (v/v) (a) Pure chloroform (b) 12:1 (c) 9:1

2. Cone-jet forms and primary splaying (major jet) occurs at the end of the jet.
3. Cone-jet splits into two jets at the end of the needle.
4. Cone-jet splits into 6 jets (primary splaying—major jet) and spinning jet occurs.
5. Six spinning jets are generated at the end of the needle and continuous movements of the jets can be observed in different frames.
6. *Each spinning jet splits into thousands of mini-jets almost immediately below the needle, with each mini-jet gradually solidifying after solvent evaporation.*

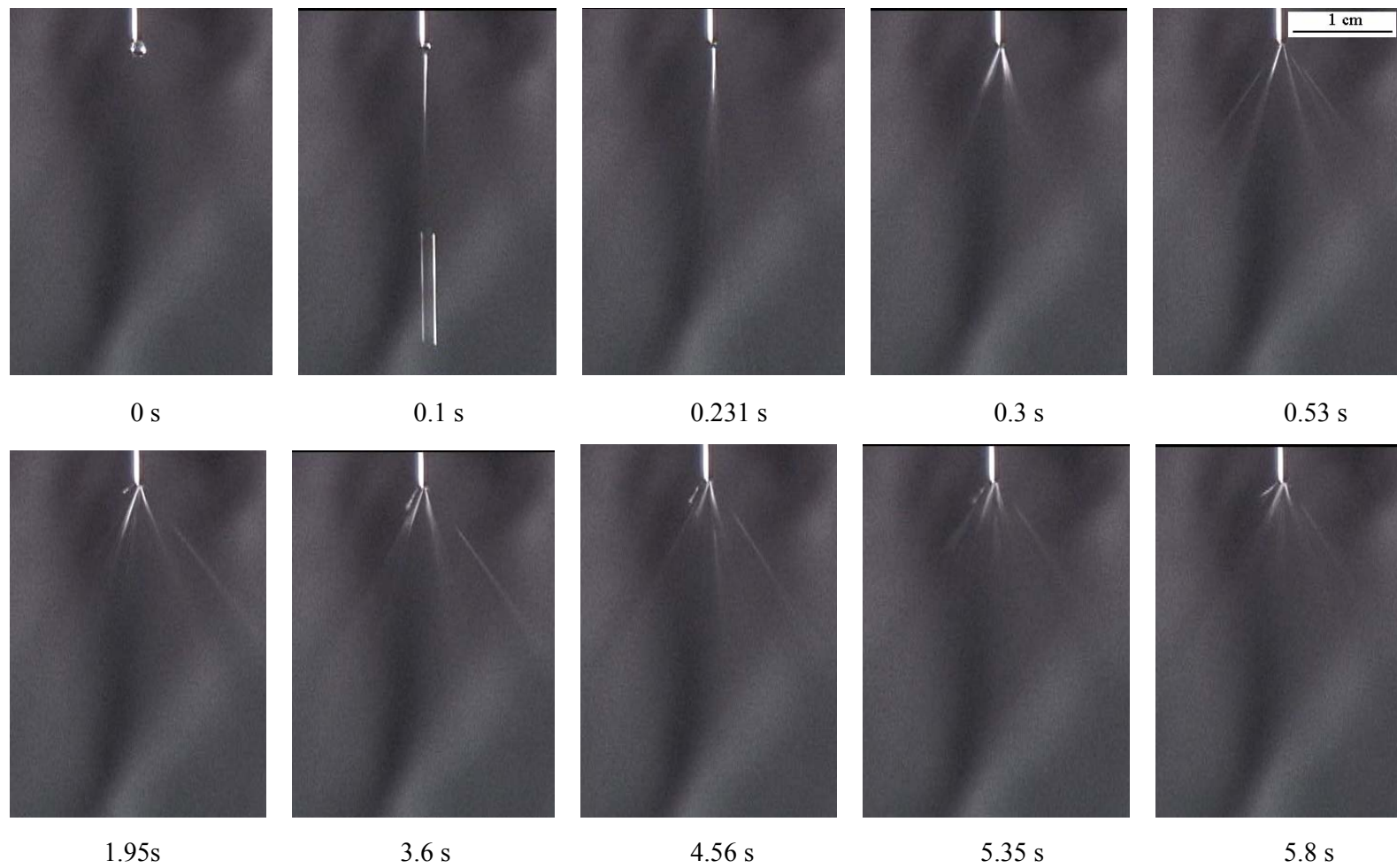


Fig. 72 Sequential images showing the breakdown and splaying of the jet with DMF (5wt% PCL, 40 kV, Chloroform/DMF ratio = 12:1 v/v).

The effects of DMF on the breakdown and splaying of the jet is summarized in Fig. 73. The repeated splaying in the presence of DMF is clearly shown. The amount of DMF added to chloroform can be controlled to produce a variety of structures. Similar results have been obtained with other solvents too. For example, Lee *et al* [40] have shown that DMF is effective with toluene and methylene chloride as the base solvent. DMF is thus able to act as a potential polyelectrolyte in a host of solvents. The addition of DMF at low solution concentrations (< 3 wt%) may also reduce the size of the diameter of the beads produced under these conditions.

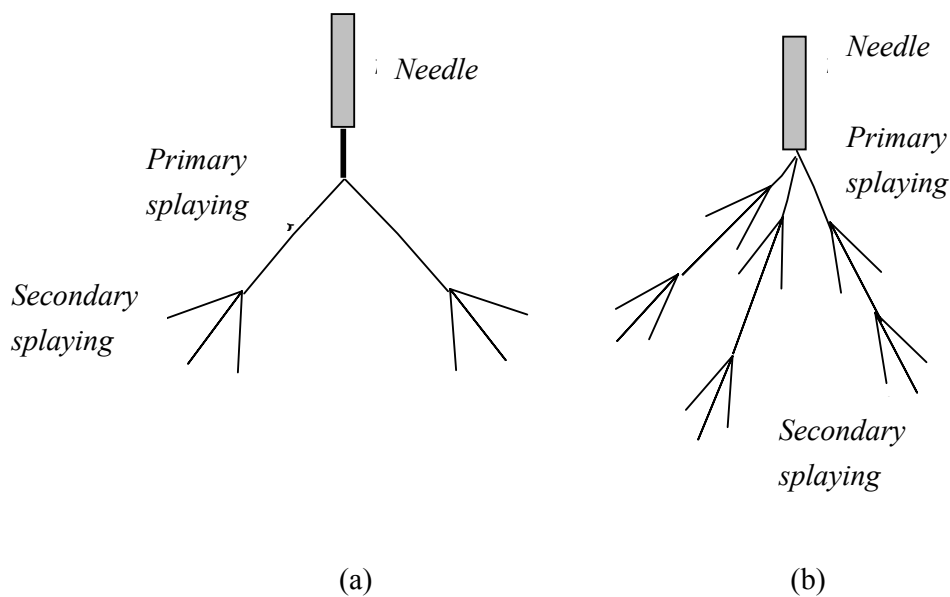


Fig. 73 Schematic illustration of the differences between the breakdown and splaying of the jet without (a) and with DMF (b).

5.8 Effects of Electrospinning on Microstructure of PCL

The microstructure of the electrospun polymer is controlled by the rapid phase separation induced by solvent evaporation. Subsequently, crystallites may form in a

crystalline polymer by nucleation and growth. The extent of crystallite formation depends on several factors including solvent vaporization rate, deposition rate and polymer molecular characteristics. Nucleation and growth of crystallites may be enhanced by slower deposition rates. In amorphous polymers, oriented structures may be produced in the fibers. The degree of orientation depends on the extent of elongational flow.

The degree of crystallinity in the polymer was examined by DSC. A typical DSC curve in the base polymer is shown in Fig. 74. An endothermic peak corresponding to the melting of the PCL is observed at about 60°C. The area under the endothermic peak corresponds to a heat of fusion of about 80 J/g. The heat of fusion for a completely crystalline PCL has been reported to be about 135 J/g [42]. Hence, the degree of crystallinity in the base polymer before electrospinning is about 60%. DSC curves for various voltages and solution concentrations are shown in Figs. 75 and 76 respectively. Electrospinning the polymer reduces the degree of crystallinity as shown in Table IX. Similar results have been reported previously for other polymers [9]. The rapid solidification of highly stretched chains under high elongational strain rates may hinder crystallinity. Solution concentration or the voltage did not have a significant effect on the degree of crystallinity in the electrospun polymer (Table IX).

The results presented here indicate that porous PCL structures can be produced by electrospinning. A range of morphologies can be produced by controlling the operating parameters such as voltage solution concentration and deposition distance. Additives such as DMF can be used to further refine the structure. The structures

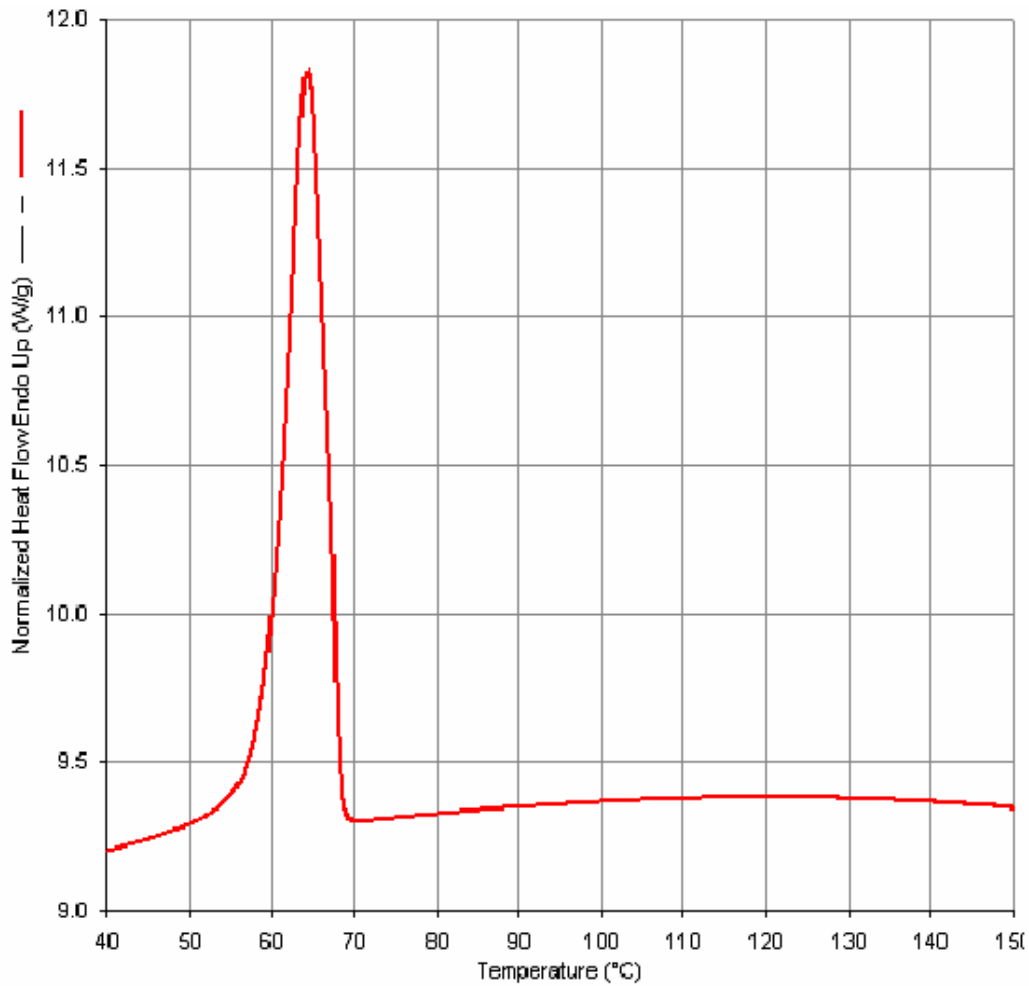


Fig. 74 Typical DSC curve for as received PCL (heating rate = 10 °C/min).

produced may contain beads, fibers or a combination of the two (the typical bead-on-string morphology). The fibrous structure contains interconnected pores and because of the sub-micron size of the fiber may have a large surface area. Such microporous, non-woven structures may be very useful in tissue engineering and drug delivery. A recent investigation has shown that electrospun PCL scaffolds can be served as good candidate materials for bone tissue engineering [43]. The wide of range of structural characteristics that may be obtained in the electrospun polymer make it suitable for many other biomedical applications including medical textiles,

drug delivery, membrane separation and organ regeneration. In addition,

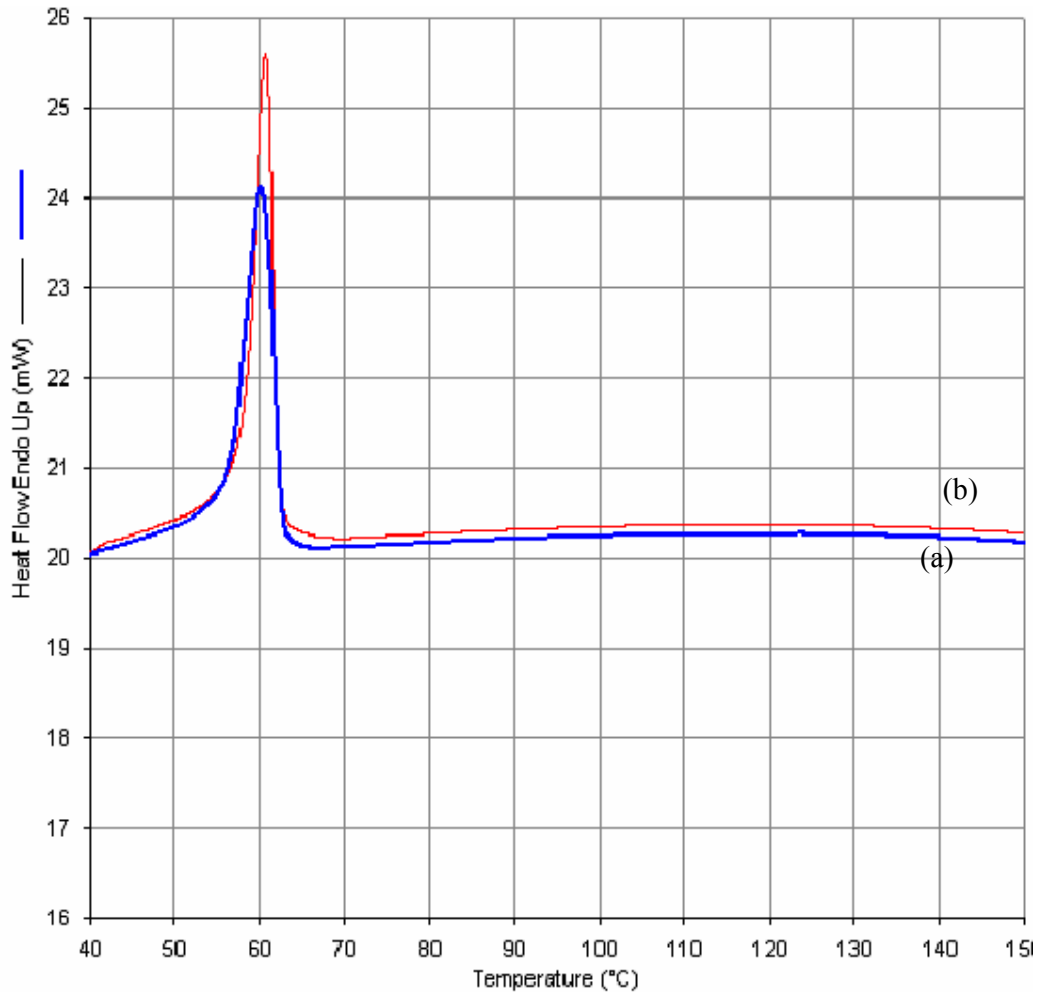


Fig. 75 DSC curves for electrospun PCL produced at (a) 20kV (b) 40kV (Solution concentration = 5 wt% PCL, deposition distance = 7.5 cm).

nanocomposites and layered structures can be produced by suitable additions to the solution. Shao et al [36] have recently used electrospinning to produce fiber mats of organic–inorganic hybrids, using silica nanofibers in a polymer matrix. Electrospinning can, therefore, be used to produce novel material structures with dramatic improvement in properties.

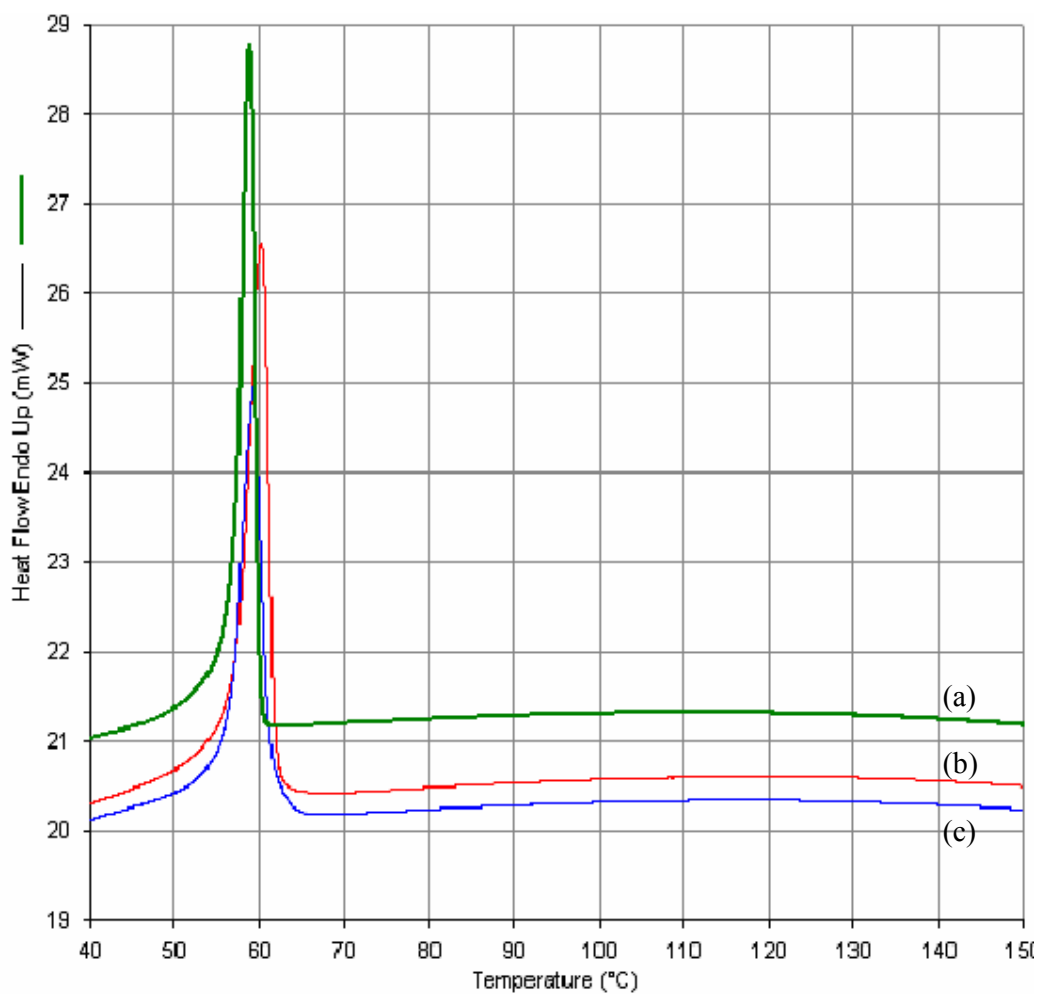


Fig. 76 DSC curves for electrospun PCL produced at (a) 3 wt% (b) 5 wt% (c) 9 wt% (30 kV, deposition distance = 7.5 cm).

Table IX Heats of fusion obtained from the measured peaks in the DSC curves for various conditions. The %crystallinity calculated from the heats of fusion is also shown.

Condition	ΔH (J/g)	% crystallinity
as- received	80	60%
electrospun, 3%-30kV	45	33%
electrospun, 9%-30kV	41	30%
electrospun, 5%- 20kV	42	31%
electrospun, 5%- 40kV	40	30%
electrospun, 9%- 40kV	47	35%

6. CONCLUSIONS

Electrospinning can be used to produce a wide range structures with Poly(ϵ -Caprolactone), PCL. The structure in the electrospun polymer may consist of beads, fibers or a combination of beads and fibers. The beads may be spherical or elongated (spindle-like) while the fibers may be round or flat. The combination of elongated beads and fibers, known as the bead-on-string morphology was observed under many conditions. The fibers may exhibit a variety of coils, loops and bends resulting primarily from the bending instability. The beads may form when the jet at the end of the Taylor's cone splits into many minijets and each minijet disintegrates into small droplets. The fibers are formed when the jet at the end of the Taylor's cone undergoes elongational flow and then breaks up into several stable minijets that accelerate toward the collector. During its transit to the collector, each minijet can further split into smaller jets with almost equal diameter. This process known as splaying determines the size of the final fiber obtained on the collector. Electrospinning may lower the degree of crystallinity in the polymer.

The solution concentration has a significant effect on the morphology of the electrospun polymer. At solution concentrations between 1 and 4 wt% PCL, the jet breaks down into droplets. In this concentration range, the average diameter of the bead increases with concentration. Average particle diameters were measured to be on the order of 900 nm and 5 μm at solution concentrations of 1 wt% and 3 wt% PCL respectively. Both solid and hollow beads can be produced by controlling the experimental conditions. The transformation from beads to interconnected fibers begins at about 4 wt% PCL in the solution. The average fiber diameter increases

with solution concentration from about 510 nm at 5 wt% PCL to 850 nm at 9 wt% PCL. The fiber diameters typically exhibit a bimodal distribution. At solution concentrations greater than 9 wt% PCL, electrospinning becomes difficult. The data indicate that the breakdown of the jet is determined primarily by varicose instability at low concentrations, while at high solution concentration bending instability has a major role in splitting and splaying of the jet.

The critical voltage for the ejection of the jet from the Taylor's cone is measured to be between 5 to 7 kV. The deposition rate of the polymer increases with the applied voltage. At low voltages (10 to 20 kV), the structure consists predominantly of beads with some filaments between the beads. As the voltage is increased beyond 25 kV, a fibrous structure is stabilized. The extent of splaying in the jet increases with the electrical field strength and hence the average diameter of the fiber decreases with increasing voltage.

Electrospinning at short deposition distances yields coalesced beads of irregular geometry or flat fibers. By contrast, spherical beads or round fibers are produced at large deposition distances. If the deposition distance becomes too large, the electrical field strength per unit length decreases and hence the jet may break down primarily into relatively large beads.

The addition of DMF to the solution has a significant effect on the electrospinning process. The deposition rate and the extent of splaying increase dramatically leading to the production of ultrathin nanofibers. The lowest average fiber diameter with and without DMF in the solution have been measured to be on the order of 150 and 450 nm respectively. A chloroform to DMF ratio of 9:1 (v/v) yielded the best results.

Hence, a range of morphologies can be produced in the electrospun polymer by controlling the operating parameters such as voltage, solution concentration and deposition distance. Additives such as DMF or other polyelectrolytes can be used to further refine the structure. Such microporous, non-woven structures may be very useful in numerous applications including tissue engineering, drug delivery, medical textiles, and membrane separation. Electrospinning can, therefore, be used to produce novel material structures with dramatic improvement in properties.

7. REFERENCES

1. A.S. Hoffman, *Advanced Drug. Delivery Reviews* **54** (1) (2002) 3-12.
2. K. F. Leong, C. M. Cheah and C. K. Chua, *Biomaterials* **24** (2003) 2368-2378.
3. O. Pillai and R. Panchagnula, *Current Opinion in Chemical Biology* **5**, Issue 4, 1 August 2001, 447-451.
4. C.J. Liao, C.F. Chen, J.H. Chen, S.F. Chiang, Y.J. Lin, K.Y. Chang, *J Biomed Mater Res* **59** (2002) 676-681.
5. Robert P. Lanza, Robert Langer, Joseph Vacanti. *Principles of Tissue Engineering* 2nd edition, Academic Press, San Diego, 2000.
6. W.J. Lin, D.R. Flanagan, R.J. Linhardt, *Polymer* **40** (1999) 1731-1735.
7. H.L. Khor, K.W. Ng, J.T. Schantz, T.T. Phan, T.C. Lim, S.H. Teoh, D.W. Hutmacher, *Materials Science and Engineering C20* (2002) 71-75.
8. J.C. Middleton and A.J. Tipton, *Biomaterials* **21** (2000) 2335-2346.
9. J. M. Deitzel, J. Kleinmeyer, D. Harris and N. C. Beck Tan, *Polymer* **42** (2001) 261-272.
10. E. Kenawy, J. M. Layman, J. R. Watkins, G.L. Bowlin, J. A. Matthews, D. G. Simpson and G.E. Wnek, *Biomaterials* **24** (2003) 907-913.
11. P. Gibson, H. Schreuder-Gibson and D. Rivin, *Colloids and Surfaces A: Physicochemical and Engineering Aspects* **187-188** , 31 August 2001, 469-481.
12. W.J. Li, C.T. Laurencin, E.J. Caterson, R.S. Tuan, F.K. Ko, *J Biomed Mater Res* **60** (2002) 613-621.
13. Christopher J. Buchko, Loui C. Chen, Yu Shen and David C. Martin, *Polymer* **40** (1999) 7397-7407.
14. X. Zong, K. Kim, D. Fong, S. Ran, D. Hsiao and B. Chu, *Polymer* **43** (2002) 4403-4412.
15. K. Ohgo, C. Zhao, M. Kobayashi, T. Asakura, *Polymer* **44** (2003) 841-846.
16. C.J. Buchko, K.M. Kozloff, D.C. Martin, *Biomaterials* **22** (2001) 1289-1300.
17. H.J. Jin, S.V. Fridrikh, G.C. Rutledge, D. L. Kaplan, *Biomacromolecules* **3** (2002) 1233-1239.
18. J.A. Matthews, G.E. Wnek, D. V. Simpson, G. L. Bowlin, *Biomacromolecules* **3** (2002) 232-238.
19. D.H. Reneker, I. Chun, *Nanotechnology* **7** (1996) 216-223.
20. H. Fong, I. Chun, D.H. Reneker. *Polymer* **43** (1999) 4585-4592.
21. D.H. Reneker, H. Fong, S. Koombhongse, *J of Applied Physics* **87**(9) (2000) 4531-4547.

22. S. Koombhongse, W. Lin, D.H. Reneker. *J Polym Sci Part B: Polym Phys* **39**: (2001) 2598-2606.
23. D.H. Reneker, W. Kataphinan, A. Theron, E. Zussman, A.L. Yarin, *Polymer* **43** (2002) 6785-6794.
24. A.F. Spivak, Y.A. Dzenis, D.H. Reneker, *Mechanics Research Communications* **27**(1) (2000) 37-42.
25. A. L. Yarin, S. Koombhongse, D.H. Reneker, *J of Applied Physics* **90**(9) (2001) 4836-4846.
26. H. Fong, D.H. Reneker, *J of Polymer Science: Part B: Polymer Physics* **37** (1999) 3488-3493.
27. J. Doshi, D.H. Reneker, *J of Electrostatics* **35** (1995) 151-160.
28. G. Taylor. *Proc Roy Soc London A* **313** (1969) 453-475.
29. C.D. Hendricks, R.S. Carson, J.J. Hogan and J.M. Schneider. *AIAA J* **2** (1964) 733-737.
30. M.M. Hohman, Y.M. Shin, G.C. Rutledge, M.P. Brenner, *Physics of Fluids* **13**(8) (2001) 2201-2220.
31. M.M. Hohman, M. Shin, G. Rutledge. M. P. Brenner, *Physics of Fluids* **13**(8) (2001) 2221-2236.
32. Y.M. Shin, M.M. Hohman, M.P. Brenner, G.C. Rutledge. *Polymer* **42** (2001) 9955-9967.
33. A. Jaworek, A. Krupa. *J Aerosol Sci* **30**(7) (1999) 873-893.
34. L. Larrondo and R. Manley, St John. *J Poly Sci, Poly Phys Ed* **19** (1981) 909-940.
35. J.M. Deitzel, J.D. Kleinmeyer, J.K. Hirvonen, N.C. Beck Tan, *Polymer* **42** (2001) 8163-8170.
36. C. Shao, H.Y. Kim, J. Gong, B. Ding, D.R. Lee, S.J. Dark, *Materials Letters* **57** (2003) 1579-1584.
37. Ferdinand Rodriguez, *Principles of Polymer System*, 3 rd edition, Hemisphere Publishing Corporation, New York, 1989.
38. C.G. Pitt, M.M. Gratzl, G.L. Kimmel, J. Surles, A. Schindler, *Biomaterials* **2** (1981) 215-220.
39. David R. Lide, *Handbook of Organic Solvents*, CRC Press, Florida, 1995.
40. K.H. Lee, H.Y. Kim, M.S. Khil, Y.M. Ra, D.R. Lee, *Polymer* **44** (2003) 1287-1294.
41. M.M. Demir, I. Yilgor, E. Yilgor, B. Erman, *Polymer* **43** (2002) 3303-3309.
42. G. Maglio, A. Migliozzi, R. Palumbo, *Polymer* **44** (2003) 369-375.
43. H. Yoshimoto, Y.M. Shin, H. Terai, J.P. Vacanti, *Biomaterials* **24** (2003) 2077-2082.

APPENDICES

Appendix A *Properties of Poly (ϵ -Caprolactone) used in this study*

Property	ASTM Test	TONE® Polymer	
		P-767	P-787
Melt Flow – 80°C, 44 psi, g/10 min.	D 1238-73	1.9	0.5
– 125°C, 44 psi, g/10 min.		7.0	1.0
– 190°C, 44 psi, g/10 min.		30	4.0
Density at 23°C (73°F), g/cc		1.145	1.145
Melting Temperature, °F (°C)		140 (60)	140 (60)
Tensile Strength, psi (MPa)	D 412-68		
2 in/min		3600 (26.0)	6000 (41.4)
20 in/min		3100 (21.3)	5800 (39.7)
Tensile Modulus psi (MPa)		63,000 (435)	56,000 (386)
Ultimate Elongation, %			
2 in/min		600-1000	800-1000
20 in/min		600-800	750-900
Flexural Modulus, psi (MPa)		83,300 (575)	74,400 (514)
Flexural Stress at 5% strain, psi (MPa)		3400 (23.4)	3000 (21.0)
Izod Impact, ft-lb/in (J/m)			
Notched	D 256-73A	1.5-3.0 (82)	6-8 (350)
Unnotched		No Break	No Break
Tensile Impact Strength ft-lb/in ² (kJ/m ²)	D 1822	28 (58)	185 (386)
Coefficient of Linear Thermal Expansion in/Difference/°C		1.55 x 10 ⁻⁴	1.663 x 10 ⁻⁴
Water Absorption, %		0.3508	0.3295
Shore Hardness	D 2240-75	55D	55D

Appendices B to E contain additional photographs of electrospun PCL produced under various conditions. These appendices are presented on the enclosed CD.